Martin Faccinelli

Spatially resolved measurements of charge carrier properties in proton doped silicon

For obtaining the academic degree
Master of Science

Master Programme of
Advanced Materials Science

Graz University of Technology

Supervisor:
Univ.-Prof. Ph.D Peter Hadley
Institute of Solid State Physics

Graz, February 2013

Abstract

The demands on semiconductor devices increase each year. Both, the reliability and the efficiency of these devices has to be improved constantly. To guarantee the constant improvement of semiconductor devices, new manufacturing processes as well as new analysis methods have to be developed.

This thesis focuses on one such process, called proton doping. Using proton doping, defects are generated in silicon in a controlled way. During an annealing step these defects form defect complexes which can act as electron donors and hence can change the charge carrier concentration in a device. The change of the resistivity and the minority carrier diffusion length in proton doped, Czochralsky grown silicon, caused by the formation of such donor complexes, was measured space-resolved, using Spreading Resistance Profiling (SRP) and Electron Beam Induced Current analysis (EBIC). A method has been developed to measure the resistivity and the doping type of a semiconductor sample in a scanning electron microscope (SEM). While a four-point-method yielded the resistivity, an EBIC-measurement at a Schottky junction was used to determine the doping type. In addition, the formation of the so called "super junction", which is the blocking state of a CoolMOS$^{\mathrm{TM}}$-device was visualized using EBIC.

Kurzfassung

Die Anforderungen an Halbleiterbauelementen steigen täglich. Neben der Funktionssicherheit muss vor allem auch das Leistungsvermögen solcher Bauteile ständig verbessert werden. Um die ständige Verbesserung von Halbleiterbauteilen zu gewährleisten, müssen regelmäßig sowohl neue Herstellungsverfahren als auch neue Analysenverfahren entwickelt werden.

Diese Arbeit befasst sich mit einem dieser Verfahren, der Dotierung mittels Protonen. Durch Protonendotieren werden gezielt Defekte in Silizium erzeugt, welche sich durch Tempern zu Defektkomplexen verbinden. Einige dieser Defektkomplexe fungieren als Elektronendonatoren und können somit die Ladungsträgerkonzentration im Bauteil ändern. Die, durch die Bildung solcher Defektkomplexe verursachte Änderung des spezifischen Widerstands und der Diffusionslänge der Minoritätsladungsträger in protonendotiertem, Czochralsky gezogenem Silizium wurde mittels Spreading Resitance Profiling (SRP) und Electron Beam Induced Current (EBIC) ortsaufgelöst bestimmt. Es wurde eine Methode entwickelt, mit der in einem Rasterelektronenmikroskop (REM) sowohl der Dotiertyp, mittels EBIC-Messung an einem Schottky-Übergang, als auch der spezifische Widerstand einer Probe, mittels Vier-Punkt-Messung, bestimmt werden kann. Des Weiteren wurde die Bildung der sogenannten „Super-Junction", dem Sperrzustand eines CoolMOS$^{\text{TM}}$-Bauelements mittel EBIC sichtbar gemacht.

Statutory Declaration

I declare that I have authored this thesis independently, that I have not used other than the declared sources / resources, and that I have explicitly marked all material which has been quoted either literally or by content from the used sources.

26 February, 2013
Date

Signature

Acknowledgement

Contents

6 Annealing Series of Proton Doped Samples   **53**

7 Formation of the Super Junction in a CoolMOS$^{\text{TM}}$ Device   **75**

8 Discussion of the Measurements   **81**

9 Conclusions   **87**

10 References   **89**

11 List of Figures   **93**

12 List of Tables   **96**

13 Appendix   **97**

1 Abbreviations and Variables

Table 1.1: Abbreviations

AC	Alternating Current
AD converter	Analogue-Digital converter
AES	Auger Electron Spectroscopy
AFM	Atomic Force Microscopy
CoolMOS	Super Junction Metal Oxide Semiconductor Field Effect Transistor
Cz-Si	Silicon wafer produced using the Czochalski method
EBIC	Electron Beam Induced Current
EDX	Energy Dispersive X-ray Analysis
EPR	Electron Paramagnetic Resonance
DLTS	Deep Level Transient Spectroscopy
FIB	Focused Ion Beam
FZ-Si	Silicon wafer produced using the float-zone method
IR	Infra-Red
IV	Current-voltage characteristic
LabVIEW	Laboratory Virtual Instrumentation Engineering Workbench
MOSFET	Metal Oxide Semiconductor Field Effect Transistor
PEN	Control Sample for measuring the penetration of the probes in SRP
QTA	Control Sample for measuring the reproducibility of the electrical contact of the probes in SRP
RF	Radio Frequency
SCM	Scanning Capacitance Microscopy
SEM	Scanning Electron Microscope
SRP	Spreading Resistance Profiling
SSRM	Scanning Spreading Resistance Microscopy
ToF-SIMS	Time of Flight-Secondary Ion Mass Spectroscopy

Table 1.2: Variables

Variable	Significance	Unit
a	Radius of a point contact	[m]
A, B, C, D	Electrical contacts in a Van der Pauw measurement	
a_1, a_2	Radii of the point contacts at the two contacts in an SRP measurement	[m]
α	Fitting parameter	
A_{ij}	Arrhenius pre factor for the reaction of P_i and P_j to C_{ij}	
B_m	Magnetic field induction	[T]
C	Capacitance	[F]
c_1, c_2	Integration constants	
c_e, p	charge carrier concentration	$\frac{1}{\text{cm}^3}$
C_{ij}	Defect complex built up from precursors P_i and P_j	
d	Distance between the two point contacts in an SRP measurement	[m]
D	Diffusion coefficient	$\left[\frac{\text{m}^2}{\text{s}}\right]$
d_A	Distance between the centres of two p-columns in a CoolMOS$^{\text{TM}}$ device along direction A	[m]
d_B	Distance between the centres of two p-columns in a CoolMOS$^{\text{TM}}$ device along direction B	[m]
D_e	Diffusion coefficient of electrons	$\left[\frac{\text{m}^2}{\text{s}}\right]$
D_i	Diffusion coefficient of P_i according to Fick's second law	$\left[\frac{\text{m}^2}{\text{s}}\right]$
D_p	Diffusion coefficient of holes	$\left[\frac{\text{m}^2}{\text{s}}\right]$
ϵ_s	Dielectric constant of a semiconductor sample in an SCM measurement	$\frac{\text{F}}{\text{m}}$
E	Electric field	$\left[\frac{\text{V}}{\text{m}}\right]$
E_0	Electron beam energy	[keV]
Ea_{ij}	Activation energy for the reaction of P_i and P_j to C_{ij}	[J]
E_c	Conduction band energy	[J]
E_F	Fermi energy	[J]
E_i	Intrinsic energy (mid band gap energy)	[J]
E_v	Valence band energy	[J]
G	Generation term (number of charge carriers generated by the incident electron beam)	
$G_0\delta$	Generation term approximated as a delta function	
I	Current	[A]
I_{12}	Current between tip 1 and 2 in a four point resistivity measurement	[A]

Variable	Significance	Unit
I_{DD}	Drift/Diffusion current	[A]
I_{EBIC}	Measured electron beam induced current	[A]
I_{offset}	Offset current in an EBIC measurement	[A]
J	Current density	$[\frac{\text{A}}{\text{m}^2}]$
J_e	Current density due to drift and diffusion of electrons	$[\frac{\text{A}}{\text{m}^2}]$
J_p	Current density due to drift and diffusion of holes	$[\frac{\text{A}}{\text{m}^2}]$
k	Constant	[A]
k_B	Boltzmann constant ($1.381 \cdot 10^{-23}$)	$[\frac{\text{J}}{\text{K}}]$
k_{ij}	Reaction constant for the reaction of P_i and P_j to C_{ij}	$[\frac{\text{m}^3}{\text{s}}]$
l	Mean free path of electrons	[m]
L	Distance between the two contacts in a Haynes Shockley experiment	[m]
L_D	Minority carrier diffusion length	[m]
$\mu, v, teta$	Oblate spheroidal coordinates	
μ_e	Mobility of electrons	$[\frac{\text{m}^2}{\text{Vs}}]$
μ_H	Hall mobility	$[\frac{\text{m}^2}{\text{Vs}}]$
μ_p	Mobility of holes	$[\frac{\text{m}^2}{\text{Vs}}]$
n	Number of charge carriers	
n_0	Number of charge carriers at thermal equilibrium	
N_A	Number of acceptors	
N_D	Number of donors	
n_e	Number of electrons	
n_p	Number of protons	
P_i, P_j	Defect precursors	
q	Elementary charge ($1.602 \cdot 10^{-19}$)	[C]
ρ	Resistivity	[Ωcm]
ρ_1, ρ_1	Resistivity of the materials 1 and 2	[Ωcm]
ρ_m	Mass density	$[\frac{\text{g}}{\text{cm}^3}]$
r	Distance between the point of charge carrier generation and the pn-junction	[m]
R	Resistance	Ω
$\vec{r_1}, \vec{r_2}, \vec{r_3}, \vec{r_4}$	Positions of the tips in a four point resistivity measurement	
$\vec{r_1}', \vec{r_2}'$	Positions of the imaginary contacts in a four point resistivity measurement	
Rec	Recombination term	
R_G	Electron Range	[µm]

Variable	Significance	Unit
R_{SRP}	Spreading resistance	Ω
s	Distance to the z-axis in oblate spheroidal coordinates	[m]
$\mathrm{S}_1, \mathrm{S}_2$	Raw wafer samples	
s_{mn}	Distance between tip m and tip n in a four point resistivity measurement	[m]
T	Temperature	[K]
τ	Minority carrier lifetime	[s]
τ_{sur}	Minority carrier lifetime depending on surface recombination only	[s]
τ_{vol}	Minority carrier lifetime depending on bulk recombination only	[s]
t	Time	[s]
Δt	Time between the introduction and the measurement of charge carriers in a Haynes Shockley experiment	
t_s	Thickness of the sample in a Van der Pauw measurement	[m]
V	Voltage	[V]
V_{34}	Potential difference between the measuring tips 3 and 4 in a four point resistivity measurement	[V]
V_{bi}	Built in potential across a *pn-* or a Schottky junction	[V]
v_s	Surface recombination velocity	$\left[\frac{\mathrm{m}}{\mathrm{s}}\right]$
X	Depth of the interaction volume of the electron beam with a sample	[µm]
$x,\ y,\ z$	Cartesian coordinates	[m]
Y	Lateral extension of the interaction volume of the electron beam with a sample	[µm]
Z	Atomic number	
Φ	Electrostatic potential	[V]

2 Introduction

Due to the automation of both, products and fabrication processes in all branches of industry, the demand on semiconductor devices has increased rapidly over the last decades. As every technology has to work faster and the reliability has to be increased all the time, also the properties of these devices have to be improved constantly. On the same time the size of semiconductor devices has to be scaled down as electrical devices grow smaller and smaller. To fulfil these demands there is a constant need for new technologies and new fabrication processes in semiconductor industry. These new processes include methods which yield very thin layers and a very homogeneous carrier concentration.

This thesis focuses on a technique called proton implantation. In this method a proton beam is scanned over a silicon sample introducing both, radiation damage, hence vacancies and interstitials, and protons. In an annealing step after the implantation these vacancies form defect complexes in combination with impurities like oxygen or carbon. Some of these complexes can act as electron donors and hence influence the effective carrier concentration. Even though this method is already applied in industrial processes, it is not yet been completely revealed which defect complexes are present and what their microscopic structure looks like.

A lot of analytical methods have been applied to investigate those defect complexes including Infra-red (IR) Spectroscopy, Spreading Resistance Profiling (SRP), and Deep Level Transient Spectroscopy (DLTS). However, since the number and the composition of the different defect complexes is strongly dependent on the quality of the substrate material and on the implantation conditions such as the implantation energy and the implantation dose, it is almost impossible to compare the results the different studies.

This thesis focuses on Electron Beam Induced Current (EBIC) methods which are applied in a Scanning Electron Microscope (SEM). In this method an electron beam is scanned over a sample and induces locally electrons and holes. If this carrier generation is close to a built in electric field, such as a pn-junction or at a Schottky contact, due to charge carrier separation a current is induced and can be measured. The signal can include information about the doping type and the minority carrier diffusion length. The method was used to investigate a proton doped silicon sample which has been annealed at different temperatures. The results of these measurements have been compared to SRP-measurements and the formation and the disappearance of different thermal donors could be observed.

Additionally some EBIC methods have been applied on ready produced devices to visualize certain specialities. Using EBIC, the p-doped columns in the n-doped matrix in a CoolMOS$^{\mathrm{TM}}$-device could be illustrated as well as the formation of the super junction.

3 Background

Most samples investigated in this thesis where doped with very low doping concentration. In this case, the defects that are introduced during the production can be responsible for the electrical properties that the final circuits exhibit. This section gives a general overview of the production steps of a semiconductor device with a special focus on the implantation of protons into silicon.

3.1 Development of a Silicon Semiconductor Device

The development and realization of a silicon semiconductor device is an elaborate process and contains of many hundred process steps. Starting with the production of the silicon substrate, called wafer, a few process steps leading to an applicable device are described.

3.1.1 Single Crystal Wafer Production

The starting substrate for the production of a silicon device is an ultra clean single-crystalline raw silicon wafer. A wafer is a disk shaped, about 1 mm thick, single-crystalline piece of silicon. The way the wafer is produced can already affect the finished device regarding (unwanted) defect concentrations.

Czochralsky Process

In the Czochalsky process, a single crystalline silicon ingot is produced from a seed crystal in a silica crucible. In the crucible the seed crystal is in contact with a pure silicon melt. While rotating the seed crystal as well as the crucible, the crystal is pulled upwards while growing layer by layer. The process is capable of producing ingots with diameters of more than 300 mm and several meters in length. A big drawback of the method is the introduction of (relatively) high concentrations of defects, as the silicon melt is in contact with the crucible. Both, the oxygen-, as well as the carbon concentration are in the range of $10^{17}\,\mathrm{cm}^{-3}$. For many applications Cz-Si is used as a substrate for epitaxially grown wafers.

Float Zone Method

The float zone method uses a pure polycrystalline ingot which is remelted into a single crystalline ingot using vertical zone melting. In the beginning of the process, a seed crystal is brought into contact with the ingot. At this contact, the zone melting starts, as the heat source (usually RF-coils) is moved along the ingot. As the process doesn't need a crucible, the quality of the single crystal regarding contaminations is low. The carbon concentration is below $10^{15}\,\mathrm{cm}^{-3}$ and the oxygen concentration is smaller than $10^{16}\,\mathrm{cm}^{-3}$. The disadvantage of this method is the limitation in the ingot diameter. Due to the surface tension during the remelting process, only ingots with at most 150 mm in diameter can be produced.

Wafer Completion

The adjustment of the doping level takes place during the Czochralskiy single crystal production by adding the dopant directly to the crystal melt. However dopants are removed during zone refining, so FZ-Si is doped using neutron transmutation doping. In this technique, the silicon ingots are bombarded with neutrons. Silicon appears as the isotopes ^{28}Si, ^{29}Si and ^{30}Si in an abundance of 92.23 %, 4.67 % and 3.1 %. The neutrons only affect ^{30}Si and transmute it in the reactions

$$^{30}\text{Si} + \text{n} -> ^{31}\text{Si} + \gamma$$

under the release of a γ-quantum and

$$^{31}\text{Si} -> ^{31}\text{P} + \beta$$
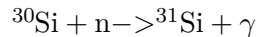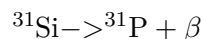
under the release of an electron (β-quantum) to ^{31}P. The half life of this decay is 2,63 h. The process of neutron transmutation doping takes several weeks but the doping distribution that is received is very homogeneous.
After the adjustment of the doping level, the ingots are cut into wafers which are then lapped and etched to receive a clean surface.

3.1.2 Wafer Processing

This section gives a short overview on some steps in the production of a silicon device. A more detailed description of these processes can be found in [1].

Layer Formation

Semiconductor devices usually consist of more than just the substrate. To fabricate additional layers, that differ in doping type or doping concentration, and depending on the size and the shape of the layers or regions one wants to create, different methods are used. Depending on the device that is fabricated and on the material quality needed, regarding especially oxygen and carbon contamination, either a raw wafer substrate is used and additional layers are introduced into this substrate, or the whole device is grown on a carrier wafer which is removed in the end.

The growth of a device is made by epitaxially depositing silicon from gaseous precursors on a carrier wafer. There are different silicon precursors that can be used for this. Either the reaction of silicon tetrachloride $SiCl_4$ or trichlorosilane $SiHCl_3$ with hydrogen to silicon and hydrochloride:

$$SiCl_4 + 2\,H_2 \longrightarrow Si + 4\,HCl$$

$$SiHCl_3 + H_2 \longrightarrow Si + 3\,HCl$$
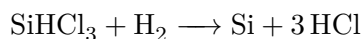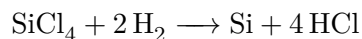
or the degradation of dichlorosilane SiH_2Cl_2 or silane SiH_4:

$$SiH_2Cl_2 \longrightarrow Si + 2\,HCl$$

$$SiH_4 \longrightarrow Si + 2\,H_2$$
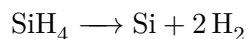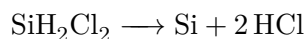
is used. Each reaction is performed at more than $1000\,°C$ in H_2 atmosphere. The doping type and doping concentration are controlled by adding e.g. PH_3 (phosphine) for n-doping or B_2H_6 (diborane) for p-doping to this atmosphere. The great benefit of epitaxial growth is its high purity but as the method is expensive, other procedures might be favoured.

One way to produce differently doped regions in a silicon raw wafer is the diffusion of dopant atoms into silicon. Two different shapes of the doping profile can be obtained. A profile of the form of the error function is generated by e.g. diffusion of atoms from the gas phase into the silicon. A Gaussian profile is obtained after an annealing procedure, when the dopant atoms have already been introduced in a precedent step (e.g. in a first diffusion step or via proton implantation).

For the production of doped layers close to the surface ion implantation is used. In this method the dopant atoms are ionised and accelerated in an electric field. The ion beam, which has a diameter of up to several mm is then scanned over the wafer. Due to scattering at the lattice atoms and deceleration in the electron shells of the lattice atoms, the implanted ions get stuck in a certain depth. The implantation depth is controlled by the acceleration energy of the implanted ions and the doping concentration is regulated by the implantation dose. As ion implantation causes radiation damage the implanted sample has to be annealed in a subsequent step. This annealing step also moves the dopant atoms to interstitial lattice sites which makes them electrically active. The emerging doping profile has the shape of a Gaussian.

Oxide layers, such as the gate oxide in a MOSFET are made by dry oxidation of a surface using molecular oxygen:

$$Si + O_2 \longrightarrow SiO_2$$
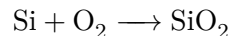
As the growth rate of the oxide is very small, only thin oxide layers are produced this way. Some process steps, like the formation of passivation layers need thicker oxide layers which are produced by wet oxidation at $1120\,°C$:

$$Si + 2\,H_2O \longrightarrow SiO_2 + 2\,H_2$$
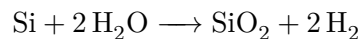
SiO_2 layers are also used as masking layers in diffusion processes, as the diffusion of boron and phosphorus is far smaller in silicon dioxide than in pure silicon.

Introduction of Recombination Centres

An important influence of the properties of a semiconductor device is the charge carrier lifetime. This lifetime can be regulated by the introduction of recombination centres.

Commonly used is the method of inserting gold or platinum into silicon by diffusion. Gold offers an acceptor state at $0.54\,eV$ below the conduction band and a donor state at $0.35\,eV$ above the valence band in the band gap of silicon. Hence it can act as act as both, recombination and generation centre. The disadvantage of the use of gold and platinum is the bad repeatability of the diffusion process leading to a higher dispersion of the semiconductor properties. Hence, especially for high power diodes, recombination centres are created by radiation. For a homogeneous profile of recombination centres, the devices are irradiated with electrons. If localized profiles are desired, proton - or helium irradiation is used. Here the implantation depth can be regulated by the acceleration energy. If a sample is irradiated with electrons,

protons or helium cores, silicon atoms get kicked out of the lattice leading to vacancies and interstitials. The radiation also interacts with defects such as carbon or oxygen, forming a variety of defects and defect complexes. Reference [2] gives an overview of some of the defect complexes induced by radiation. After the irradiation, in a subsequent step the sample has to be annealed. Depending on the annealing temperature and also the annealing time, different defect complexes are formed or removed.

3.1.3 Proton Implantation

The implantation of protons into silicon is a technique that can be used for different concerns in the production of a semiconductor device. Depending on the implantation conditions proton implantation can be used to increase the number of recombination centres [3], to generate donor-defects [4] or, at high implantation doses, even to cut a sample [5].

When silicon is implanted with protons at doses from $10^{13}\,\mathrm{H^+/cm^2}$ to $10^{15}\,\mathrm{H^+/cm^2}$ [6] hydrogen related complexes are formed leading to an increase of the donor concentration. Reference [7] gives a collection of references on what is already known about hydrogen related donor complexes. As some of these complexes form and disappear due to a certain thermal budged they are called thermal donors. The concentration of the different types of thermal donors is controlled in an annealing procedure subsequently to the proton implantation. Table 3.1 from [6] gives an overview of the temperature range where some thermal donors appear in Cz-grown silicon.

Table 3.1: Temperature ranges of hydrogen related thermal donors in Cz-Si.

Themal Donor	Temperature Range [°C]	Reference
TD1	350-500	[8]
TD2	300-500	[9]
TD3	300-500	[9]
TD4	300-500	[10]

In general the formation of such a complex C_{ij} can be formulated like a chemical reaction. Usually such reactions are complicated, as many reaction partners can be involved, but for simplification a second-order-reaction of two components or precursors P_i and P_j is assumed as

$$P_i + P_j \longrightarrow C_{ij}.$$
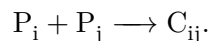
These precursors can be atoms, vacancies or even small complexes. The reaction rate can be formulated as

$$\frac{d[C_{ij}]}{dt} = k_{ij}[P_i][P_j], \tag{3.1}$$

where $[C_{ij}]$, $[P_i]$ and $[P_j]$ are the concentrations of the different reaction partners and k_{ij} is the reaction constant.

The reaction rate depends on the temperature as given by the Arrhenius equation

$$k_{ij} = A_{ij}e^{-(Ea_{ij}/k_BT)}, \tag{3.2}$$

where A_{ij} is a pre-factor and Ea_ij is the activation energy for the reaction of P_i and P_j to C_{ij} and k_B is the Boltzmann constant.

The concentrations of the precursors depend on diffusion as given by Fick's second law:

$$\frac{\delta[\mathrm{P}_i]}{\delta t} = D_i \frac{\delta^2[\mathrm{P}_i]}{\delta x^2},$$

(3.3)

where D_i is the diffusion coefficient.

The complexes formed can be donors, acceptors, or recombination centres. Either they change the concentration of one type of charge carrier, or they influence the charge carrier lifetime. If the number of donors N_D exceeds the number of acceptors N_A, the doping is n-type and if there are more acceptors than donors, the doping is p-type. If the reaction and diffusion constants would be known, the sample properties regarding charge carrier concentration, resistivity, or mobility could be simulated as a function of the annealing temperature. To get these constants, one would have to be able to measure the concentrations of the different precursors and defect complexes independently. Hence it is important to identify the structures of the different defect complexes and precursors to be able to develop techniques to measure their concentrations.

3.2 Basic Elements of Semiconductor Devices

The basic elements of all semiconductor devices are *pn-* and/or Schottky junctions. In this section these two components are described.

3.2.1 *pn*-Junction

Doping is the intentionally introduction of impurities into an intrinsic semiconductor to modulate its electrical properties. Generally it is differed between the introduction of electron acceptors (*p*-doping) and electron donors (*n*-doping). Acceptors lack one electron or more, compared to silicon. The absence of this electron is called a hole, which is a fictional, positively charged, charge carrier. Electron donors posses more electrons than silicon. Phosphorous, arsenic or antimony are typically used as donors in silicon, boron or aluminium act as acceptors. While the existence of holes shifts the Fermi energy closer to the valence band energy, donors form energy levels close to the conduction band and hence shift the Fermi energy closer to the conduction band energy. The majority charge carriers are holes in a *p*-doped and electrons in an *n*-doped semiconductor. Besides the majority carriers also minority carriers (electrons in *p*- and holes in *n*-doped semiconductor) are present, nevertheless, in a far smaller concentration than the majority carriers.

If a *p*-doped and an *n*-doped semiconductor are brought into contact, a *pn*-junction is formed. Due to the concentration gradients majority carriers diffuse over to the other side of this junction, leaving the charged donors and acceptors behind. As a consequence a charge gradient is formed, causing an electric field which pushes the charge carriers back to their origin. Electrons are pushed back into the *n*- and holes back into the *p*-region. When the thermodynamic equilibrium is reached, a space charge region is formed at the *pn*-junction where no free charge carriers are present.
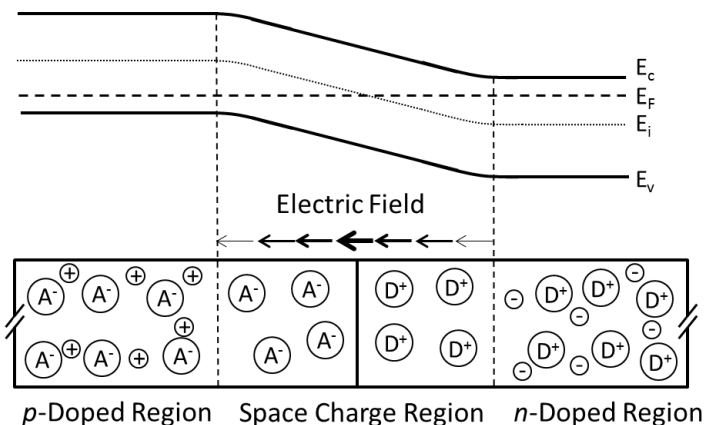
Figure 3.1: Upper image: Band diagram at a *pn*-junction including the conduction and valence band energies E_c and E_v, the Fermi energy E_F and the intrinsic energy E_i. **Lower image**: Scheme of a *pn*-junction between a *p*-doped and an *n*-doped semiconductor. At the contact a space charge region is formed. The resulting electric field points from *n* to *p* and has its maximum at the metallurgical contact.

Figure 3.1 shows a scheme of a *pn*-junction in thermodynamic equilibrium including the corresponding band diagram. The band diagram illustrates the energies of the conduction and the valence band as a function of the position along the *pn*-junction. Far from the junction, and hence, outside the space charge region, the band energies are constant. Within the space charge region band bending occurs and the relative difference of the bands to the Fermi energy changes.

If a positive voltage is applied from the *p*- to the *n*-region, the width of the space charge region is reduced. The *pn*-junction is in forward bias and a current will flow. If a negative voltage is applied, the width of the space charge region is increased and the current is blocked.

3.2.2 Schottky-Junction

A Schottky junction is formed, when a metal and a semiconductor are brought into contact. In this case, majority carriers diffuse from the semiconductor to the metal, leaving either acceptors in a *p*- or donors in an *n*-doped semiconductor behind. This, the same way as at a *pn*-junction, generates an electric field, which pushes the majority carriers back into the semiconductor. This means, the electric field at a metal to *p*-type contact points from the metal to the semiconductor and pushes the holes back. At a metal to *n*-type semiconductor contact the electric field points toward the metal and pushes the electrons back into the semiconductor.

Figure 3.2 illustrates a Schottky junction between a metal and an *n*-type semiconductor. The band bending and the resulting electric field are indicated. If a Schottky junction is unfavoured, a highly doped semiconductor is introduced close to the metal leading to an Ohmic contact.
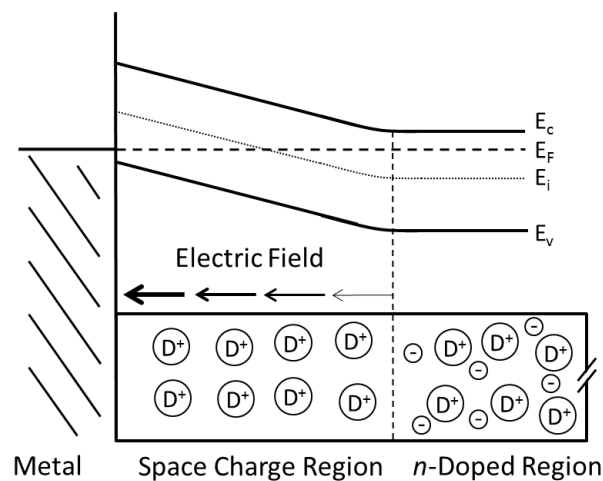
Figure 3.2: Upper image: Band diagram at a Schottky-junction between a metal and an *n*-doped semiconductor including the conduction and valence band energies E_c and E_v, the Fermi energy E_F and the intrinsic energy E_i. **Lower image**: Scheme of a Schottky-junction between a metal and an *n*-doped semiconductor. At the contact a space charge region is formed. The resulting electric field points from *n* to the metal and has its maximum at the metallurgical contact.

4 Materials and Methods

4.1 Equipment

Scanning electron microscope	JEOL JSM 6490LV
Micromanipulators	Kleindiek Nano Control NC30
Micromanipulator tips	Various Tips from Picoprobe and Micromanipulator
Sourcemeter	Keithly 2636A System Sourcemeter
Current amplifier	Stanford Research Systems Model SR570 Low-Noise Current Preamplifier
AD-converter	AdWin Pro II
Lock-in-amplifier	Stanford Research Systems Model SR830 DSP Lock-In Amplifier
SRP tool	SSM2000
SRP analysis program	NANOSRP Analysis
Heating stage	Anton Paar DHS 1100
Grinding machine	Struers Knuth-Rotor
Grinding papers	Struers SiC Grinding Paper 500, 800, 1000 and 4000
Silver paint	Electrolube Silver Conductive Paint

4.2 Samples

All samples used in this thesis were provided by Infineon AG. This section should give an overview of the different kinds of samples that have been investigated and and give some basic description of semiconductor devices used.

4.2.1 Raw Wafer Samples

To be able to compare measurements on proton doped silicon samples, also raw silicon samples have been investigated. These samples have been sliced or broken from either 6 inch (150 mm) or 8 inch (200 mm) raw silicon wafers. These samples consist of a polished top surface covered with native silicon oxide only and a rather rough backside with a thicker oxide layer. Both n- and p-doped, Czochalski and float-zone produced raw silicon samples in a resistivity range from $0.02\,\Omega$cm to more than $1000\,\Omega$cm have been used.

4.2.2 Proton Doped Silicon Samples

A raw p-doped Czochralsky grown silicon wafer has been implanted through the front side (top surface). The resistivity of the raw material was higher than $1000\,\Omega$cm. The wafer was implanted with $4\,\mathrm{MeV}$ protons at an implantation dose of $2 \cdot 10^{14}\,\mathrm{H}^+/\mathrm{cm}^2$ and annealed for one hour at temperatures from $100\,^\circ$C to $1000\,^\circ$C.

4.2.3 Devices

A ready produced CoolMOS$^{\mathrm{TM}}$ device has also been investigated. The device had not yet been packaged but delivered as a whole wafers. From this wafer samples have been prepared for the investigations.

4.3 Scanning Electron Microscopy (SEM)

Scanning Electron Microscopy is one of the most widely used analysis methods in semiconductor failure analysis. As the name indicates, it is a method to visualize small objects using the interaction of an electron beam with the analysed matter. The scheme of a scanning electron microscope used in this thesis is illustrated in figure 4.1 showing the main components of such an instrument. Electron microscopy will be described in this chapter according to the electron microscope used. Further applications will be mentioned but not discussed.
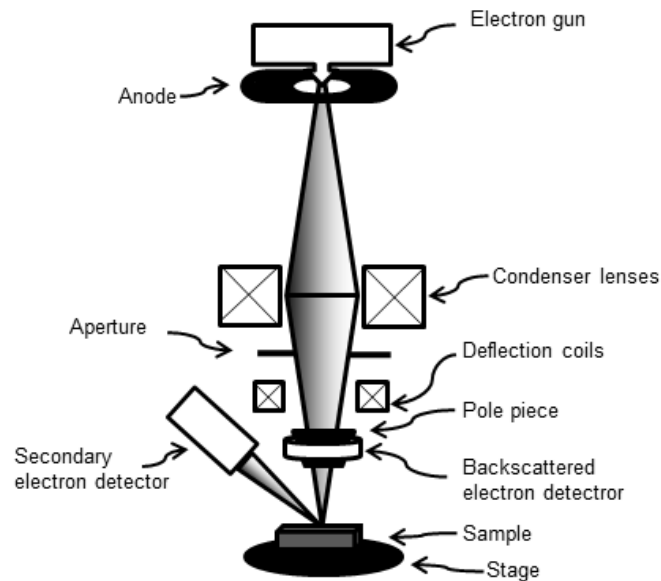
Figure 4.1: Scheme of a Scanning Electron Microscope, JEOL JSM 6490LV as it was used in this thesis.

As a charged particle beam is used in a scanning electron microscope, the whole system has to be in vacuum to diminish interaction of the beam with atoms or molecules in the gas phase. Usual pressures used in SEM are 10^{-6} mbar for the electron column and $10^{-4} - 10^{-5}$ mbar for the chamber. In the JEOL 6490LV, a pre-vacuum down to 10^{-2} mbar is generated by rotary pumps. Then a oil diffusion pump reduces the pressure to the favoured conditions.

The primary electron beam is generated in the electron gun. In this SEM, the electron beam is generated by heating a tungsten filament and extracting the electrons using an electric field. Additionally the electrons are accelerated to the favoured energy. Electron beam energies between a few hundred eV and 30 keV are used. The condenser lenses focus the beam while the aperture decreases the beam diameter and hence the energy spreading of the beam energy. The beam enters the specimen chamber via the pole piece and is scanned over the specimen using deflection coils.
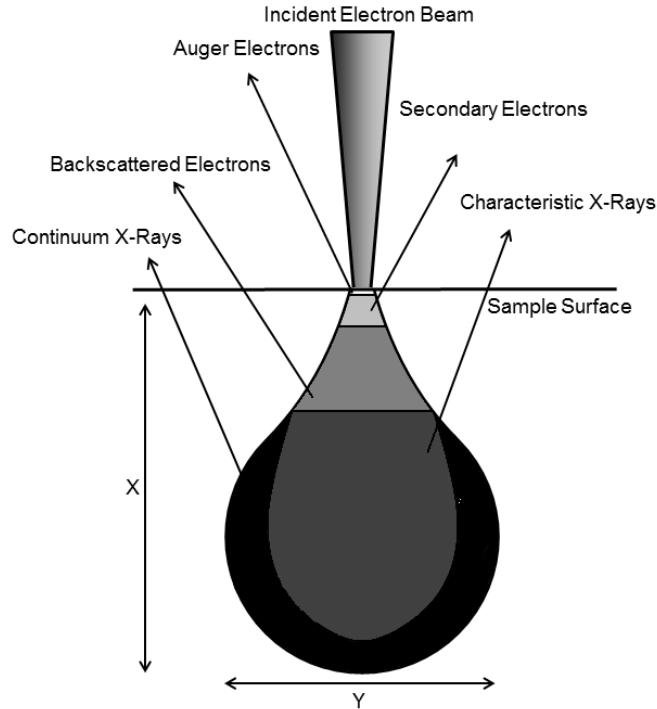
Figure 4.2: Pear-shaped interaction volume of an electron beam with a sample. The arrows show the different kinds of radiation produced by the incoming electron beam.

When the accelerated electrons penetrate the sample, elastic as well as inelastic scattering will occur. Due to the scattering, the interaction volume of the beam with the sample is much higher than the actual beam diameter (see figure 4.2). In reference [11] the extension of the interaction volume is calculated. The penetration depth X in µm can be approximated from

$$X = \frac{0.1 E_0^{1.5}}{\rho_m},\qquad(4.1)$$

where E_0 is the beam energy in keV and ρ_m is the mass density of the specimen in g/cm^3. The lateral extension Y in µm of the interaction volume is approached using

$$Y = \frac{0.077 E_0^{1.5}}{\rho_m}.\qquad(4.2)$$

Figure 4.3 shows the dependence of the penetration depth and lateral extension of the diffusion length from the beam energy.

Another reference in literature [12] gives an other dependence of the depth of the interaction volume, or electron range, as it is called there. The electron range R_G in elements of atomic numbers from 10 to 15 can be calculated using :

$$R_G = \frac{0.0389 E_0^{1.75}}{\rho_m}\qquad(4.3)$$
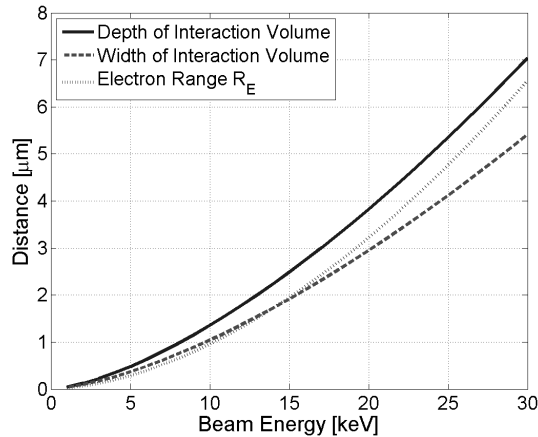
Figure 4.3: Scaling (depth and width) of the interaction volume of the incident beam and electron range R_E in silicon ($\rho = 2.34\,\mathrm{g/cm^3}$) in relation to the beam energy according to [11] and [12].

In table 4.1 a scheme of the different kinds of radiation produced by the interaction of the beam with the specimen is listed. Each kind of radiation carries specific informations about the sample:

Table 4.1: Radiation types after interacting with an electron beam.

Radiation	Measurement Techniques	Information
Auger electrons	AES*	Examination of the chemical composition of the very surface
Secondary electrons	Secondary Electron Detection	Imaging of the surface topography, voltage or potential contrast
Backscattered electrons	Backscattered Electron Detection	Imaging of differences in the chemical composition
Characteristic X-rays	EDX*	Averaged chemical composition of the interaction volume

*Not available in the electron microscope used in this thesis.

A detailed description of scanning electron microscopy can be found in [13].

4.3.1 Backscattered Electron Detection - Elastic Scattering

If incident electrons electrostatically interact with atomic nuclei it comes to elastic scattering, where electrons are scattered while loosing only a small fraction of their energy. Most of these scattering events occur at deflection angles of less than $90\,^\circ$, hence the electrons which undergo such a scattering stay in the sample. Nevertheless a small fraction of electrons are scattered at higher deflection angles and due to their high energy can leave the specimen. These electrons are called backscattered electrons and can be collected with a detector, which is in most cases fixed close to the pole piece (see figure 4.1).

High angle elastic scattering is proportional to the atomic number Z^2. Thus also backscattered electron signal increases with the atomic number. This means that regions on the sample surface

containing light elements (carbon or silicon) give a small backscattered electron signal while areas containing heavy elements (gold, tungsten) lead to a high signal. If the backscattered electron signal is captured and plotted against the position of the beam on the sample surface an atomic mass contrast image is obtained. As the kinetic energy of the backscattered electrons is high (almost the same as primary beam electrons), electrons scattered in quite a distance from the sample surface (up to some µm) can leave the specimen. So not only information about the very surface but also of the bulk is obtained.

4.3.2 Secondary Electron Detection - Inelastic Scattering

Inelastic scattering leads to an energy transfer of the primary beam electrons to the sample. This energy leads to excitations of inner-shell electrons. The relaxation of these excited states leads to emission of so called secondary electrons. As the energy of secondary electrons is small (less than 100 eV) and the probability of inelastic scattering depends inversely on the kinetic energy, the mean free path of secondary electrons in the specimen is very small (a few nm). As a consequence only secondary electrons generated within a depth of usually less than 2 nm are emitted from the sample into the vacuum. These electrons are then collected using an Everhart-Thornley detector. This type of detector consists of a collector grid, a scintillator and a photomultiplier. The emitted SE are attracted towards the collection grid by a positive voltage. Then they are accelerated towards the scintillator. At the scintillator each impacting electron generates, depending on the kinetic energy, up to several 100 photons which then are guided to a photomultiplier where the signal is amplified by several orders of magnitude. The amplified signal is then collected and plotted as a function of the position of the beam on the specimen.

As a result of the small escape depth of the electrons the signal strongly depends on the structure of the surface. While flat areas release only a small number of secondary electrons, the signal is very high at edges and corners. Additionally a "shadow effect" is introduced by positioning the Everhart-Thornley detector at a certain angle to the sample. Structures whose surface point towards the detector generate a higher signal than structures that point away from it.

4.3.3 Sample Preparation

For an investigation with SEM, samples have to be prepared in a certain way. Depending on the position to investigate and its size, the specimen has to be diced and ground. It can also be decorated using special acids or bases (e.g. hydrofluoric acid for highlighting oxides). As the electron beam causes a current, either due electrons leaving the specimen or incoming ones, the sample (surface) has to be conducting. If the sample itself isn't conducting, a layer of metal or carbon is deposited using physical vapour deposition (sputtering or thermal evaporation).

4.3.4 Voltage (Potential) Contrast

A further development of the secondary electron detection is the voltage, or potential contrast measurement. The number of secondary electrons generated and emitted at a certain region on the specimen is dependent on the potential of this region. Changing the potential leads to a change in the detected SE signal. While a positive specimen bias results in a reduction of the emission of secondary electrons, a negative bias leads to an increase of the secondary electron signal. If there are regions in the sample which differ by doping type or carrier concentration, an applied bias voltage changes their potential to a different extent. If the difference in the change is high enough, it is possible to obtain a contrast between these regions. This method is usually performed using a frequency dependent signal (Lock-In-Technique) [14] but it is also possible to see a voltage contrast without chopping the beam.

Figure 4.4 shows a voltage contrast measurement on a super-junction MOSFET device. At 0 V bias the secondary electron signal appears to be homogeneous over the whole specimen (4.4a). If -5V are applied to the sample from top to bottom (4.4b), a potential contrast can be observed, separating the p-doped columns from the n-doped bulk.
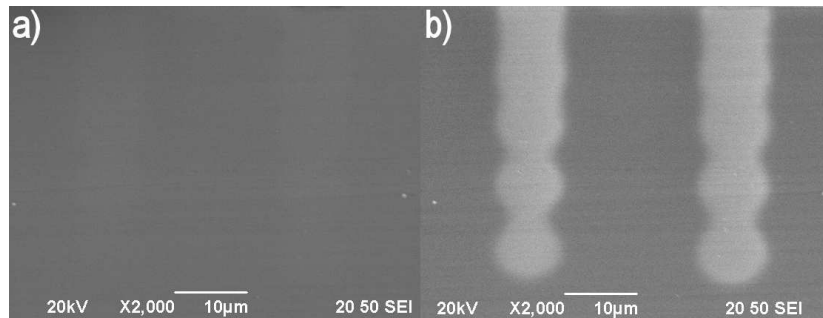
Figure 4.4: Voltage Contrast of p-columns in a super-junction MOSFET. The bias is applied from top to bottom. a) 0 V bias Voltage; b) -5 V bias Voltage

4.4 Electron Beam Induced Current (EBIC)

EBIC measurement techniques are used in semiconductor failure analysis to visualize internal electric fields (e.g. Schottky- or *pn*-junctions).

4.4.1 Physics of EBIC

If an electron beam interacts with a sample it produces different kinds of radiation (see section 4.3). Additionally electrons and holes are generated, which can diffuse around in the sample and can be separated at built in electrical fields, e.g. at Schottky- or *pn*-junctions. If both sides of such a junction are electrically contacted, an electron beam induced current can be collected (see figure 4.5).
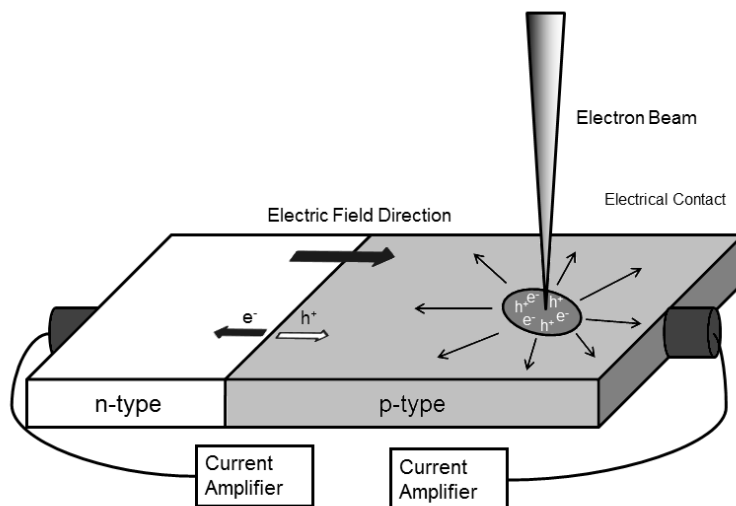
Figure 4.5: Scheme of an EBIC measurement. The electron beam induces electrons and holes which diffuse to the *pn*-junction. While electrons are pulled over the junction by the built-in electric field, the holes are pushed back. The separated charge carriers are collected at the current contacts and amplified using current amplifiers. One of the amplifiers can as well be replaced by a ground contact.

The electron beam induced current is proportional to the number of charge carriers $n(x)$, which are separated at the electric field. $n(x)$ can be derived from the charge continuity equation

$$\frac{\delta n(x)}{\delta t} = G(x) + \frac{1}{q}\nabla J_n(x) - Rec(x), \tag{4.4}$$

where $G(x)$ is the generation term, $J_n(x)$ is the current density and $Rec(x)$ stands for the recombination.

$G(x)$ describes the number of charge carriers generated at position x of the specimen. It strongly depends on the acceleration voltage and the beam current. Usually $G(x)$ is assumed to be constant in every point.

The current density can be described as

$$J_e(x) = q n_e(x) \mu_e E(x) + D_e q \nabla n_e(x) \tag{4.5}$$

for electrons and

$$J_p(x) = q n_p(x) \mu_p E(x) - D_p q \nabla n_p(x) \tag{4.6}$$

for holes, where q is the elementary charge, μ_e and μ_p are the mobilities and D_e and D_p are the diffusion constants of electrons and holes. The diffusion constant is related to the mobility by the the Einstein relation

$$D = \frac{\mu k_B T}{q}. \tag{4.7}$$

Diffusion is the movement of charge carriers along a concentration gradient while drift is motion due to an electric field.

In the relaxation approximation, the recombination term $Rec(x)$ has the form

$$\frac{n(x) - n_0}{\tau(x)}. \tag{4.8}$$

$\tau(x)$ is the (minority carrier) lifetime and can be made up of different components

$$\frac{1}{\tau(x)} = \frac{1}{\tau_{\text{vol}}(x)} + \frac{1}{\tau_{\text{sur}}(x)}. \tag{4.9}$$

While τ_{vol} depends on the concentration of recombination centres in the volume, τ_{sur} is kept constant over the whole sample. The contribution of τ_{sur} is controlled via the surface preparation. The volume where electrons and holes are generated is a limiting factor for the resolution of EBIC scans. This has to be taken into account especially if higher beam energies are used. While the width of the generation volume in silicon is about $0.25\,\mu m$ at $5\,kV$, it increases to more than $3\,\mu m$ at $20\,kV$ (see figure 4.3). A collection of references on EBIC techniques can be found in reference [15].

4.4.2 Sample Preparation and Assembling

As for SEM analysis (4.3.3) also for EBIC measurement the samples have to be prepared. For cross sectional measurements, the specimen is diced and ground. The grinding is a crucial step in the preparation for an EBIC measurement because it has a direct influence on the surface recombination rate. Preparation procedures are listed in table 4.2.

The grinding was performed using silicon carbide grinding paper. For shallow grinding (cross sections, after dicing) SiC 1000 and SiC 4000 paper was used. SiC 1000 stands for thousand meshes per inch in the sieve which was used for sieving the silicon carbide grains. This corresponds to a maximum grain size of $25\,\mu m$. For grinding through the whole specimen, like in the case of the planar view analysis of the CoolMOS device, SiC 500 ($50\,\mu m$), 1000 ($25\,\mu m$) and 4000 ($6\,\mu m$) have been used. The side walls of the proton doped samples were roughened using SiC 800 ($32\,\mu m$) paper.

Table 4.2: Preparation Procedures for EBIC measurements

Sample	Position	Procedure
CoolMOS	Cross Section	Dicing; no grinding due to metallization
CoolMOS	Planar View	Dicing; gluing on a piece of silicon; grinding with SiC Paper from the backside through the whole sample with a small bevel angle
Proton Doped Silicon	Cross Section	Dicing; Grinding with SiC Paper; drying with compressed air; roughening of the side walls with SiC paper; painting of side-walls with silver paint
Proton Doped Silicon	Planar View	Dicing, Grinding with SiC Paper; drying with compressed air
Raw Silicon Samples	Planar View	Dicing, grinding with SiC Paper from the backside through the backside-oxide

For planar view measurements, the sample is fixed on a specimen holder using adhesive carbon tape and mounted in the SEM. Cross sectional measurements are performed in a special holder. It consists of two copper cylinders which are pressed to the side walls of the sample by a spring. The copper cylinders are isolated against each other and each one is contacted to a current feed through of the SEM. Figure 4.6 shows the two specimen holders for cross sectional (a) and planar view (b).
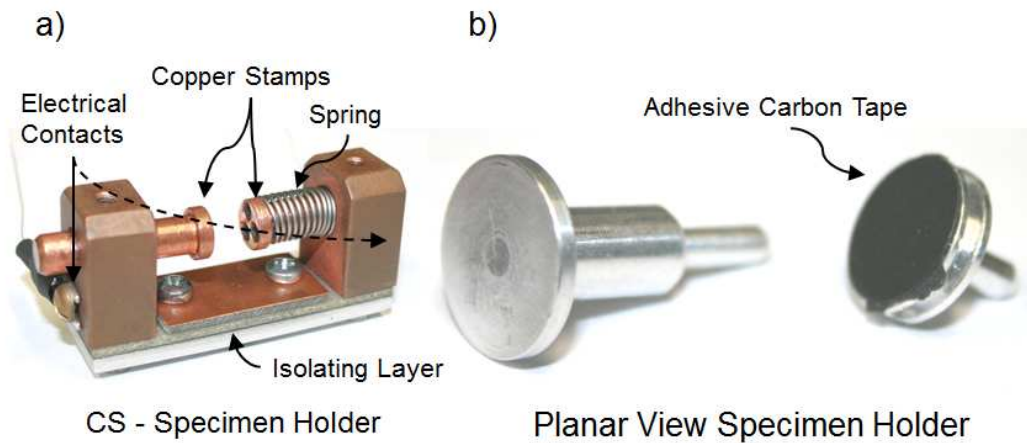
Figure 4.6: Specimen holders for EBIC measurement. **a)** shows a holder for cross sectional, **b)** one for planar view measurements.

4.4.3 EBIC Measurement Techniques

Dependent on the information one wants to derive from an EBIC measurement, there are several measurement techniques. In each method the electron beam deflection is externally controlled and the beam is scanned over the specimen using an AD-Converter. The EBIC signal is then collected as a function of position of the electron beam.

EBIC Line Scan

For an EBIC line scan the beam is scanned in a line across the sample. Usually this is done perpendicular to a *pn*-junction (see figure 4.7). Away (in the *n*-type region) from the space charged region the EBIC signal is low due to the absence of an electric field. The dominant contribution to the signal is the diffusion of minority carriers which can diffuse over into the space charged region and get separated. As the position of the beam moves towards the space charged region, the signal increases. In the space charged region the drift component adds to the signal which then reaches its maximum at the metallurgical junction (if the carrier concentrations in the *n*-type and p-type region are the same). The analysis can be done in planar view as well as on the cross section of a sample. If the cross section is investigated, buried junctions parallel to the surface can be investigated. For a usual line scan 1920 points are measured and plotted. The dwell time lies at $20\,\mu s$ which corresponds to an averaging of the EBIC signal over one $50\,\mathrm{Hz}$ period to diminish noise in the line current.
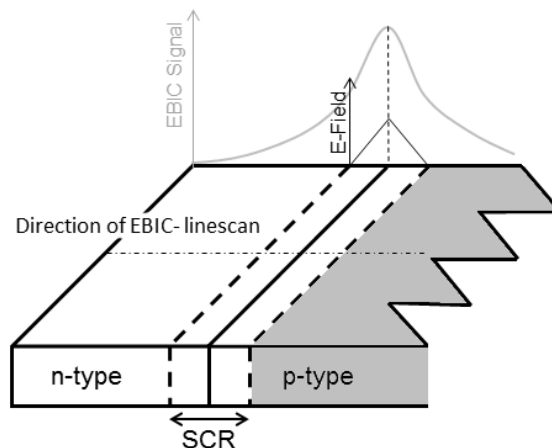
Figure 4.7: Scheme of a space charge region at a *pn*-junction. The distribution of the electric field is schemed as well as the EBIC signal

An EBIC line scan can provide information about the position of a *pn*- or a Schottky junction. In addition the diffusion length can be distracted from the decay of the signal (see Diffusion Length Measurement).

EBIC 2D-Scan

For a two dimensional EBIC image, several line scans in constant intervals are made on the sample and fused to a two dimensional image. The contrast in these images is either due to built-in electrical fields in the specimen or because of differences in defect concentrations (recombination centres). EBIC 2D-scans are plotted as contour, gray-scale or three dimensional plots.

EBIC Chop-Scan(AC-EBIC-Scan)

A usual EBIC scan is performed under steady-state-conditions. This means the beam is held on one place and after a certain dwell time it is moved to the next measurement point. If a bias voltage is applied to the sample, a direct current will flow. Even if the sample contains a reverse biased junction, there will be a leakage current. This leakage current is often several orders of magnitude bigger than the EBIC signal. Therefore an additional EBIC measurement method was introduced.

In an EBIC chop-scan the beam is "chopped" between the measurement point and a point that gives no EBIC signal. Usually a grounded tip or the specimen holder is used as points of no EBIC signal. The AC signal is then amplified using a lock-in-amplifier. The dwell time is set to $67\,\mu$s resulting in a "chopping frequency" of $7.5\,$kHz. In this way, the DC-part of the signal is filtered and only the EBIC-depended AC-part is measured. Hence also biased samples can be measured.

Schottky-Junction-EBIC Measurement

This method has been first described in [16]. If a metal tip is brought into contact with a semiconductor sample, bend bending occurs and a Schottky junction is formed (see section 3.2.2). Depending on the energy of the conduction E_c and the valence E_v band relative to the Fermi Energy E_f of the metal used, the bands band in different directions. If E_f of the metal is similar to E_f of the semiconductor (as for tungsten and silicon) the direction of the bend bending and the direction of the resulting electric field is only dependent on the doping type of the semiconductor. If the semiconductor specimen is n-doped, the bands will bend up at the Schottky junction, resulting in an electric field pointing towards the metal (figure 4.8a). If the doping type of the semiconductor is p, the bands will bend down and the electric field will point towards the semiconductor (figure 4.8b).

If electrons and holes are generated in the surroundings of a Schottky junction, an EBIC-signal can be measured. Depending on the direction of the electric field this electron beam induced current can change sign. If the EBIC-signal is collected with a current amplifier connected to the tip, the electron beam induced current is positive for a metal to n-type, and negative for a metal to p-type junction. Figure 4.9 shows a scheme of a Schottky-junction-EBIC measurement.

Micromanipulators with tungsten tips, like shown in figure 4.10 are used to contact the samples. These manipulators are moved using a combination of piezo-crystals and stick-slip motors and can be manoeuvred in the x-, y- and z-direction.
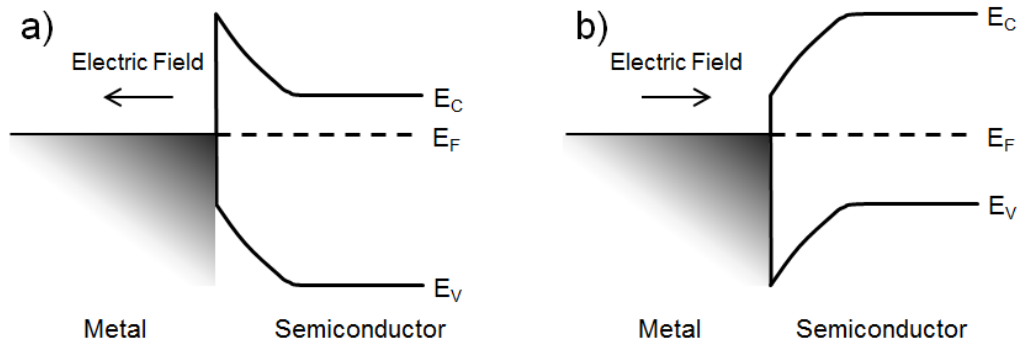
Figure 4.8: Scheme of the band-bending at a metal to *n*-type (**a**) and a metal to *p*-type (**b**) Schottky junction with the resulting direction of the electric field.
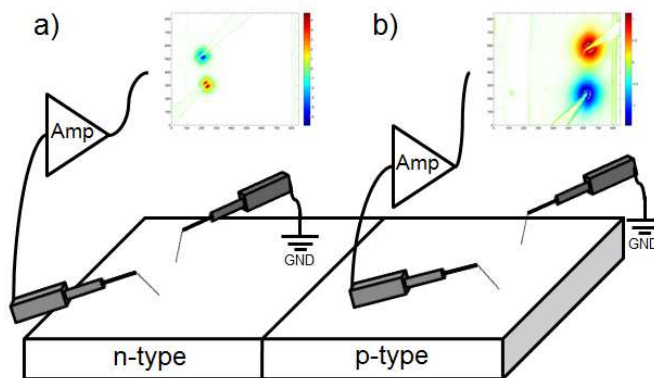
Figure 4.9: Scheme of two Schottky-EBIC measurements on an **a)** *n*-doped and **b)** *p*-doped region. In each measurement, the electron beam induced current is collected and amplified with one tip, while the second tip is contacted to ground potential. Red color in the contour plot means a positive current while blue implies a negative one.
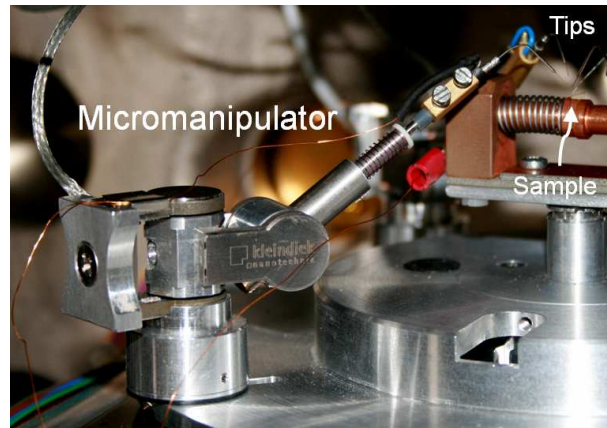
Figure 4.10: Micromanipulator in a SEM chamber. On the very right four tips make contact to a thin sample ($\sim$100 μm) mounted in the cross section specimen holder.

Diffusion Length Measurement

One charge carrier property that can be extracted from EBIC scans is the diffusion length L_D. Far from the electric field the movement of charge carriers is mostly dependent on concentration gradients. Due to the generation of electron hole pairs, the charge carrier concentration is locally increased leading to diffusion of these charge carriers along the concentration gradient. In thermal equilibrium the concentration of minority carriers is far lower than the concentration of majority carriers. Hence the generation of excess carriers has a higher influence on the concentration of minority carriers rather than on the majority carrier concentration and thus the diffusion length extracted from an EBIC measurement is more precisely the minority carrier diffusion length.

When the electron beam is scanned away from a junction the dependence between the current I_{EBIC} and the distance to the junction r under steady state conditions is given by [17] as

$$I_{\mathrm{EBIC}} \propto e^{-(r/L_D)}. \tag{4.10}$$

A configuration is assumed, where a *pn*-junction is parallel to the incident beam, and the incident beam is scanned perpendicular away from the junction (see figure 4.7). If the surface recombination velocity is negligible (v_s is zero), the relationship between the current and the distance according to [18] is given as

$$I_{\mathrm{EBIC}} = ke^{-(r/L_D)} \tag{4.11}$$

where k is a constant. The minority carrier diffusion length can be extracted, according to [19] as the negative inverse of the slope of

$$\ln I_{\mathrm{EBIC}} = -\frac{r}{L_D} + k \tag{4.12}$$

If v_s is infinite the decay can be approximated as

$$I_{\mathrm{EBIC}} = kr^{-(1/2)}e^{-(r/L_D)} \tag{4.13}$$

A generalized relationship of the induced current I_{EBIC} as a function of distance to the edge of the SCR at any surface recombination is given by [18] and [20] as

$$I_{\mathrm{EBIC}} = kr^{\alpha}e^{-(r/L_D)}. \tag{4.14}$$

where k is a constant and α is a fitting parameter used to linearise the $\ln(I_{\mathrm{EBIC}})$ versus r curve. For a pn-junction parallel to the incident beam, α is zero if v_s is zero (see 4.11) and α is $-1/2$ if v_s is infinite (see 4.13). If on the other hand, the configuration implies a planar junction, perpendicular to the incident beam, α is $-1/2$ when v_s equals zero and $-3/2$ if v_s is infinite [21, 22, 23]. If v_s is finite, α has a value between the two extrema. α can then derived from the fitting process of the linearisation of the $\ln(I_{\mathrm{EBIC}})$ versus r curve. [24] and [25] also present a method for extracting v_s from the α parameter.

Another measurement configuration which can be used for the extraction of the minority carrier diffusion length is the Schottky-junction-EBIC measurement. If a setup is used like illustrated in figure 4.9 the dependence of the signal decay to the diffusion length can be approximated as presented on the following pages.

The main difference to the configuration described above is the profile of the junction which causes the charge carrier separation and hence the EBIC signal. Instead of a pn-junction, which is parallel to the incident beam and has a large area, a Schottky junction is responsible for the charge carrier separation which is approximated as a point.
The carrier generation $G(\vec{r})$ is approximated by a delta function $G_0\delta(\vec{r})$ leading to following expression for the continuity equation:

$$D\nabla^2(n - n_0) + G_0\delta(\vec{r}) - \frac{n - n_0}{\tau} = 0, \tag{4.15}$$

where $n - n_0$ is the excess minority carrier concentration. Under the condition of a negligible surface recombination, the dependence of the minority carrier concentration of the distance to the point of generation r is given by

$$n - n_0 = \frac{G_0}{4\pi r}e^{-(r/\sqrt{D\tau})}. \tag{4.16}$$

As $L_D = \sqrt{D\tau}$ this equation can also be written as

$$n - n_0 = \frac{G_0}{4\pi r}e^{-(r/L_D)}. \tag{4.17}$$

As the EBIC signal is directly proportional to the excess carrier concentration, provided that the surface recombination is negligible, the decay of the EBIC signal can be approximated as

$$I_{\mathrm{EBIC}} \propto \frac{1}{r}e^{-r/L_D}. \tag{4.18}$$

The minority carrier diffusion length can then be extracted as the negative inverse of the slope of

$$\ln(I_{\mathrm{EBIC}} \cdot r) = -\frac{r}{L_D}. \tag{4.19}$$

This technique is very sensitive to small changes in the current ($I_{\mathrm{EBIC}} + I_{\mathrm{offset}}$). Figure 4.11 shows three idealized signals plotted versus the distance r from the maximum of the signal
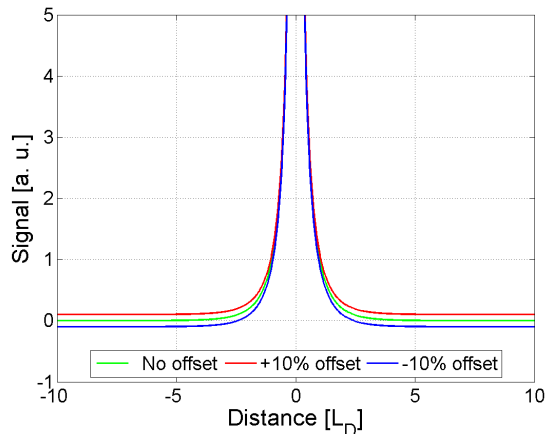
Figure 4.11: Idealized EBIC signal (green line) including signals with $+10\,\%$ (red line) and $-10\,\%$ offset (blue line).

as multiples of the diffusion length L_D. While one signal includes no offset current, an offset current of $\pm 10\,\%$ was added to the other two signals. The offset is given as a fraction of the signal at $r = L_D$.

In figure 4.12 the decay of the signal was linearised by plotting the logarithm of the signal times the distance to the maximum of the signal $[\ln(I \cdot r)]$ as a function of the distance. From this plot the slope from which the diffusion length is calculated can be extracted. It can be observed that the width of the region where all plots are linear, the extraction region, is rather small and strongly depends on the offset current. The higher the offset current the smaller becomes this region. The influence of the offset current on the diffusion length for different extraction regions is shown in figures 4.13. It can be observed that offset currents in the range of a few percent (of the signal at $r = L_D$) can already cause an error of several ten percent. The Schottky junction is formed with a metal tip. As the maximum of the EBIC signal is at the metal to semiconductor contact, the tip screens parts of the signal, including the maximum. Hence, especially for small diffusion lengths, the extraction region has to be chosen between one and two times L_D.
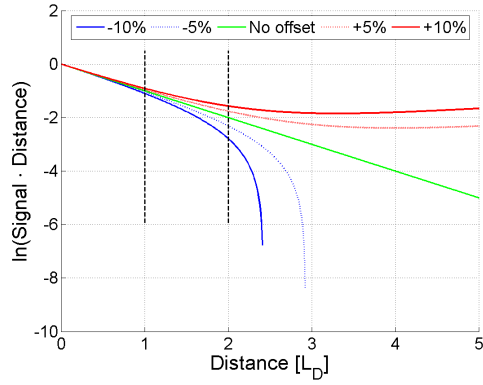
Figure 4.12: Idealized and linearised EBIC signal (green line) including signals with $+5\%$ and $+10\%$ (red lines) and -5% and -10% offset (blue line). The dashed line indicates the range in which the slope of the decay is extracted.
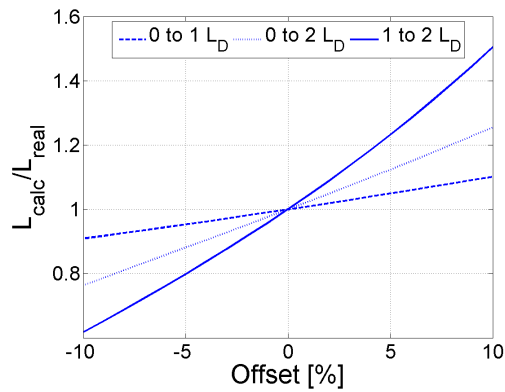
Figure 4.13: Ratio of calculated L_{calc} and real L_{real} diffusion length as a function of the offset current for different extraction regions.

4.5 Spreading Resistance Profiling (SRP)

SRP is a commonly used measurement in failure analysis for measuring dopant concentration and resistivity profiles. For this measurement a sample is diced and ground at a certain bevel angle. Then the analysis is performed by measuring the spreading resistance between two tungsten probes as a function of the depth profile. Using calibration curves this resistance profile is then converted into a carrier concentration and a resistivity profile.

Figure 4.14 shows a scheme of an SRP-tool. The tool mainly consists of an optical microscope, the probe mechanism and a stage.
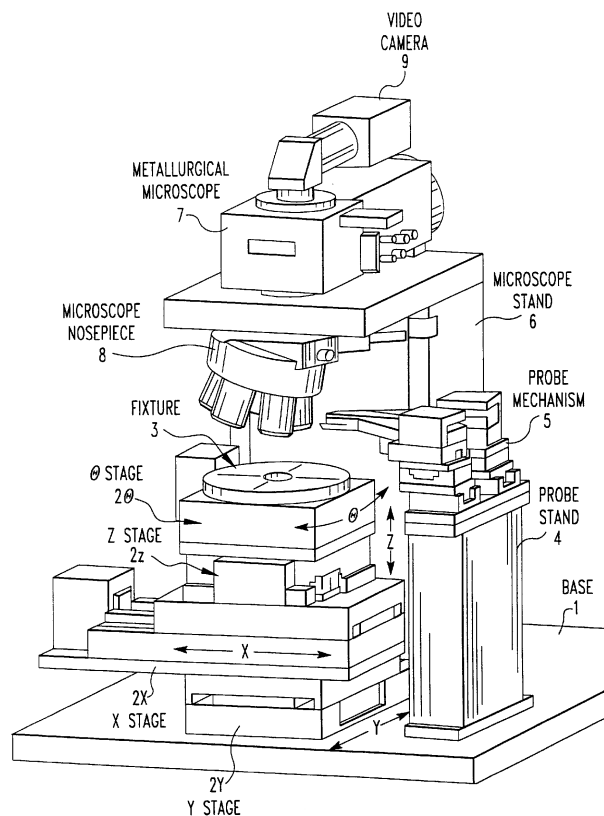
Figure 4.14: Spreading Resistance Profiling tool. The image has been taken from reference [26].

4.5.1 Theory

The following section should give an idea of the distribution of the potential in an SRP measurement. The Laplace equation for this geometry was solved by Peter Hadley.

Spreading resistance was introduced by Maxwell who was the first to investigate the electrical properties of point contacts (see reference [27]). He considered some material with a resistivity ρ that was divided into two halves by an insulating membrane. There is a hole with radius a in this membrane. If a voltage is applied across the membrane a current will flow through this hole. Maxwell showed that the resistance of the contact is $R = \rho/2a$. Most of the voltage drops close to this hole where the current density is high. Away from the hole the current

density almost goes to zero. As the electric field is proportional to the current density it also approaches zero far from the hole. The electrostatic potential is the integral of the electric field and is therefore constant far from the hole. To determine the potential Φ, Maxwell solved the Laplace equation for this geometry,

$$\nabla^2 \phi = 0. \tag{4.20}$$

It is convenient to solve this problem in oblate spheroidal coordinates $(\mu,\ v,\ \theta)$ which are defined as

$$x = a\cosh\mu \cos\nu \cos\theta, \tag{4.21}$$

$$y = a\cosh\mu \cos\nu \sin\theta, \tag{4.22}$$

and

$$z = a\sinh\mu \sin\nu. \tag{4.23}$$

with the restrictions $0 < \mu < \infty,\ -\pi/2 < \nu < \pi/2$ and $0 < \theta < 2\pi$ (see figure 4.15).
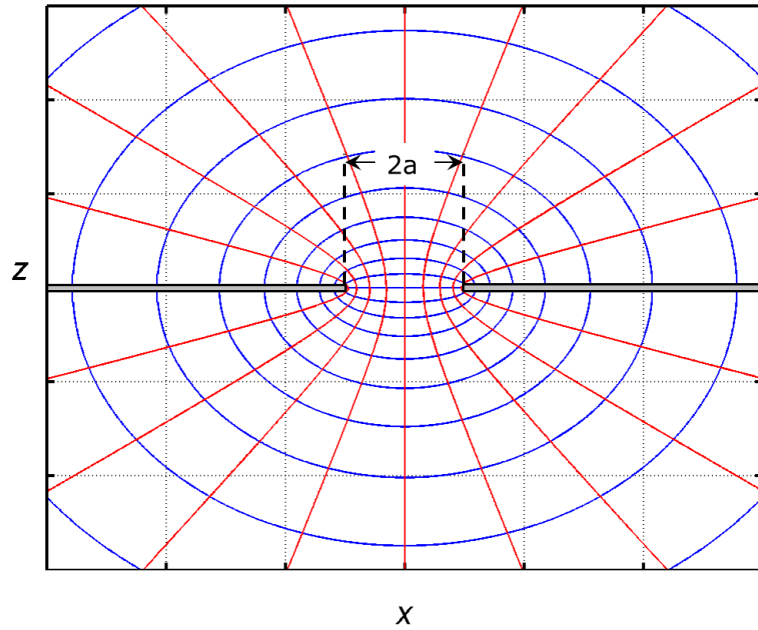
Figure 4.15: Distribution of the electric field for a current flowing through a round hole with radius a.
Red lines: Electric field lines (lines of a constant μ). The current flows parallel to the electric field.
Blue lines: Equipotential lines (constant v).

In these coordinates, the potential is only a function of μ. The Laplace equation in oblate spheroidal coordinates is

$$0 = \frac{1}{a^2 \left(\sinh^2\mu + \sin^2\nu\right)} \left[\frac{1}{\cosh\mu} \frac{\partial}{\partial\mu} \left(\cosh\mu \frac{\partial\phi}{\partial\mu} \right) + \frac{1}{\cos\nu} \frac{\partial}{\partial\nu} \left(\cos\nu \frac{\partial\phi}{\partial\nu} \right) \right] +$$
$$+ \frac{1}{a^2 \left(\cosh^2\mu + \cos^2\nu\right)} \frac{\partial^2\phi}{\partial\theta^2}. \tag{4.24}$$

Since Φ is only a function of μ, this reduces to

$$\frac{\partial}{\partial\mu}\left(\cosh\mu\frac{\partial\phi}{\partial\mu}\right) = 0. \tag{4.25}$$

This can written as

$$\cosh\mu\frac{d^2\phi}{d\mu^2} = -\sinh\mu\frac{d\phi}{d\mu}. \tag{4.26}$$

Let $y = \frac{d\phi}{d\mu}$, then

$$\frac{dy}{d\mu} = -\tanh\mu y. \tag{4.27}$$

This equation can be solved by the separation of variables,

$$\frac{dy}{y} = -\tanh\mu d\mu, \tag{4.28}$$

and integrated

$$\ln y = -\ln\left(\cosh\mu\right) + c_1. \tag{4.29}$$

Here c_1 is an integration constant. The result is exponentiated

$$y = \frac{d\phi}{d\mu} = \frac{\exp(c_1)}{\cosh\mu}, \tag{4.30}$$

and integrated again

$$\phi = 2\exp(c_1)\tan^{-1}\left(\tanh\frac{\mu}{2}\right) + c_2. \tag{4.31}$$

Here c_2 is another integration constant. As it is always possible to add a constant to a potential c_2 can be set to 0. The function $\tan^{-1}\left(\tanh\frac{\mu}{2}\right)$ approaches $\frac{\pi}{4}$ for large μ as shown in figure 4.16. If, for very large μ, a voltage $V/2$ is applied on one side and $-V/2$ is applied to the other
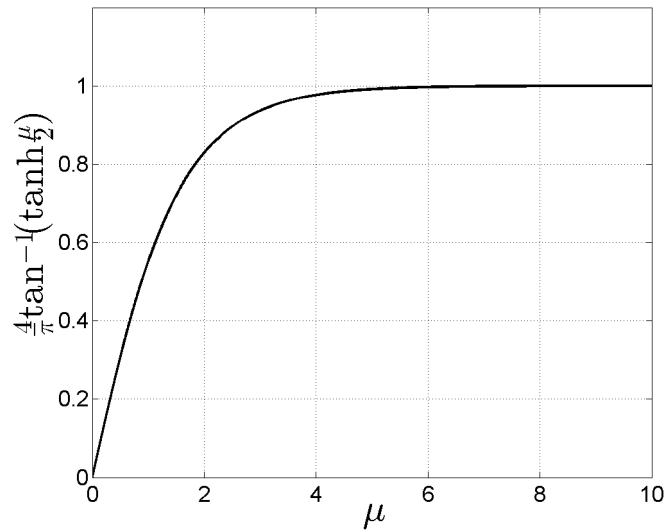
Figure 4.16: $\tan^{-1}\left(\tanh\frac{\mu}{2}\right)$ vs. μ

side of the membrane then the potential that satisfies these boundary conditions is

$$\phi = \frac{2V}{\pi} \tan^{-1}\left(\tanh\frac{\mu}{2}\right). \tag{4.32}$$

If this potential is substituted into the Laplace equation the electric field can be calculated as

$$\vec{E} = -\nabla\phi = -\frac{V\operatorname{sech}\mu}{\pi a\sqrt{\sinh^2\mu + \sin^2\nu}}\hat{\mu}. \tag{4.33}$$

The current density is proportional to the electric field:

$$\vec{j} = -\frac{\vec{E}}{\rho} = \frac{V\operatorname{sech}\mu}{\pi a\rho\sqrt{\sinh^2\mu + \sin^2\nu}}\hat{\mu}. \tag{4.34}$$

At $z = 0$ and $\mu = 0$ the current density is,

$$\vec{j}(z=0) = -\frac{V}{\pi a\rho\sin\nu}\hat{z}. \tag{4.35}$$

The integration of the current density over the hole yields the current which is passing through. At $z = 0$, the current density only points in the z-direction. Furthermore, the current density does not depend on θ as it is cylindrically symmetric around the z-axis. The current density only depends on the distance from the z-axis, $s = \sqrt{x^2 + y^2}$. The current is

$$I = \int_0^a 2\pi j(s) s \, ds. \tag{4.36}$$

Because of the cylindrical symmetry, the integration can be performed in x-direction, yielding

$$I = -2\pi \int_0^a \frac{V}{\pi a\rho\sin\nu} x \, dx. \tag{4.37}$$

At $z = 0$, $x = a\cos\nu$ and $dx = -a\sin\nu d\nu$

$$I = 2\pi \int_{\pi/2}^0 \frac{Va\cos\nu}{\pi\rho} d\nu = \frac{2aV}{\rho}. \tag{4.38}$$

The spreading resistance is the voltage divided by the current

$$R = \frac{\rho}{2a}. \tag{4.39}$$

This result can be used to rewrite the expressions for the potential, the electric field and the current density in terms of the total current I:

$$\phi = \frac{\rho I}{\pi a} \tan^{-1}\left(\tanh\frac{\mu}{2}\right). \tag{4.40}$$

$$\vec{E} = -\frac{\rho I\operatorname{sech}\mu}{2\pi a^2\sqrt{\sinh^2\mu + \sin^2\nu}}\hat{\mu}. \tag{4.41}$$

$$\vec{j} = \frac{I \operatorname{sech}\mu}{2\pi a^2 \sqrt{\sinh^2\mu + \sin^2\nu}} \hat{\mu}. \tag{4.42}$$

The current density does not depend on the resistivity. This means that for two materials on both sides of the membrane with the resistivity ρ_1 and ρ_2 the potentials on both sides can be calculated independently. The spreading resistance in this case is

$$R = \frac{\rho_1 + \rho_2}{4a}. \tag{4.43}$$

If there is a highly conductive material on the one side of the membrane and a poorly conducting material on the other side, $\rho_1 \ll \rho_2$ the spreading resistance is

$$R = \frac{\rho_2}{4a}. \tag{4.44}$$

This formula is used to determine the resistivity of semiconductors when a round metal contact is placed on the surface of the semiconductor (see figure 4.17). In this calculation, Ohm's law
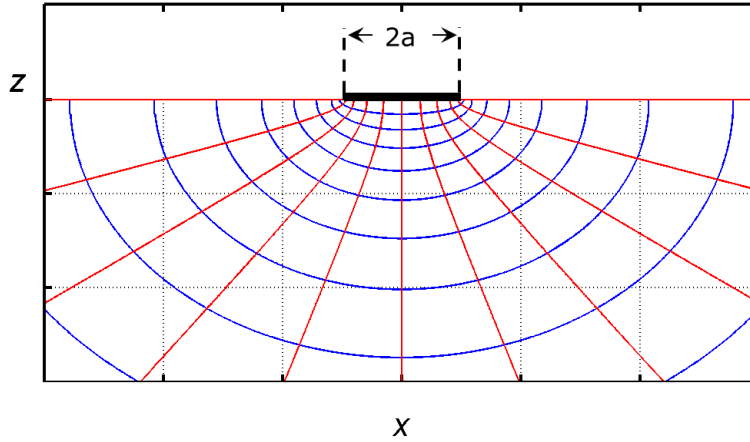
Figure 4.17: Distribution of the electric field for a current flowing from a round metal contact to a semiconductor. **Red lines**: Electric field lines. The current flows parallel to the electric field. **Blue lines**: Equipotential lines.

$\rho\vec{j} = \vec{E}$ is used . This means that the transport is assumed to be in the diffusive limit. For this to be true, a should be larger than the electron mean free path l. If a is on the order of l, then modifications of this result described in [28] and [29] need to be considered.

In SRP two metal tips are placed on a semiconductor, hence two metal semiconductor contacts with radii a_1 and a_2 are formed. The position of these contacts are $x = -d/2$ and $x = -d/2$. To determine the resulting potential, the potentials of two single contacts can be added:

$$\phi = \frac{\rho I}{\pi} \left(\frac{1}{a_1} \tan^{-1}\left(\tanh\frac{\mu_1}{2}\right) - \frac{1}{a_2} \tan^{-1}\left(\tanh\frac{\mu_2}{2}\right) \right). \tag{4.45}$$

In the $y = 0$ plane,

$$\mu_1 = \cosh^{-1}\left(\frac{\sqrt{\left(x + \frac{d}{2} + a_1\right)^2 + z^2} + \sqrt{\left(x + \frac{d}{2} - a_1\right)^2 + z^2}}{2a_1}\right) \tag{4.46}$$

and

$$\mu_2 = \cosh^{-1}\left(\frac{\sqrt{\left(x - \frac{d}{2} + a_2\right)^2 + z^2} + \sqrt{\left(x - \frac{d}{2} - a_2\right)^2 + z^2}}{2a_2}\right). \tag{4.47}$$
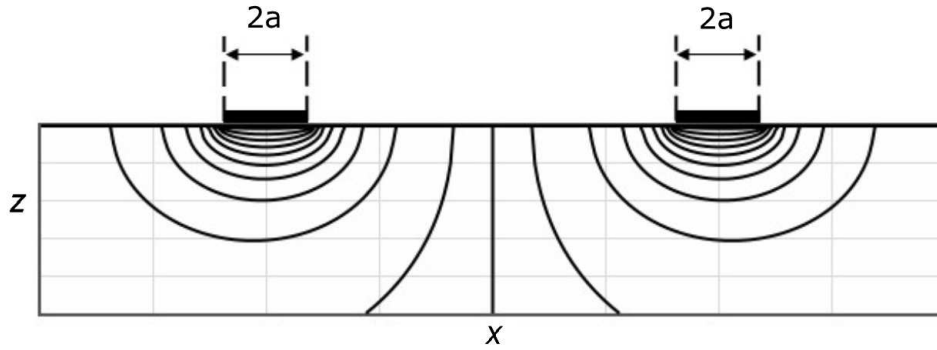
Figure 4.18: Distribution of the equipotential lines in an SRP measurement, when the current is passed from one contact to the other.

Figure 4.18 shows the equipotential lines when current is passed from one electrode to the other. It shows that most of the voltage falls near the contacts. The potential at the surface, where $y = 0$ and $z = 0$ is used to calculate the voltage between the contacts. Along this line

$$\mu_1 = \cosh^{-1}\left(\frac{|x + \frac{d}{2}|}{a_1}\right) \tag{4.48}$$

and

$$\mu_2 = \cosh^{-1}\left(\frac{|x - \frac{d}{2}|}{a_2}\right). \tag{4.49}$$

The voltage between the contacts is

$$V = \frac{\rho I}{\pi}\left(\frac{1}{a_1}\tan^{-1}\left(\tanh\left(\frac{1}{2}\cosh^{-1}\frac{d - a_2}{a_1}\right)\right) + \frac{1}{a_2}\tan^{-1}\left(\tanh\left(\frac{1}{2}\cosh^{-1}\frac{d - a_1}{a_2}\right)\right)\right), \tag{4.50}$$

and the resistance is

$$R_{\mathrm{SRP}} = \frac{V}{I} = \frac{\rho}{\pi}\left(\frac{1}{a_1}\tan^{-1}\left(\tanh\left(\frac{1}{2}\cosh^{-1}\frac{d - a_2}{a_1}\right)\right) + \frac{1}{a_2}\tan^{-1}\left(\tanh\left(\frac{1}{2}\cosh^{-1}\frac{d - a_1}{a_2}\right)\right)\right). \tag{4.51}$$
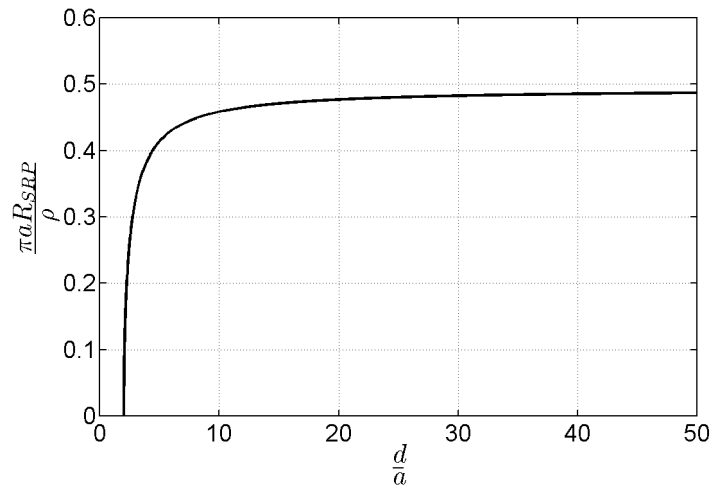
Figure 4.19: Spreading resistance as a function of the distance between the tips for $a=a_1=a_2$.

Figure 4.19 shows the spreading resistance for $a=a_1=a_2$ as a function of the distance between the tips. The resistance measured in an SRP experiment is only a weak function of the distance between the electrodes as soon as that distance is a few times the radius of the contacts. For $d < 2a$ the contacts overlap and the resistance is zero.

4.5.2 Sample Preparation

Being able to make reproducible contact to the specimen is crucial for good results in SRP. Therefore the probe surface as well as the sample surface have to be conditioned.

Probe Conditioning

For making good contact to the specimen the probes should meet several demands:

- reproducible electrical and physical penetration of the specimen

- reproducible electrical contact on both, n- and p-doped samples in a resistivity range from $<0.0001\,\Omega$cm to $>1000\,\Omega$cm

- stability over many thousands of measurement points

- generation of probe marks on the specimen

- very small contact area in relation to the probe spacing

To fulfil these requirements every now and then the probes have to be conditioned (see references [26, 30]). The conditioning procedure includes several grinding steps where the tip surface is roughened and sharpened. After each step the penetration of the probes into the specimen and the reproducibility of the electrical contact are measured using a PEN and QTA sample. After the conditioning the surfaces of the probes have to be stabilized. This is achieved by running

several hundred measurement points on a random ground sample. After this stabilisation, QTA and PEN are measured again. If the results of this measurement are satisfying, the probes can be used for actual measurements.

Sample Bevelling and Polishing

Before the measurement, the SRP sample has to be diced (in most times out of a wafer) and ground at a certain bevel angel. The bevel angel has to be chosen according to the depth of the profile of interest. The grinding is a very crucial step in SRP sample preparation as it is necessary to provide reproducible sample surfaces to guarantee comparable results. Depending on the bevel angle the specimen is first pre-ground and then polished, using a glass plate and a suspension of 0.1 μm diamond powder in sawing oil. Thereafter, for bevel angles smaller than 5°44', the bevel angel of the sample is measured using a goniometer.

Calibration

Figure 4.20 shows a SEM image of the imprints of one of the tips after an SRP measurement. One can see that the highlighted imprint consists of several micro-contacts rather than of only one round single contact. Thus the calculations shown in section 4.5.1, assuming round single contacts cannot be used. To transform the spreading resistance profiles into resistivity profiles a calibration has to be performed.
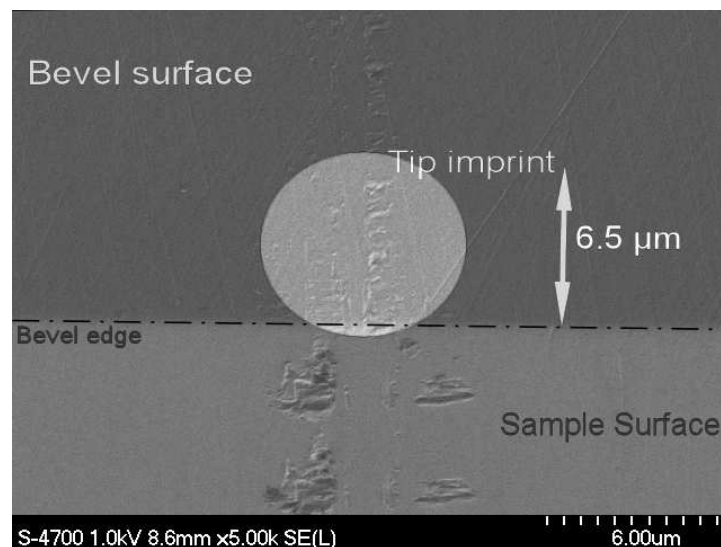
Figure 4.20: SEM image of SRP probe imprints. The bevel angle of the sample is 20°. The contact has a diameter of 6.5 μm.

Each time the quality of the tip imprints is changed a calibration curve has to be recorded. This can be due to a change of the tip surface (e.g. due to conditioning) or a change of the polishing procedure (e.g. scratches in the glass plate). For each doping type a separate calibration has to be done. Different lattice orientations require own calibration curves as well. Furthermore, if the measurement conditions such as probe load or step size are changed, further calibration curves have to be recorded.

Figure 4.21 shows calibration curves for phosphorous and boron doped <100> silicon with a probe load of 10 g and a step width of 5 µm. One can observe that the calibration curves don't yield the same resistivity for the same spreading resistance. This often leads to a step or a kink if there is a *pn*-junction in a resistivity profile.
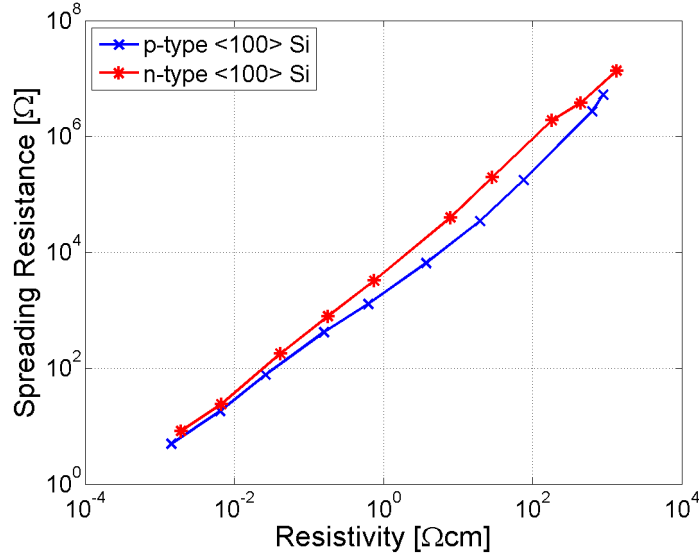
Figure 4.21: SRP calibration curves for *n*- (red line) and *p*- doped <100> silicon (blue line).

4.5.3 Measurement

In figure 4.22 the principle of an SRP measurement on a bevelled surface is shown. Sourcing a constant voltage of 5 mV between the tungsten probes the current is measured. The usual spacing of the probes is 40-50 µm. The measurement yields a spreading resistance profile. The resistivity $\rho(x)$ is then derived from the spreading resistance applying the calibration curve. Assuming a constant, known carrier mobility $\mu_{e,p}$, the carrier concentration $c_{e,p}$ can be calculated using

$$c_{e,p}(x) = e\frac{1}{\rho(x)\mu_{e,p}}, \qquad (4.52)$$

where e is the elementary charge. The resistivity profiles can also be converted into dopant profiles as explained in [31].

Usually the measurement is performed semi-automatically. Up to twelve already bevelled samples can be measured in one batch. The samples have to be aligned with the bevel edge and values for the bevel angle, the crystal orientation, the step size and the grain size of the grinding powder have to be inserted. The measurement is then performed automatically.
Also the analysis of the measured spreading resistance is performed semi-automatically. Information such as the position of a *pn*-junction and the doping type of each region have to be given to the program in order to receive the resistivity and dopant concentration profiles from the spreading resistance profile.
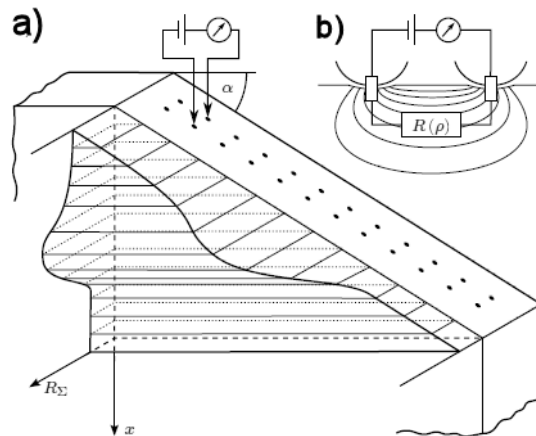
Figure 4.22: a): Scheme of an SRP measurement. The scheme shows the sum of the resistance derived from the contact and the doping of the substrate.
b): Equivalent circuit diagram of the SRP method. The image has been taken from reference [6].

One of the disadvantages of this measurement is that, although it claims to provide profiles in nano-scale, the measurement is performed in quite lager dimensions. The step size between the measurement points is 5 µm while the spreading of a space charge region is in the same scale or smaller. Therefore it is quite impossible to measure the increase in resistance, which would lead to a minimum in the charge carrier profile in such a region. Even if the step size is lowered (it can be lowered to 2.5 µm), the paths of the current can be much more propagated. This makes it quite impossible to visualize exact positions of space charged regions, as well as *pn*-junctions.

Due to the bevelling the resistivity profile obtained from the spreading resistance measurement doesn't correspond completely to the actual profile without bevelling [32, 33]. The measured spreading resistance does not only depend on the resistivity of the layer, the tips make contact to, but also to the layers underneath. If these layers are better conductors, the spreading resistance will be smaller, if these layers are insulating, the spreading resistance will increase. The smaller the bevel angel, the higher the influence of this effect on the profile. For the correction of this influence to the resistivity profile various correction methods have been published [34, 35, 36]. As these algorithms are very sensitive and react on minor changes of the input resistance, the the noise level has to be very small. To keep the noise at a low level, the raw data has to be smoothed [37, 38]. The correction and smoothing was performed using an analysis program belonging to the SRP instrument.

4.6 Four-Point-Resistivity Measurement

Another important characteristic of charge carriers, or of material in general is the resistivity ρ. The resistivity is defined as the ratio of the electric field E to the current density j

$$\rho = \frac{E}{J}. \tag{4.53}$$

The resistivity carries information about the density and the mobility of electrons

$$\frac{1}{\rho} = n_e e \mu_e \tag{4.54}$$

and holes

$$\frac{1}{\rho} = n_p e \mu_p \tag{4.55}$$

in semiconducting materials, where n_e and n_p are the carrier densities, e is the elementary charge and μ_e and μ_p are the carrier mobilities. As shown in 4.5, it is possible to calculate the resistivity from a spreading resistance profile. Nevertheless, as SRP is not a direct measurement it is recommendable to find other, direct measurements to validate the results of SRP.

L. B. Valdes [39] presented a direct measurement technique of ρ using four metal tips on a semiconductor sample for a certain configuration of the tips. In this section a generalization of this method regarding the positioning of the contacts as well as the boundary condition of an edge of the sample is presented.

When a current contact is placed on a flat sample of uniform resistivity and a current I is sourced, the current density $\vec{j}$ below this contact is

$$\vec{j} = \frac{I}{2\pi r^2} \vec{r}. \tag{4.56}$$

If there are two current contacts and the current is sourced from r_1 to r_2 the current density is given by

$$\vec{j} = \frac{I_{12}}{2\pi} \left(\frac{\vec{r} - \vec{r_1}}{|\vec{r} - \vec{r_1}|^3} - \frac{\vec{r} - \vec{r_2}}{|\vec{r} - \vec{r_2}|^3} \right). \tag{4.57}$$

This is true for a homogeneous, infinite sample. If the current contacts are placed close to an edge, the boundary condition of the current being zero at the edge has to be taken into account. This is done by introducing two additional imaginary contacts (at $\vec{r_1}'$ and $\vec{r_2}'$) which are mirrored opposite the real contacts with regard to the edge of the specimen. This leads to the equation

$$\vec{j} = \frac{I_{12}}{2\pi} \left(\frac{\vec{r} - \vec{r_1}}{|\vec{r} - \vec{r_1}|^3} - \frac{\vec{r} - \vec{r_2}}{|\vec{r} - \vec{r_2}|^3} + \frac{\vec{r} - \vec{r_1}'}{|\vec{r} - \vec{r_1}'|^3} - \frac{\vec{r} - \vec{r_2}'}{|\vec{r} - \vec{r_2}'|^3} \right). \tag{4.58}$$

From this, the electric field distribution can be calculated:

$$\vec{E} = \rho \vec{j} = \frac{\rho I_{12}}{2\pi} \left(\frac{\vec{r} - \vec{r_1}}{|\vec{r} - \vec{r_1}|^3} - \frac{\vec{r} - \vec{r_2}}{|\vec{r} - \vec{r_2}|^3} + \frac{\vec{r} - \vec{r_1}'}{|\vec{r} - \vec{r_1}'|^3} - \frac{\vec{r} - \vec{r_2}'}{|\vec{r} - \vec{r_2}'|^3} \right) \tag{4.59}$$

If now two additional contacts are placed on the surface (see figure 4.23 at $\vec{r_3}$ and $\vec{r_4}$, the potential difference between these tips V_{34} is given by

$$V_{34} = \frac{\rho I_{12}}{2\pi} \int_{r_3}^{r_4} \left(\frac{\vec{r} - \vec{r_1}}{|\vec{r} - \vec{r_1}|^3} - \frac{\vec{r} - \vec{r_2}}{|\vec{r} - \vec{r_2}|^3} + \frac{\vec{r} - \vec{r_1}'}{|\vec{r} - \vec{r_1}'|^3} - \frac{\vec{r} - \vec{r_2}'}{|\vec{r} - \vec{r_2}'|^3} \right) d\vec{r} \tag{4.60}$$
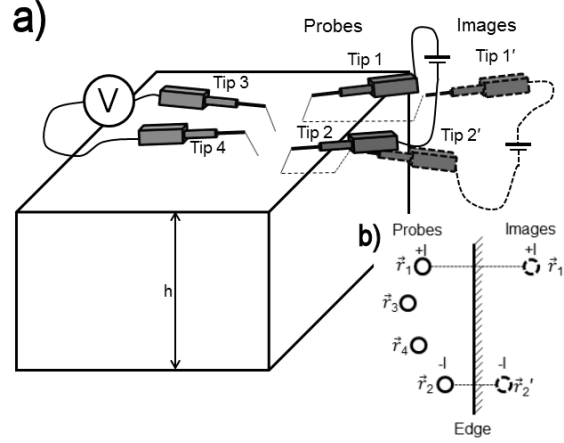
Figure 4.23: Scheme of a four-point resistivity measurement as an overview of the voltage measurement (**a**) and in planar view (**b**).

As $z = 0$ on the surface, the integration only has to be done for x and y.

$$
\begin{aligned}
V_{34} = \frac{\rho I_{12}}{2\pi} \int_{x_3}^{x_4} &\left(\frac{x - x_1}{[(x - x_1)^2 + (y_3 - y_1)^2]^{3/2}} - \frac{x - x_2}{[(x - x_2)^2 + (y_3 - y_2)^2]^{3/2}} + \right. \\
&\left. + \frac{x - x_1'}{[(x - x'1)^2 + (y_3 - y_1')^2]^{3/2}} - \frac{x - x_2'}{[(x - x_2')^2 + (y_3 - y_2')^2]^{3/2}} \right) dx - \\
- \frac{\rho I_{12}}{2\pi} \int_{y_3}^{y_4} &\left(\frac{y - y_1}{[(x_4 - x_1)^2 + (y - y_1)^2]^{3/2}} - \frac{y - y_2}{[(x_4 - x_2)^2 + (y - y_2)^2]^{3/2}} + \right. \\
&\left. + \frac{y - y_1'}{[(x_4 - x'1)^2 + (y - y_1')^2]^{3/2}} - \frac{y - y_2'}{[(x_4 - x_2')^2 + (y - y_2')^2]^{3/2}} \right) dy
\end{aligned}
\tag{4.61}
$$

After the integration the expression for V_{34} is

$$
V_{34} = \frac{\rho I_{12}}{2\pi} \left(\frac{1}{s_{31}} + \frac{1}{s_{31'}} + \frac{1}{s_{42}} + \frac{1}{s_{42'}} - \frac{1}{s_{41}} - \frac{1}{s_{41'}} + \frac{1}{s_{32}} + \frac{1}{s_{32'}} \right)^{-1},
\tag{4.62}
$$

where

$$
s_{mn} = \sqrt{(x_m - x_n)^2 + (y_m - y_n)^2}
\tag{4.63}
$$

This leads to the final expression for the resistivity in a four point measurement with one edge boundary condition:

$$
\rho = \frac{2\pi V_{34}}{I_{12}} \left(\frac{1}{s_{31}} + \frac{1}{s_{31'}} + \frac{1}{s_{42}} + \frac{1}{s_{42'}} - \frac{1}{s_{41}} - \frac{1}{s_{41'}} - \frac{1}{s_{32}} - \frac{1}{s_{32'}} \right)^{-1}.
\tag{4.64}
$$

This formula was implemented into a LabVIEW program which sweeps the current I_{12}, measures the voltage V_{34} and calculates the resistivity ρ.

For measurements on the surface of a sample without the boundary condition of an edge

$$
\rho = \frac{2\pi V_{34}}{I_{12}} \left(\frac{1}{s_{31}} + \frac{1}{s_{42}} - \frac{1}{s_{41}} - \frac{1}{s_{32}} \right)^{-1}.
\tag{4.65}
$$

was used. In this configuration $1/s_{31'}$, $1/s_{32'}$, $1/s_{41'}$ and $1/s_{42'}$ are 0 as the edge is very far away from the measured position, compared to the distance between the outermost tips.

4.7 Other Measurements

During this thesis a lot of other measurement methods which provide certain charge carrier properties have been discussed, but not applied. This section shows a selection of these methods.

4.7.1 Scanning Spreading Resistance Microscopy (SSRM)

SSRM bases on the principles of SRP. The main difference is the use of only one measurement tip while the second contact is fixed (see figure 4.24).
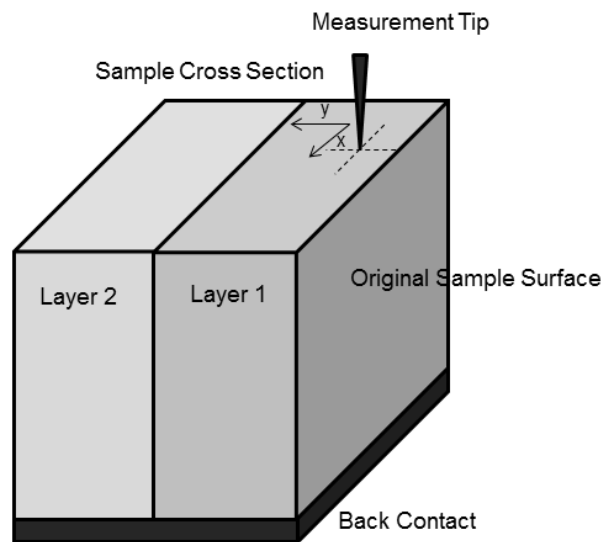
Figure 4.24: Scheme of an SSRM measurement on the cross section of a sample

The measurement tip, a sharp conductive AFM tip, is scanned over the sample and the resistance between the tip and the back contact is measured as a function of position. As most of the voltage drops close to the contact of the tip to the sample, only the resistivity of the sample in this region influences the overall resistance. Hence the resolution of this method is better than in usual spreading resistance profiling. The resistance map is then transformed into a resistivity or carrier map using a calibration function. An advantage to spreading resistance profiling lies in the possibility of measuring a two-dimensional carrier profile [40, 41, 42]. Furthermore the specimen don't necessarily have to be beveled, as the resolution of the measurement is already high without bevelling [43, 44, 45].

4.7.2 Microwave and RF-Techniques

The measurement of the interaction of semiconducting material with electromagnetic radiation is another possibility to quantify charge carrier properties. In [46] the dependence of microwave power transmission through a semiconducting sample on its conductivity is presented. Spatially resolution is achieved by guiding the microwaves with an antenna [47]. Another method is using radio frequency instead of microwaves [48].

4.7.3 Scanning Capacitance Microscopy (SCM)

Scanning capacitance microscopy is a measurement technique where the capacitance between a probe tip and a sample is measured as a function of position [49]. The method uses either an oxide layer [50] or the space charged region of a Schottky contact between the tip and a clean semiconductor surface [51] to probe the capacitance and can be performed one- or two-dimensional. The charge carrier density n can be calculated from the voltage derivative of the capacitance (dC/dV)[51] as

$$n = \frac{8(V_{bi} - V)^3}{q\epsilon_s} \left(\frac{dC}{dV}\right)^2,$$ (4.66)

where V_{bi} is the built-in potential across the junction, q is the charge of the carriers and ϵ_s is the dielectric constant of the investigated semiconductor. The method has a dynamic range from 10^{14} to $10^{20}\,\mathrm{cm}^{-3}$ [52] and a spatial resolution of less than $20\,\mathrm{nm}$ [53].

4.7.4 Haynes Shockley Experiment

For the Haynes Shockley experiment, a semiconductor specimen (mostly a rod) is exposed to a longitudinal electric field. Two point contacts (emitter and collector) are made on the specimen. Then minority carriers are introduced at the emitter and the signal is measured at the collector. From the Δt between the introduction of carriers and the measurement of the signal, the minority carrier mobility μ can be calculated from

$$\mu = \frac{L}{E\Delta t},$$ (4.67)

where L is the distance between the point contacts and E is the electric field [54].

4.7.5 Van der Pauw Method

For special specimens the resistivity and the mobility can be measured using the Van der Pauw method. This method uses, similar to the four-point resistivity measurement, four electrical contacts (A, B, C and D). A current is sourced between two contacts and the potential difference between the other two contacts is measured. For this experiment, following conditions have to be fulfilled:

- The electrical contacts have to be at the very edge of the sample.

- The contacts have to be small compared to the spacing between them.

- The sample has to be flat and homogeneous in thickness.

- The sample has to consist of a closed surface; there are supposed to be no holes in the sample.

The resistances $R_{AB,CD}$ and $R_{BC,DA}$ are measured, where

$$R_{AB,CD} = \frac{V_{CD}}{I_{AB}}$$ (4.68)

and

$$R_{BC,DA} = \frac{V_{DA}}{I_{BC}}.$$ (4.69)

The resistivity ρ is calculated from these resistances and the sample thickness t_s by

$$\rho = \frac{\pi t_s}{\ln 2} \frac{R_{AB,CD} + R_{BC,DA}}{2} f\left(\frac{R_{AB,CD}}{R_{BC,DA}}\right) \tag{4.70}$$

where f is a function of the ratio of $R_{AB,CD}/R_{BC,DA}$ [55].
If a magnetic field is applied perpendicular to the specimen, the Hall mobility μ_H is given by

$$\mu_H = \frac{t_s}{B_m} \frac{\Delta R_{BD,AC}}{\rho}, \tag{4.71}$$

where B_m is the magnetic field induction and $\Delta R_{BD,AC}$ is the resistance change due to the magnetic field.

5 Determination of Doping Type and Resistivity of Unknown Samples

This section should show how both, the doping type and the resistivity of raw silicon samples can be determined. Therefore two silicon raw wafer samples (S_1 and S_2) have been investigated using the Schottky-junction-EBIC (see section 4.4.3) and the four-point-resistivity method (see section 4.6).

5.1 Schottky-Junction-EBIC

For the Schottky-junction-EBIC measurement the samples have been ground and placed in the scanning electron microscope. Two tungsten micromanipulator tips were used to form the Schottky junctions. The figures 5.1 and 5.2 show the Schottky-junction-EBIC measurements on sample S_1 and S_2.
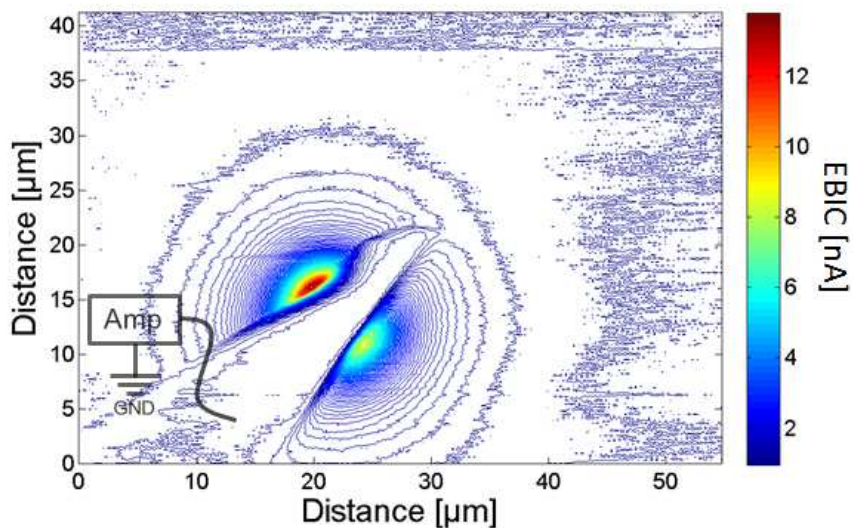
Figure 5.1: Schottky-Junction-EBIC measurement on unknown sample S_1.

At the Schottky junction in figure 5.1 a positive current (indicated with red color) is collected. Thus, according to section 4.4.3 the doping of S_1 is n-type.
Figure 5.2 shows a Schottky-junction-EBIC measurement on the sample S_2. In this figure, both Schottky junctions between the micromanipulator tips and the sample can be observed. The signal is collected with the lower tip (signalized with the current amplifier) which is called

measuring tip. The negative (blue) electron beam induced current at this tip indicates *p*-doping of the sample S_2. Although the electric fields at both junctions point in the same direction (in this case, from the tip to the semiconductor) the EBIC signals have an opposite sign. This is due to the signal being collected with only one tip. If charge carriers are generated at the second tip (upper tip), electrons will move via this tip to ground and thus holes will be collected by the measuring tip. This gives a positive signal (red) at the second tip. The EBIC signal at the second tip can be used as a verification of the signal at the measuring tip. If both tips make contact to the same doping regions, the currents induced at the junctions have to be of opposing sign. If the current direction is the same at both junctions, a *pn*-junction has to be in between.
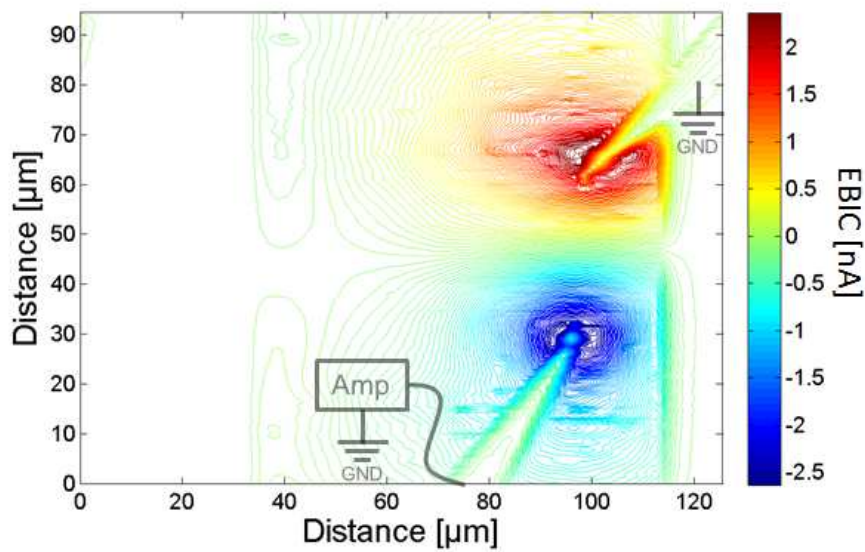
Figure 5.2: Schottky-Junction-EBIC measurement on unknown sample S_2.

5.2 Four-Point-Resistivity Measurements

The resistivity of the two raw silicon samples S_1 and S_2 was measured using the four-point resistivity measurement (see section 4.6). Figure 5.3 shows a four-point-resistivity measurement on sample S_1. A current in a range from -10 to 10 mA was used. In figure 5.3a the voltage measured between current source and sink (tip 1 and 2 in figure 4.23) is plotted against the sourced current. This plot is transformed to the IV characteristic of the contacts shown in figure 5.3b. The IV-curve is similar to the IV-curve of a double diode. This corresponds to what would be expected when two tungsten tips make contact to a semiconductor surface. According to equation 4.65 there has to be a linear relation between the sourced current I_{12} and the measured voltage V_{34}. Figure 5.3c proofs this for sample S_1 and the resistivity of the sample can be calculated using the tip positions obtained from figure 5.4 and given in table 5.1. ρ is calculated by inserting the slope V_{34}/I_{12} from figure 5.3c into formula 4.65. This gives a resistivity of $0.024\,\Omega$cm for the sample S_1 on this position.
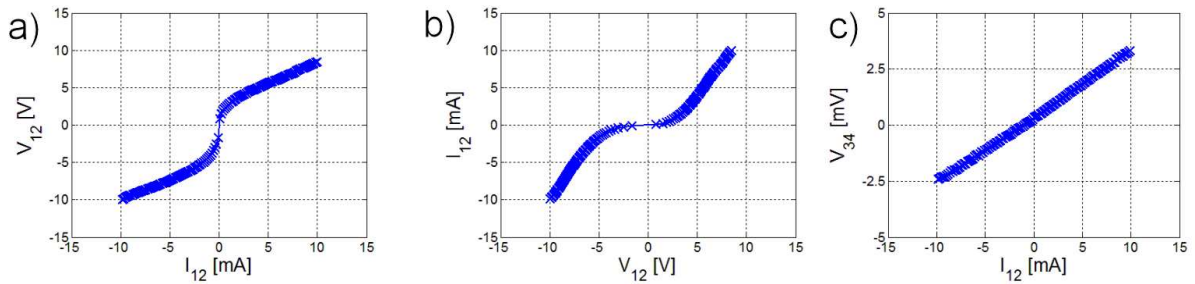
Figure 5.3: Four-Point-resistivity measurement on sample S_1. The indices of current and voltage axes are derived from the tip numbering in figure 4.23. **a)**: Voltage V_{12} between the current source and sink versus the sourced current I_{12}; **b)**: IV-characteristic between the current source and sink (derived by transposing 5.3a; **c)**: Potential difference V_{34} between the measurement tips versus the sourced current I_{12}.

Table 5.1: Positions of the micromanipulator tips in the four-point-resistivity measurement on sample S_1 derived from figure 5.4 .

	X-position [µm]	Y-position [µm]
Tip 1 (Current Source)	0	0
Tip 2 (Current Sink)	244.5	0
Tip 3 (Measuring Tip)	88	6.5
Tip 4 (Measuring Tip)	150	0
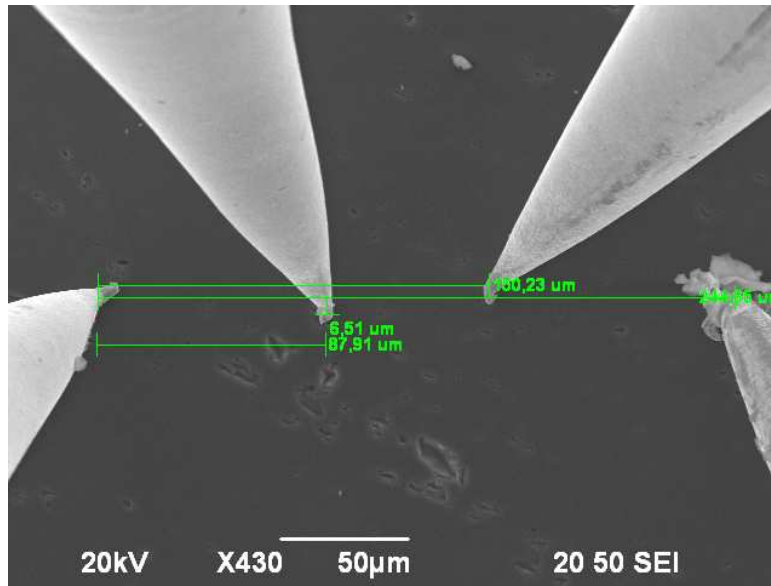
Figure 5.4: SEM image of a Four-Point-resistivity measurement on sample S_1. The positions of the tips have been measured and the relative distances are given in table 5.1.
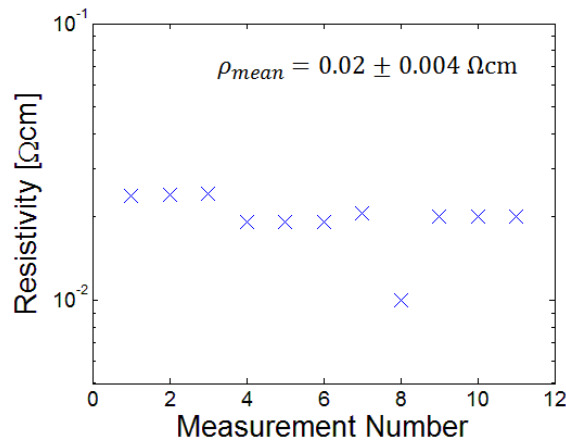
Figure 5.5: Average resistivity of the sample S_1 obtained from several measurements on different positions on the same sample.

The measurement was repeated on different positions of the sample leading to an average resistivity ρ_{mean} of $0.020 \pm 0.004\,\Omega$cm (see figure 5.5).

The resistivity of sample S_2 was also measured with the four-point-resistivity method. Figure 8.2 shows the results of such a measurement, performed from -7 to 7 μA. The sub-plots 8.2a and b correspond to the voltage vs. current and to the IV-characteristic between current source and sink. In the sub-plot 5.6c the measured voltage V_{34} is plotted versus the sourced current. This plot is almost linear and yields (inserted into the equation 4.65 and using the corresponding positions of the tips) a resistivity of 8200 Ωcm.
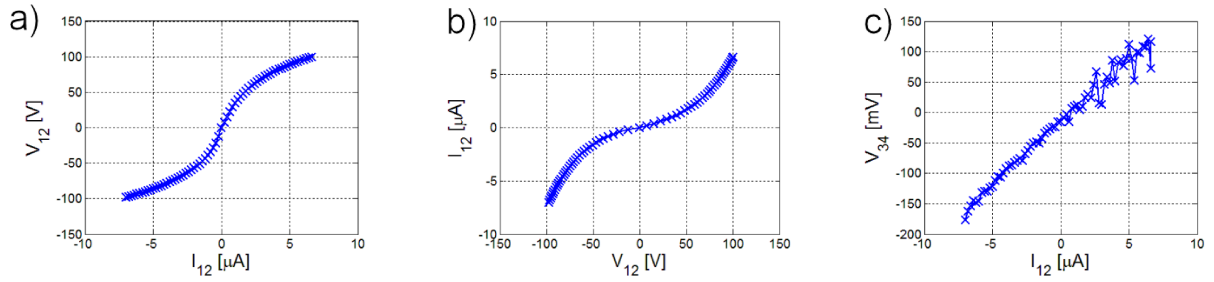
Figure 5.6: a-c): Four-point-resistivity measurement on sample S_2. The indices of current and voltage axes are derived from the tip numbering in figure 4.23. **a)**: Voltage V_{12} between the current source and sink versus the sourced current I_{12}; **b)**: IV-characteristic between the current source and sink; **c)**: Potential difference V_{34} between the measurement tips versus the sourced current I_{12}.
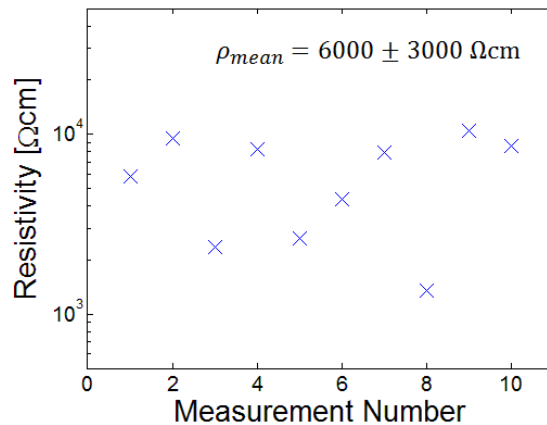
Figure 5.7: Average resistivity of sample S_2.

The four-point-resistivity measurements on S_2 showed a large variation of the results, leading to a mean resistivity ρ_{mean} for sample S_2 of $6000 \pm 3000 \, \Omega$cm (see figure 5.7).

5.3 Comparing Results to Values on Data Sheets

The two samples S_1 and S_2 correspond to raw wafers produced by the companies MEMC and SEH. Table 5.2 compares the measured properties to the corresponding values on the data sheets.

Table 5.2: Comparison of measured properties of S_1 and S_2 to values from data sheet.

Property	Sample S_1	MEMC wafer	Sample S_2	SEH wafer
Doping type	n-type	Antimony doped (n)	p-type	Boron doped (p)
Resitivity [Ω**cm**]	0.020 ± 0.004	$0.008 - 0.030$	6000 ± 3000	> 1000

The measured values fit to the expected ones and it can be stated that S_1 corresponds to the MEMC wafer and S_2 to the SEH wafer. The results of the measurements also show, that the four-point measurement seems to be better suited for samples with a small resistivity than for high resistivity samples. The Schottky EBIC technique works for both, n- and p-type samples with a resistivity of more than $1000\,\Omega$cm.

5.4 Conclusions

Two samples, S_1 and S_2, of unknown resistivity and doping type have been investigated. The doping type was determined using the Schottky-junction-EBIC method (see section 4.4.3) and the resistivity has been measured using the four-point-resistivity measurement (see section 4.6). S_1 has been identified as a $0.020 \pm 0.004\,\Omega$cm n-type silicon sample. The doping of S_2 has been determined to be p-type and a resistivity of $6000 \pm 3000\,\Omega$cm has been measured.

6 Annealing Series of Proton Doped Samples

One topic concerning proton doped silicon is the formation of different thermal donors (see section 3.1.3) dependent on the invested thermal budget. The identification of these thermal donors is of great interest. For this reason a series of proton doped samples was prepared and annealed at different temperatures. The influence of the temperature of this annealing step on the resistivity of the samples and on the doping type was investigated using EBIC and SRP.

6.1 Starting Material

A raw silicon wafer was used as starting material for these samples. In tables 6.1 and 6.2 some properties of the material can be found.

Table 6.1: Starting material for the annealing series.

Supplier	SEH
Dopant	boron
Single Crystal Growth	magnetic Czochralski
Crystal Orientation	<100>

Table 6.2: Characteristics of the starting material for the annealing series

Property	Average Value	Lower Limit	Upper Limit
Resistivity [Ωcm]		1000	
Wafer Diameter [mm]	200	199.8	200.2
Wafer Thickness [µm]	725	710	740
Oxygen Content [cm^{-3}]			$4.1 \cdot 10^{17}$

The silicon wafer was implanted with protons at a dose of 2×10^{14} H$^+$/cm ^{2} and an energy of 4 MeV leading to an implantation depth of about 165 µm. Thereafter the wafer was cut into pieces of 1×1 cm and placed into an annealing stage. The implanted and not annealed starting material is called original sample.

6.2 Annealing Procedure and Sample Preparation

The annealing step was performed using a DHS1100 heating stage (see figure 6.1). For the annealing procedure, the original sample was put on the annealing stage. The stage was closed with a graphite dome and flushed with nitrogen gas. During the annealing process there was a constant flux of nitrogen gas of $4\,\text{L/min}$. The stage was heated with a rate of $300\,°\text{C/min}$. At temperatures of more than $200\,°\text{C}$ the dome was cooled with compressed air. After the annealing, the sample was cooled down to room temperature. Depending on the annealing temperature, this cooling step took up to $20\,\text{min}$. The annealing time refers to the time between the point where the annealing temperature is reached and the starting of the cooling.
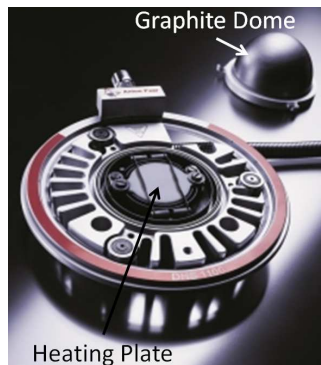
Figure 6.1: Annealing stage DHS1100 from Anton Paar.

After the cooling, the sample was sliced with a diamond pen into two $1 \times 0.5\,\text{cm}$ pieces. Subsequently one piece was prepared for the EBIC- and the other one for the SRP-measurement as described in the sections 4.4.2 and 4.5.2.

Table 13.1 on page 97 gives an overview on the samples produced and investigated with EBIC and SRP.

6.2.1 EBIC Analysis

The annealed samples have been investigated in the scanning electron microscope using the EBIC line-scan, EBIC 2D-scan and Schottky-junction-EBIC method.

The figures 6.2 and 6.3 show an EBIC-line-scan and an EBIC-2D-scan on the cross section of the original sample. The line-scan plot consists of two separate signals. Each signal derives from the same measurement and was detected with a separate current amplifier connected to the sample as illustrated in figure 4.5.

The peak of the EBIC signal in the line-scan is at a depth of $200 \pm 10\,\mu\text{m}$ from the sample surface. The error is derived from the measurement uncertainty of the distance measurement in the electron microscope which is assured to be lower than $5\,\%$. The maximum EBIC signal is induced at the maximum electric field which in this case derives from the *pn*-junction between the *n*-type, proton doped region and the *p*-type substrate material. In the region close to the surface (from $0 - 140\,\mu\text{m}$) no signal was detected. Due to the increase of the electron concentration towards the proton implantation peak (see figure 6.4b) band bending occurs

resulting in an additional electric field. The band bending is shown in figure 6.4a and was derived from simulations[1]. This electric field generated by this concentration gradient points towards the surface of the sample (left side), and hence, into the opposite direction to the electric field generated at the pn-junction. Minority carriers, which are holes in this case, generated in the region close to the surface of the sample would be dragged over to the backside by the electric field at the *pn*-junction. Nevertheless they are pushed back by the first electric field and don't even reach the *pn*-junction. Hence no electron beam induced current is detected.
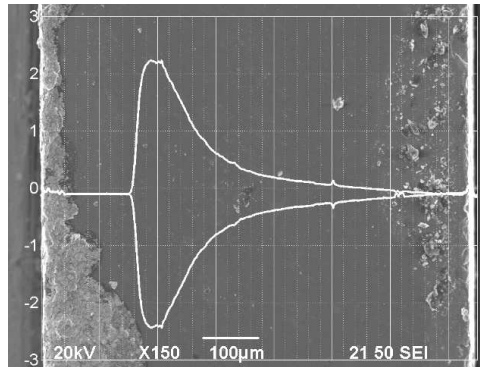
Figure 6.2: Combined SEM image and EBIC line-scan on the cross section of the original sample.

On the right side of the peak of the EBIC signal, the decay of the signal depending on the distance from the *pn*-junction can be observed. A range for the diffusion length of electrons in the *p*-substrate material can be estimated as described in section 4.4.3. The limits of the range are calculated assuming an infinite surface recombination velocity ($v_s = \infty$) for the maximal diffusion length and a negligible velocity ($v_s = 0$) for the minimal diffusion length. Figure 6.5 shows the extraction of these limits from the EBIC line-scan.

The measurements resulted in a minimum diffusion length of $126 \pm 13\,\mu$m and a maximum diffusion length of $221 \pm 22\,\mu$m. Thus, the range of the diffusion length of the minority carriers (electrons) in the substrate of the original sample can be narrowed down to $110 - 250\,\mu$m. A measuring error of $10\,\%$ was assumed.

---

[1]The simulations have been provided by Manfred Gruber.
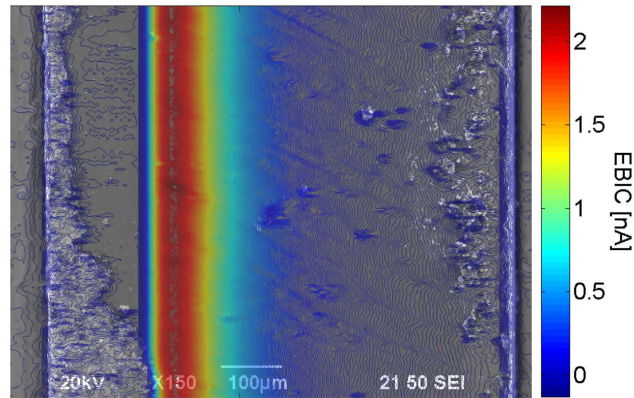
Figure 6.3: Combined SEM image and EBIC 2D-scan on the cross section of the original sample.
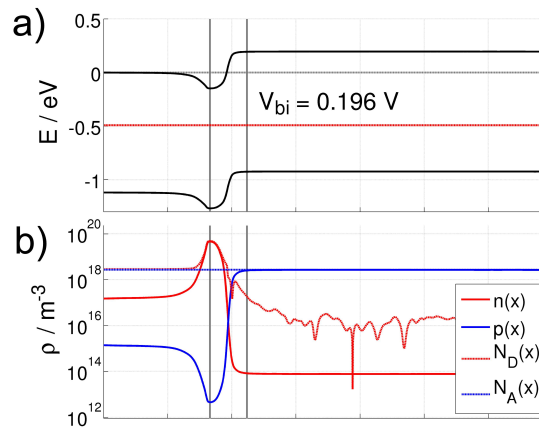
Figure 6.4: Simulation of **a)** the band diagram and **b)** the electron (red line) and hole (blue line) concentration along the cross section of the original sample.[1]
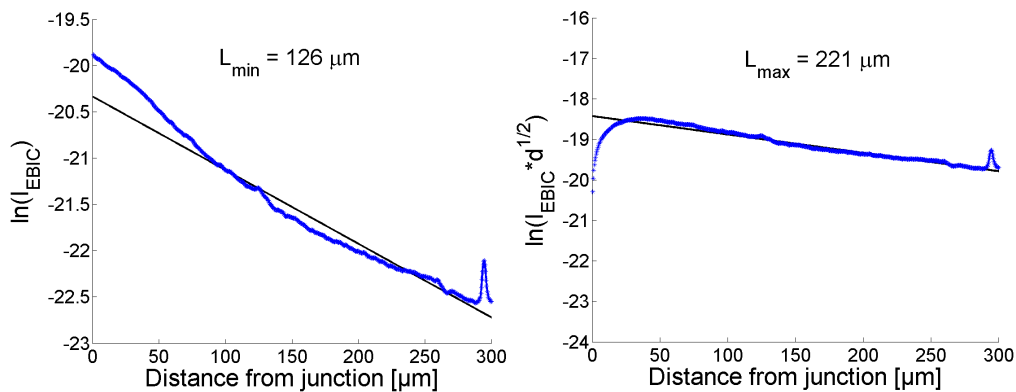
Figure 6.5: Extraction of the minority carrier diffusion length in the substrate region of the original sample from an EBIC line-scan. **Left image**: Minimal minority carrier diffusion length assuming no surface recombination. **Right image**: Maximal minority carrier diffusion length assuming an infinite surface recombination velocity.

6.2.2 Schottky-Junction-EBIC Measurements

The doping type of all samples of the annealing series was investigated using the Schottky-junction-EBIC method, as described in section 4.4.3. The figures 6.6 and 6.7 show two measurements on the proton implanted region and on the substrate of the original sample.
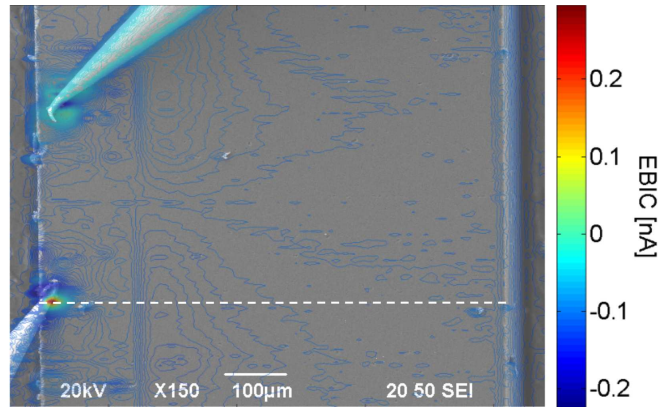
Figure 6.6: Schottky-junction-EBIC measurement on the implanted side of the original sample. The plotted signal was measured with the lower tip. The dashed line indicates the line-scan which was used to extract the diffusion length.

In both measurements the EBIC signal was recorded with the lower tip, reaching to the sample from the left side. The electron beam induced current generated close to the measuring tip in figure 6.6 is positive (red) and hence the doping type is determined to be *n* in this region. The EBIC generated at the measuring tip in figure 6.7 is negative, indicating *p*-doping. The EBIC generated at the second tip in this figure is positive, confirming this statement.
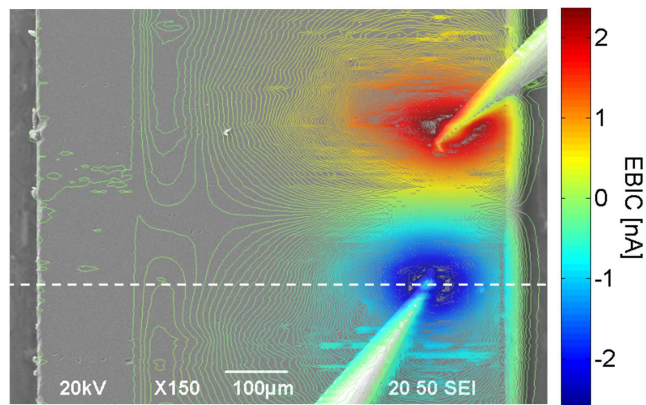
Figure 6.7: Schottky-junction-EBIC measurement on the substrate region of the original sample. The signal plotted was measured with the lower tip. The dashed line indicates the line-scan which was used to extract the diffusion length.

The diffusion length can be deduced from the measurements of the decay of the EBIC signal as a function of the distance to the Schottky junction (maximum of the EBIC signal) as described in section 4.4.3. Figure 6.8 shows a line-scan extracted from the Schottky-junction-EBIC

measurement in figure 6.6 along the dashed line.
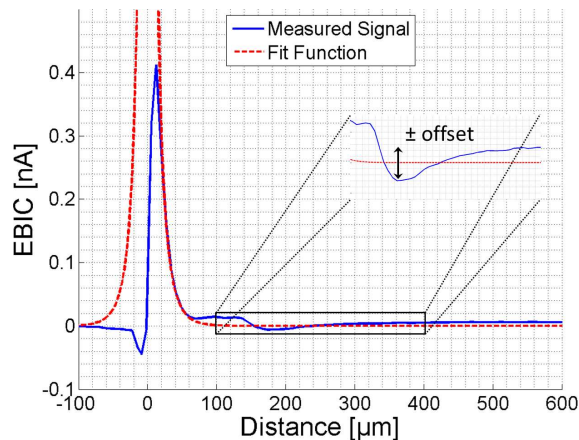
Figure 6.8: EBIC line-scan over a Schottky junction between a tip and the sample in the proton implanted region of the original sample. Blue line: data extracted from the dashed line in figure 6.6. Red dashed line: Fit function according to equation 4.19.

The line-scan passes the center of the Schottky junction and hence the maximum of the electron beam induced current. Unfortunately the tip hides this maximum leading to a dip in the line-scan. The position of the maximum is determined by fitting the measured signal to an idealized signal as in figure 4.11. The samples investigated include a *pn*-junction which also influences the signal in some way. It is assumed that the EBIC signal at the Schottky junction is not influenced if it is generated far from the *pn*-junction. Despite this, the *pn*-junction affects the offset current. On that account it is not possible to subtract a specific offset from the EBIC signal and a small current range is used as indicated in the sub-plot in figure 6.8 to estimate the measuring error.

Figure 6.9 shows the extraction of the diffusion length from an EBIC-line-scan over a Schottky junction in the proton implanted region of the original sample. To correct the EBIC signal the mean offset has been subtracted. The measuring error is then calculated using the upper and lower limits for the offset as shown in the right image in figure 6.9. This yields a minimum minority carrier diffusion length of $20\pm8\,\mu$m for the proton implanted region of the original sample.

Figures 6.10 and 6.11 show the extraction of the minority carrier diffusion length from the Schottky-junction-EBIC measurement in figure 6.7, along the dashed line. The minority carrier diffusion length was determined to be higher than $145 \pm 30\,\mu$m.
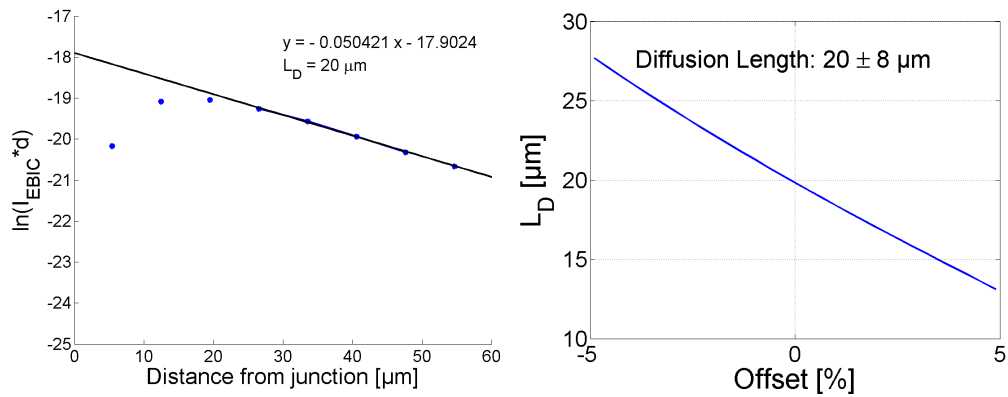
Figure 6.9: Extraction of the minority carrier diffusion length in the proton implanted region of the original sample using the Schottky-junction-EBIC method. **Left image**: Extraction of the diffusion length from the negative inverse slope of the signal plotted as $\ln(I_{EBIC}d)$ versus d. **Right image**: Calculation of the measuring error using the offset current range from the sub-plot in figure 6.8.
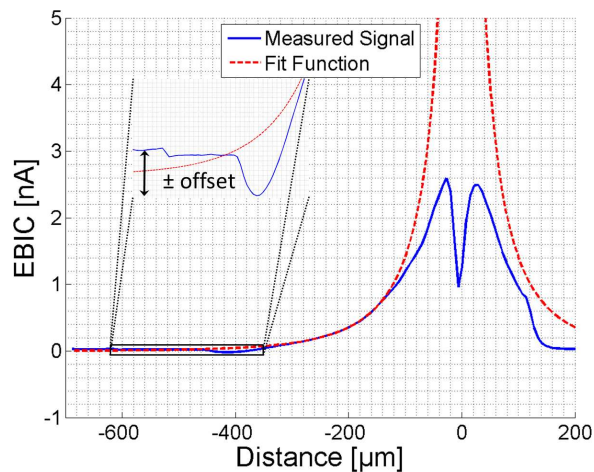
Figure 6.10: EBIC line-scan over a Schottky junction between a tip and the sample in the substrate of the original sample. **Blue line**: Data extracted from the dashed line in figure 6.7. **Red dashed line**: Fit function according to equation 4.19.
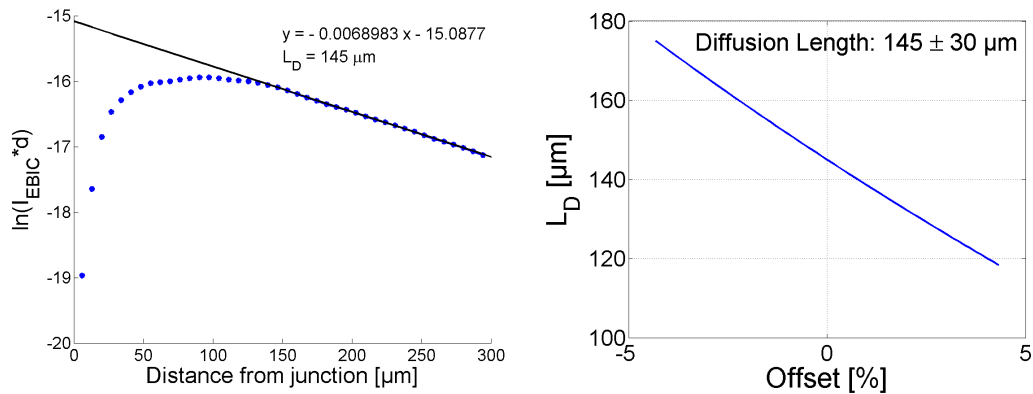
Figure 6.11: Extraction of the diffusion length in the substrate material of the original sample using the Schottky-junction-EBIC method. **Left image:**Extraction of the diffusion length from the negative inverse slope of the signal plotted as $\ln(I_{EBIC}d)$ versus d. **Right image**: Calculation of the measuring error using the offset current range from the sub-plot in figure 6.10.

6.2.3 SRP Analysis

The resistivity of the samples of the annealing series was measured using spreading resistance profiling, as described in section 4.5. Spreading resistance profiles have been recorded as shown in the left plot in figure 6.12. These profiles have then been converted into resistivity profiles using the analysis program associated with the SRP-instrument as demonstrated in the right sub plot in figure 6.12.
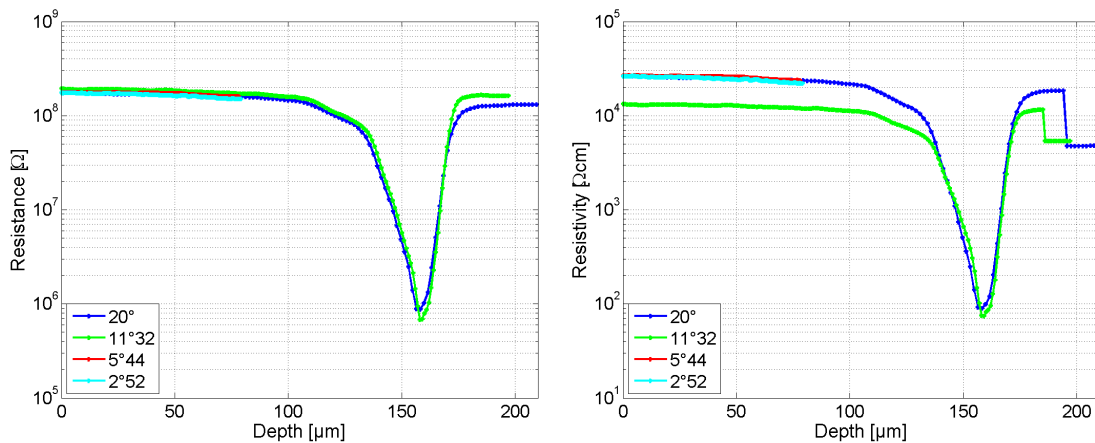
Figure 6.12: Spreading resistance (**left image**) and resistivity (**right image**) profile of the original sample. Four profiles measured at different bevel angles are shown.

The spreading resistance profile shows the development of the resistance on the original sample as a function of the depth. The samples have been beveled at angles of $2\,°52\,'$ and $5\,°44\,'$ for investigations to a depth of $75\,\mu m$ and $11\,°32\,'$ and $20\,°$ for measurements to a depth of $200\,\mu m$. The resistances in all four measurements are constant until a depth of about $100\,\mu m$. Then the resistance decreases and reaches a minimum at the implantation depth at $165\,\mu m$. Looking deeper into the sample the resistance increases again to a similar level as close to the

surface. While the EBIC measurements (see figure 6.2) show a *pn*-junction in this sample, the SRP-measurements do not.

Nevertheless a *pn*-junction was introduced for the calculation of the resistivity profiles, as illustrated in figure 6.12. This introduction is important as the proton implanted area has to be analysed as *n*-doped and the substrate as *p*-doped material. In most cases this introduction led to a bend in the profile as different calibration curves have been used for the calculation of the resistivity for *n*- and *p*-doped regions. The position of the *pn*-junction was chosen in a way to provide enough residual length to measure the mean resistivity of the substrate. While the mean resistivity of the substrate material was determined to be $5000\,\Omega$cm, $20000\,\Omega$cm have been measured at the proton implanted region.

The resistivity profile obtained from the measurement at a bevel angle of $11\,°32\,'$ appears to be of lower resistivity than the other profiles in the right plot in figure 6.12. This might be due to a bad calibration curve for *n*-doped material used in this measurement. Hence the measurement at a bevel angle of $20\,°$ was used for the further analysis of the SRP results.

6.3 Annealed Samples

In this section the different measurements of the samples annealed at different temperatures are compared. The formation and inactivation of thermal donors as a function of the annealing temperature is investigated. All samples have been annealed for one hour.

6.3.1 EBIC Measurements

Different EBIC methods have been used to determine the position of the *pn*-junction, the doping type and the minority carrier diffusion length in different regions of the annealed samples.

To localize the position of the *pn*-junction an EBIC line-scan was performed across the whole samples. The maximum of the electron beam induced current is located at the maximal electric field and hence at the *pn*-junction. The left plot in figure 6.13 shows the depth of the peak of the EBIC signal as a function of the annealing temperature. At annealing temperatures between 25 and 350 °C the position of the *pn*-junction is located at a depth of $180 \pm 10\,\mu$m. Between 300 and 400 °C the position of the *pn*-junction shifts to a depth of 35 µm. The depth of the junction increases at annealing temperatures between 400 and 485 °C to 95 µm. At 500 °C the *pn*-junction is again moved closer to the front side of the sample. Between annealing temperatures of 505 and 510 °C no junction could be located. At 515 °C the *pn*-junction appears again at the original depth of about 180 µm. The depth of the junction increases slightly at annealing temperatures between 515 and 600 °C to 200 µm. If the sample was annealed at temperatures higher than 700 °C no *pn*-junction could be located any more.
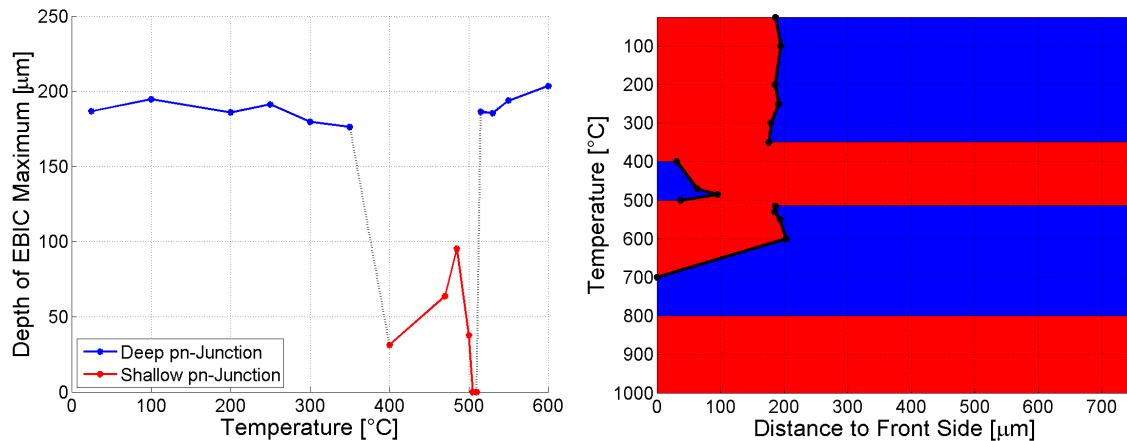
Figure 6.13: Left image: Propagation of the maximum of the electron beam induced current depending on the annealing temperature. Deep *pn*-junctions are drawn in blue, shallow junctions are red. **Right image**: Evolution of the regions of different doping type as a function of the annealing temperature and the distance to the front side of the sample. *n*-type regions are coloured red, *p*-type regions are coloured blue.

The change of the doping type in different regions on the sample and at different annealing temperatures is illustrated in the right image in figure 6.13. The doping type distribution on the sample at low annealing temperatures is shown in the top region of the image. At annealing temperatures below 400 °C the proton implanted front side is *n*-doped (red) the substrate and

p-doped (blue). Between 350 and 400 °C the doping type of the substrate changes from *n*-to *p*-type due to the formation of thermal donors. In the same time a shallow *p*-type region is formed. It is not clear how this *p*-type region can develop, while the substrate is already converted to *n*-type. One reason could be the healing of the radiation damage in this region revealing the original *p*-doping of the substrate material. In the same time the formation of the thermal donor complex, which at these annealing temperatures is already present in the substrate material is inhibited. This could happen due to trapping of oxygen defects at vacancies, as the concentration of vacancies is increased due to the proton implantation. Another cause could be the formation of thermal acceptor complexes formed from radiation induced defects. At an annealing temperatures higher than 500 °C this shallow *p*-type region vanishes, either due to the inactivation of thermal acceptors or the formation of thermal donors, or due to a combination of both. Between 510 and 515 °C the doping of the substrate changes back to *p*-type. The arrangement of the *n*- and *p*-type regions is similar to the condition before the annealing. Between annealing temperatures of 600 and 700 °C the doping type of the proton implanted region changes from *n*- to *p*-type, indicating the inactivation of the thermal donor complexes. After the annealing at a temperature of 700 °C the whole sample is *p*-type. At annealing temperatures between 700 and 800 °C the doping of the whole sample changes from *p*- to *n*-type. The explanation for this could be the formation of another thermal donor complex. The doping of the whole sample stays *n*-type up to annealing temperatures of 1000 °C.

Many species of impurities and impurity complexes can act as recombination centres or traps and hence reduce the charge carrier lifetime τ. As $L_D = \sqrt{D\tau}$, changes in the diffusion length L_D should indicate the formation and disappearance of such impurity complexes. The figures 6.14 and 6.15 show the change of the minority carrier diffusion length in the substrate of the original sample as a function of the annealing temperature. In figure 6.14 the decay of the EBIC signal in an EBIC line-scan, perpendicular to a *pn*-junction was used to extract the diffusion length. As described in section 4.4.3 the limits of the diffusion length were approximated assuming a negligible surface recombination for the lower limit (green curve) and an infinite surface recombination velocity for the upper limit (red curve). The plot of the diffusion length versus the annealing temperature shows a slight decrease between room temperature and annealing temperatures up to 350 °C, indicating an increase of the concentration of bulk recombination centres. At annealing temperatures between 350 and 515 °C no values for the diffusion length of the minority carriers in the substrate could be extracted from EBIC line-scans, as there was no *pn*-junction close to the substrate. At an annealing temperature of 515 °C, as the doping of the substrate material changes from *n*- to *p*-type, a *pn*-junction is formed again and a diffusion length can be extracted. This diffusion length is almost twice the length of the diffusion length of minority carriers in the substrate annealed at 350 °C. This development can be explained by an decrease of the concentration of recombination centres. Annealing the samples at higher temperatures leads to a reduction of the diffusion length. At annealing temperatures higher than 600 °C the *pn*-junction vanishes again and no minority carrier diffusion length can be extracted from EBIC line-scans any more.
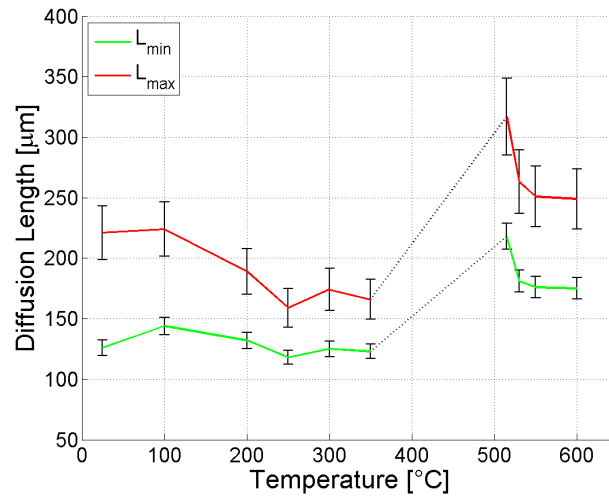
Figure 6.14: Evolution of the minority carrier diffusion length in the substrate region of the original sample, derived from EBIC line-scans. **Green line**: Minimum minority carrier diffusion length, assuming a negligible surface recombination. **Red line**: Maximum minority carrier diffusion length, assuming an infinite surface recombination velocity. The black bars indicate the measuring error.

In figure 6.15, the evolution of the minority carrier diffusion length extracted from Schottky junctions is shown. As the extraction of the diffusion length from Schottky-Junction-EBIC measurements assumes a negligible surface recombination, this measurements yield minimal minority carrier diffusion lengths.

The minimal diffusion length of minority carriers in the substrate is $145 \pm 30\,\mu m$ before the annealing step and decreases to $70\,\mu m$ at annealing temperatures between 100 and $350\,^{\circ}C$. This indicates an increase of the concentration of recombination centres. Between 350 and $400\,^{\circ}C$ the doping is changed from p- to n-type and the minimal diffusion length decreases to $16\,\mu m$. This suggests that the thermal donor complexes which are formed at this annealing temperature act as both, donor levels and recombination centres. At annealing temperatures between 400 and $510\,^{\circ}C$ the minority carrier diffusion length increases slightly indicating the annihilation or inactivation of recombination centres. Between an annealing temperature of 510 and $515\,^{\circ}C$ the doping of the substrate material changes back from n- to p-type and the minority carrier diffusion length is increased from $40\,\mu m$ to almost $150\,\mu m$ at $520\,^{\circ}C$. This indicated the decrease of the concentration of both, thermal donors and recombination centres, supporting the assumption that the defect complex acts as both, donor and recombination centre. At annealing temperatures between 520 and $700\,^{\circ}C$ the diffusion length decreases below $100\,\mu m$. Between 700 and $800\,^{\circ}C$ the doping changes from p- to n-type and the minimal minority carrier diffusion length decreases to less than $25\,\mu m$. The diffusion length decreases further to $18\,\mu m$ at an annealing temperature of $1000\,^{\circ}C$.

The evolution of the minority carrier diffusion length in the proton implanted region of the samples was investigated as well. This evolution is shown in figures 6.16 and 6.17 as a function of the annealing temperature. Figure 6.16 shows the evolution of the minority carrier diffusion length extracted from EBIC-line-scans. Only at annealing temperatures between 400 and $500\,^{\circ}C$ a pn-junction was present in the proton implanted region (see left image in figure 6.13).
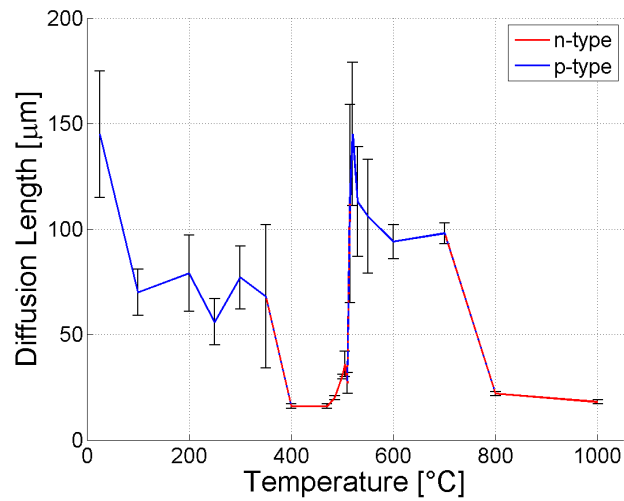
Figure 6.15: Evolution of the minority carrier diffusion length in the substrate region of the original sample, derived from Schottky-junction-EBIC measurements. A blue line is used for *p*-type, a red line for *n*-type material. The black bars indicate the measuring error derived from the different ranges for the offset current.

Hence figure 6.16 only shows the evolution of the diffusion length in this temperature range. A slight increase of the diffusion length of the minority carriers can be observed, indicating the decrease of recombination centres.

In figure 6.17 the minimal minority carrier diffusion length, derived from Schottky-junction-EBIC measurements, is plotted as a function of the annealing temperature. In the temperature range from room temperature to 600 °C the evolution of the diffusion length shows several jumps, either due to the high measuring error or due to the formation and decomposition of different thermally activated defect complexes. At annealing temperatures between 600 and 700 °C the doping in the proton implanted region changes from *n*- to *p*-type and the diffusion length increases drastically from 25 to 100 µm. Between an annealing temperature of 700 and 800 °C the doping changes back to *n*-type and the diffusion length decreases to 30 µm. At annealing temperatures between 800 and 1000 °C the diffusion length decreases slightly to 24 µm The change of the diffusion length of minority carriers in the proton implanted region showed to be relatively small compared to the measuring error in these measurements. This is due to the fact that a bad resolution was chosen for the recording of the Schottky-junction EBIC measurements. Using a higher resolution for the EBIC measurements, more significant and traceable changes due to the formation and degradation of recombination centres in this region could be observed.
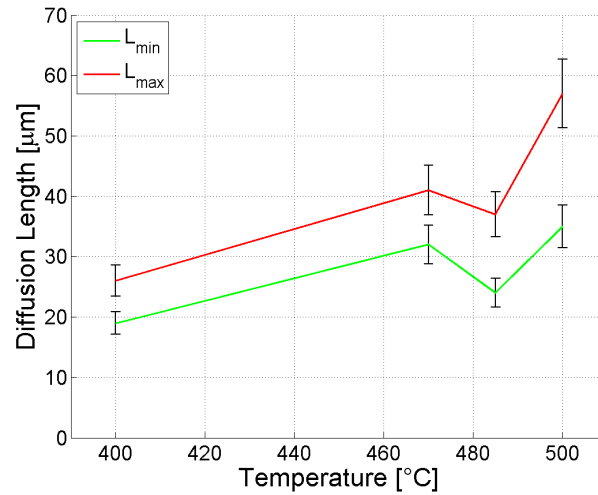
Figure 6.16: Evolution of the minority carrier diffusion length in the proton implanted region of the original sample, derived from EBIC line-scans. **Green line**: Minimum minority carrier diffusion length, assuming a negligible surface recombination. **Red line**: Maximum minority carrier diffusion length, assuming an infinite surface recombination velocity. The black bars indicate the measuring error.
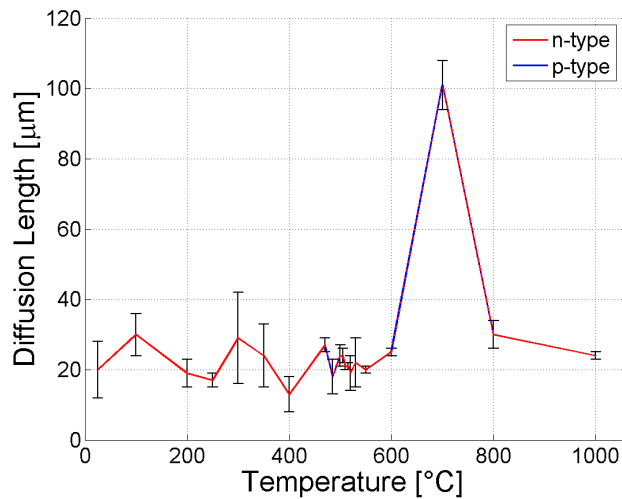
Figure 6.17: Evolution of the minority carrier diffusion length in the proton implanted region of the original sample, derived from Schottky-junction-EBIC measurements. A blue line is used for *p*-type, a red line for *n*-type material. The black bars indicate the measuring error derived from the different ranges for the offset current.

6.3.2 SRP Measurements

Figure 6.18 illustrates the SRP measurements on slices of the original sample annealed at different temperatures for one hour. All measurements, except for the original sample (25 °C) have been performed at a bevel angle of 11 °32 '.
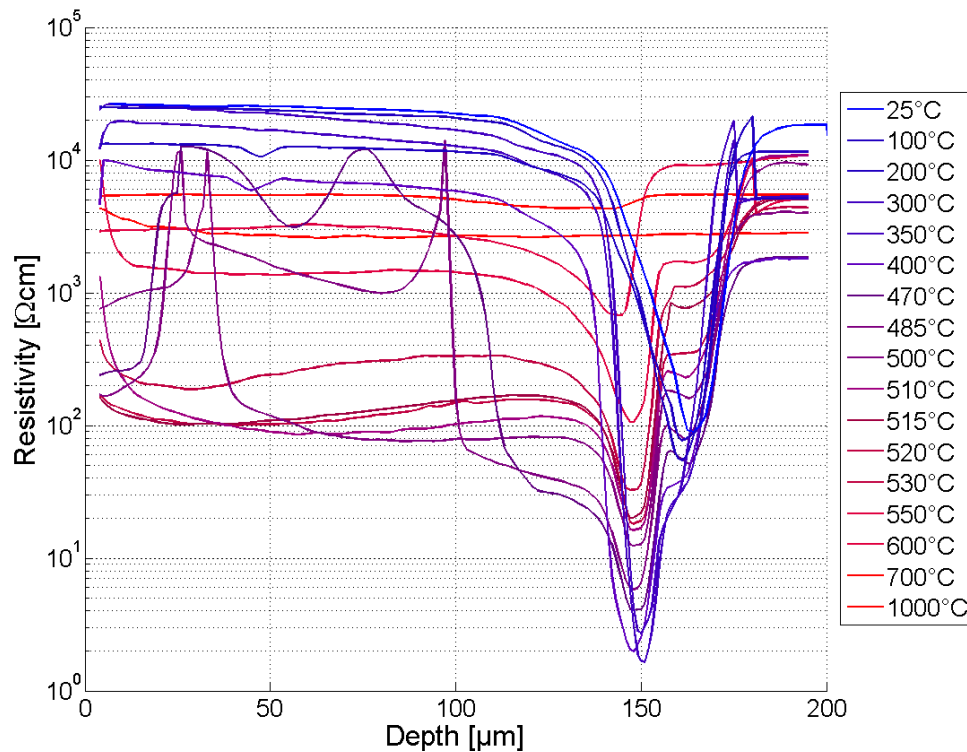
Figure 6.18: Evolution of the resistivity profiles of the original sample as a function of the annealing temperature.

The evolution of the resistivity of the substrate material as a function of the annealing temperature is shown in the right image in figure 6.19. The resistivity values have been obtained by averaging the resistivity values of the region highlighted in the left image in the figure. At annealing temperatures between room temperature and 350 °C the resistivity of the substrate material is about 5000 Ωcm. The doping is *p*-type. At annealing temperatures between 350 and 400 °C The doping of the substrate material changes from *p*- to *n*-type and the resistivity decreases to 1000 Ωcm. This most certainly happens due to the appearance of oxygen related thermal donors as described in [56]. At annealing temperatures between 470 and 510 °C the resistivity of the substrate material increases to more than 1000 Ωcm as the oxygen related thermal donors are inactivated. This inactivation leads to a compensation of the electron excess and hence to a higher resistivity than before the annealing. At annealing temperatures between 510 and 515 °C the doping changes from *n*- back to *p*-type and the resistivity of the substrate increases to 5000 Ωcm again. The resistivity stays the same at annealing temperatures up to 700 °C. At an annealing temperature of 1000 °C, as the doping changes again to *n*-type, the resistivity decreases to 3000 Ωcm. It's not clear yet why the doping type changes again.
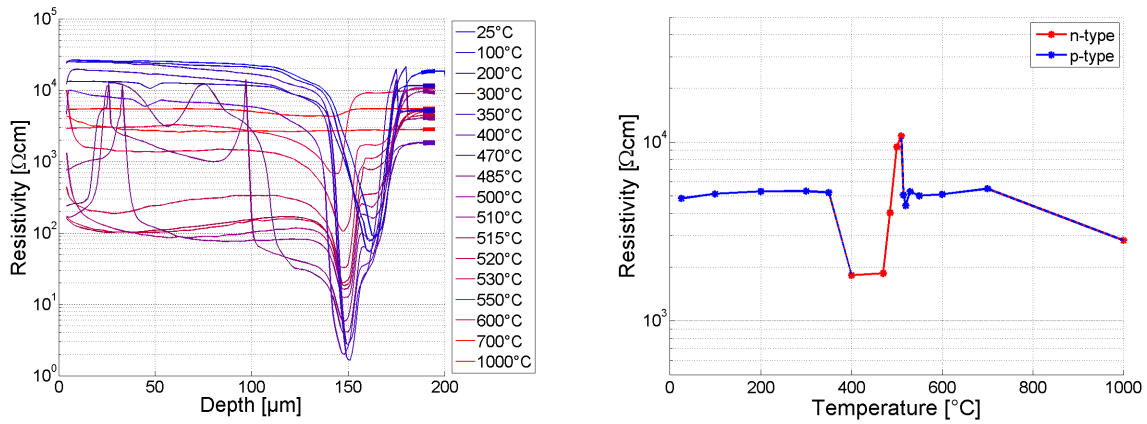
Figure 6.19: Left image: SRP measurements on samples annealed at different temperatures with the substrate region highlighted (at 190 to 200 µm). **Right image**: Evolution of the resistivity of the substrate material as a function of the annealing temperature.

In figure 6.20 the shifting of the depth of the minimum of the resistivity profiles and the minimal resistivity are plotted as a function of the annealing temperature. Starting at a depth of 164 µm the minimum migrates towards the sample surface. Starting at an annealing temperature of 300 °C it stays more or less constant at a depth of 147 µm. Between room temperature and an 350 °C the minimal resistivity decays from 90 to 2 Ωcm. At higher annealing temperatures the resistivity increases again. At 700 °C the resistivity at the minimum is 4000 Ωcm and already close to the resistivity of the starting material. At an annealing temperature of 1000 °C the resistivity is constant over the whole sample and hence, no minimum is present any more.
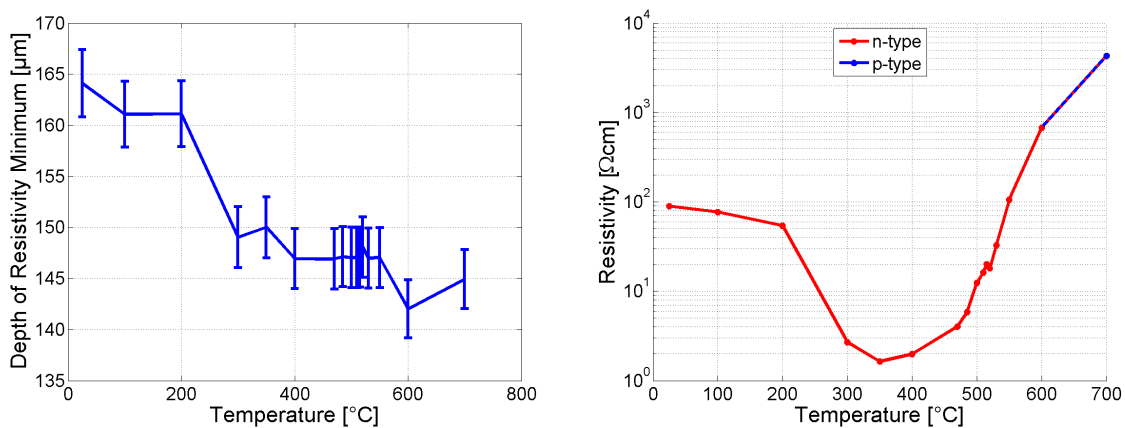
Figure 6.20: Shifting of the depth of the minimum in the resistivity profile (**left image**) and evolution of the minimal resistivity (**right image**) as a function of the annealing temperature.

Right after the proton implantation step the implanted hydrogen is localized close to the implantation depth. This hydrogen rich region expands as a function of the annealing temperature. Figure 6.21 shows the movement of the edge of the hydrogen rich region towards the surface. This progress can also be observed in figure 6.18 as a migration of the left shoulder of

the resistivity minimum towards the sample surface at temperatures between 400 and 500 °C.
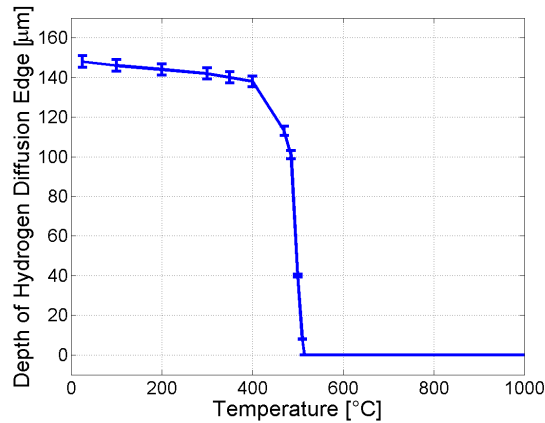
Figure 6.21: Evolution of the hydrogen diffusion edge as a function of the annealing temperature.

The figures 6.22, 6.25 and 6.26 each show a highlighted region in the resistivity profiles and the evolution of the mean resistivity in this region as a function of the annealing temperature. Figure 6.22 focuses on a depth of 120 to 130 μm, which lies in the implanted region of the sample, close to the implantation depth. At annealing temperatures between room temperature and 350 °C the resistivity is about 10000 Ωcm with *n*-type doping and hence quite higher than the resistivity of the starting material (5000 Ωcm). This is due to radiation induced defects caused by the proton implantation which don't heal at small temperatures. Starting at annealing temperatures of 400 °C and higher, on the one hand these defects heal and on the other hand, the hydrogen diffuses to the sample surface, both leading to a reduction of the resistivity which reaches its minimum of 30 Ωcm at an annealing temperature of 470 °C. At annealing temperatures between 470 to 700 °C the resistivity increases again. One cause is the decrease of the concentration of hydrogen related donors as they diffuse further to the surface of the sample. Another cause is the inactivation of these donors, which leads to a change of the doping from *n*- to *p*-type at an annealing temperature of 700 °C. The resistivity is 4000 Ωcm at this temperature and hence close to the resistivity of the substrate material.

Both, the migration of the edge of the hydrogen rich region and the evolution of the resistivity in the region of a depth of 120 to 130 μm are plotted in figure 6.23 as a function of the annealing temperature. Between annealing temperatures of 400 to 470 °C the resistivity, drawn in red, decreases, indicating both, the healing of the radiation damage and the formation of thermal donors. At the same time the region containing the implanted hydrogen expands. The position of the edge of this region is plotted as the blue line in 6.23. At annealing temperatures between 400 and 500 °C the EBIC scans indicate shallow *pn*-junctions. One explanation of the formation of this shallow *p*-doped region, is the healing of the radiation damage in this region, revealing the *p*-doped substrate. At the same time the hydrogen doesn't have enough time or thermal budget to diffuse as far as to the surface.

As illustrated in figure 6.20 the depth of the resistivity minimum moves away from the implantation depth at increasing annealing temperatures. When the resistivity minimum moves, a shoulder, or a region of rather low resistivity is left behind. Figure 6.24 shows the formation of
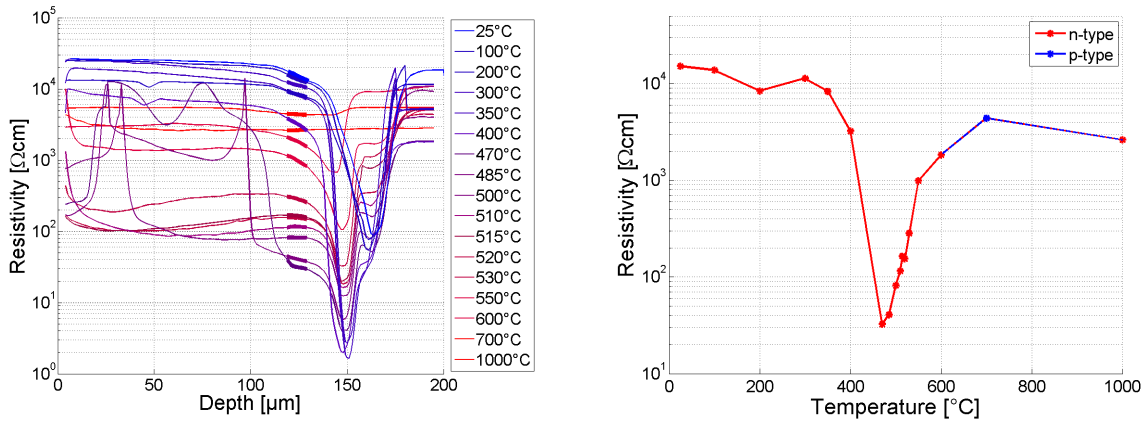
Figure 6.22: Left image: SRP measurements on samples annealed at different temperatures with the implanted region close to the implantation depth highlighted (at 120 to 130 µm). **Right image**: Evolution of the resistivity of this region as a function of the annealing temperature.
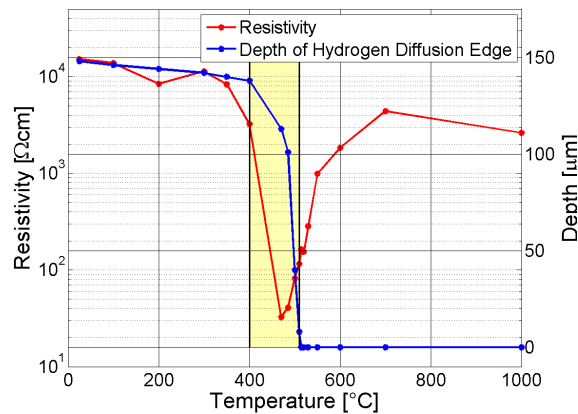
Figure 6.23: Comparison of the movement of the edge edge of the hydrogen rich region (blue) to the evolution of the resistivity close to the implantation depth (red). Highlighted in yellow: Samples annealed at temperatures where a *p*-doped region appeared at the surface.

this shoulder which already begins at an annealing temperature of 300 °C and disappears at annealing temperatures of more than 600 °C. In figure 6.25 the mean resistivity in the region around the implantation depth is plotted as a function of the annealing temperature. The resistivity of the original sample at the implantation depth is 100 Ωcm. Up to an annealing temperature of 470 °C the resistivity in this region decreases slightly to 50 Ωcm. This decrease is far smaller than the decrease of the minimum resistivity (see figure 6.20) as the position of the minimum moves away from the implantation depth. At annealing temperatures between 470 to 600 °C the resistivity of the shoulder increases to a resistivity of more than 10000 Ωcm. One reason might be the decrease of the concentration of hydrogen related thermal donors as they diffuse away from this region. Another reason is the inactivation of the defect complexes leading to a compensation of the excess of electrons. Between annealing temperatures of 600 to 700 °C the doping in the region around the implantation depth changes from *n*- to *p*-type and the resistivity decreases to 5000 Ωcm. At annealing temperatures around 1000 °C the doping

changes back to *n*-type again and the resistivity decreases further to $3000\,\Omega$cm.
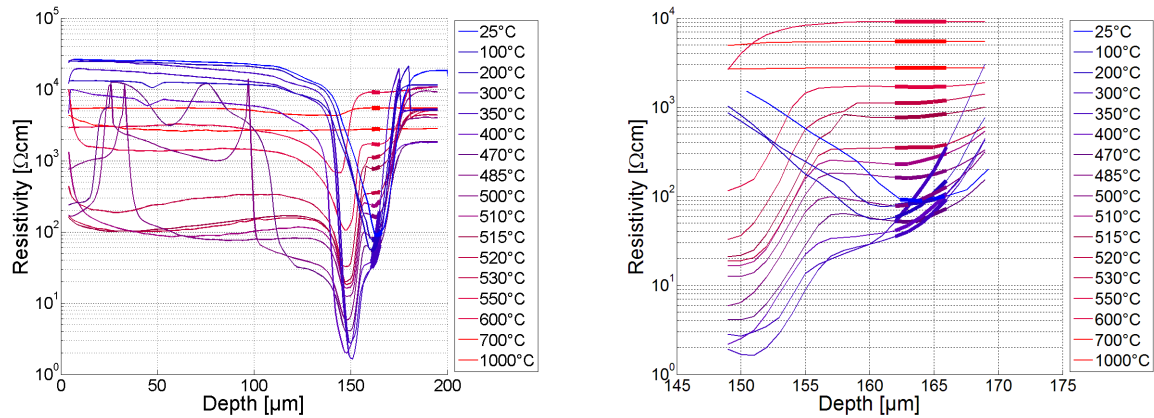
Figure 6.24: Left image: SRP-Measurements on samples annealed at different temperatures with the the implantation depth highlighted (at $164 \pm 2\,\mu$m). **Right image**: Region around the implantation depth in more detail. The formation of a shoulder can be observed at a depth of $155\,\mu$m

In figure 6.26 the region close to the surface is investigated in more detail. This region is located in a part of the sample where the protons where shot through during the proton implantation, creating radiation induced defects. Due to these defects the mean resistivity of this region is high at annealing temperatures up to $350\,^\circ$C. At annealing temperatures between 350 and $400\,^\circ$C the doping changes from *n*- to *p*-type. The mean resistivity decreases at annealing temperatures between 350 to $515\,^\circ$C from more than 10000 to $100\,\Omega$cm. Between annealing temperatures of 500 to $510\,^\circ$C the doping changes back to *n*-type as starting at that temperature the implanted hydrogen diffuses as far as to the surface, forming hydrogen related thermal donors. The mean resistivity in this region increases again to $3000\,\Omega$cm at an annealing temperature of $600\,^\circ$C. Although the doping type changes at higher annealing temperatures the resistivity stays more or less constant.
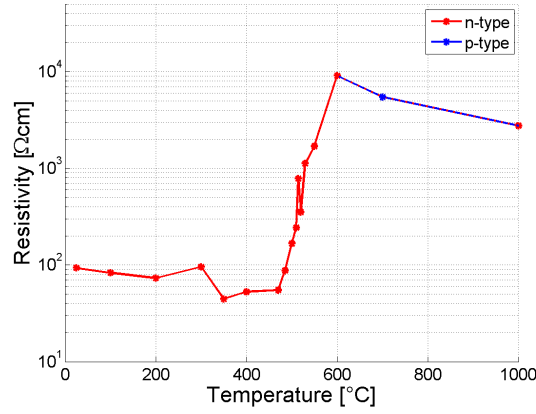
Figure 6.25: Evolution of the resistivity at the implantation depth as a function of the annealing temperature.
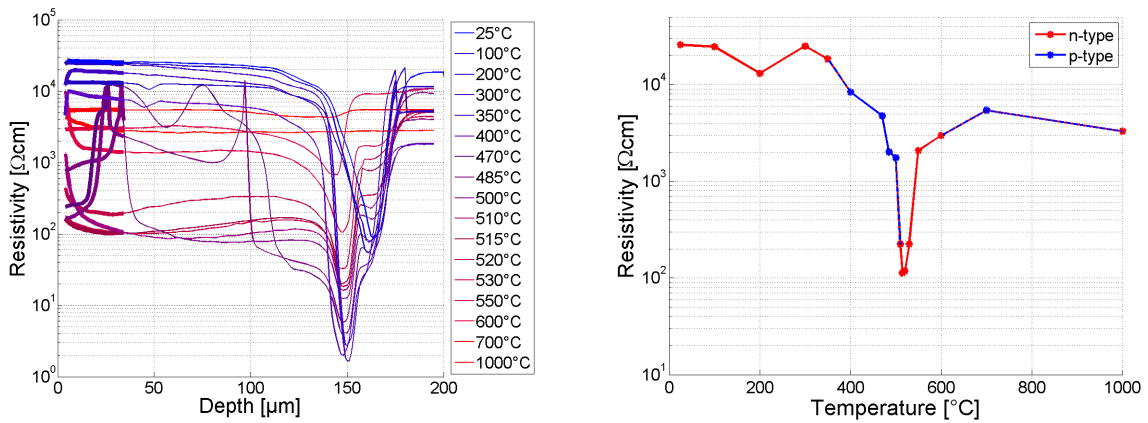
Figure 6.26: Left image: SRP measurements on samples annealed at different temperatures with the implanted region highlighted (at 5 to 35 µm). **Right image**: Evolution of the resistivity of this region depending on the annealing temperature.

6.4 Conclusions and Outlook

To investigate the temperature dependent evolution of defect complexes in proton doped silicon, a series of samples has been prepared which have been annealed at different temperatures. In a first series of measurements the properties of the original, not annealed sample have been studied. The doping type of the substrate was determined to be *p*-type and the implanted region *n*-type. The resistivity of the original sample was higher than $20000\,\Omega$cm in the proton implanted region and $5000\,\Omega$cm in the substrate region. The effects of the annealing considering the sample resistivity, doping type and minority carrier diffusion length have been investigated using spreading resistance profiling (see section 4.5) and different measurement techniques of electron beam induced current (see section 4.4). A list of the changes in the material at certain annealing temperatures can be found in table 13.2 on page 98.

To be able to give more precise temperature ranges, a lot more samples have to be prepared. Also the influence of a change of the annealing time has to be studied. Furthermore different substrate materials considering the concentrations of oxygen and boron should be studied. In addition the proton implantation energy and dose could be changed to see the influence of these factors as well.

7 Formation of the Super Junction in a CoolMOS$^{\text{TM}}$ Device

In this section the formation of the super junction in a CoolMOS$^{\text{TM}}$ device is shown. The CoolMOS$^{\text{TM}}$ is a power transistor with a lower on-resistance than a conventional power MOSFET (see references [57, 58]). Parts of this section are to be published in [59].

7.1 Background

The CoolMOS$^{\text{TM}}$ device is a super-junction MOSFET and differs from the lateral MOSFET due to the introduction of p-doped columns as an elongation of the p-body of the MOSFET (see figure 7.1). A more detailed description of the device can be found in reference [1].
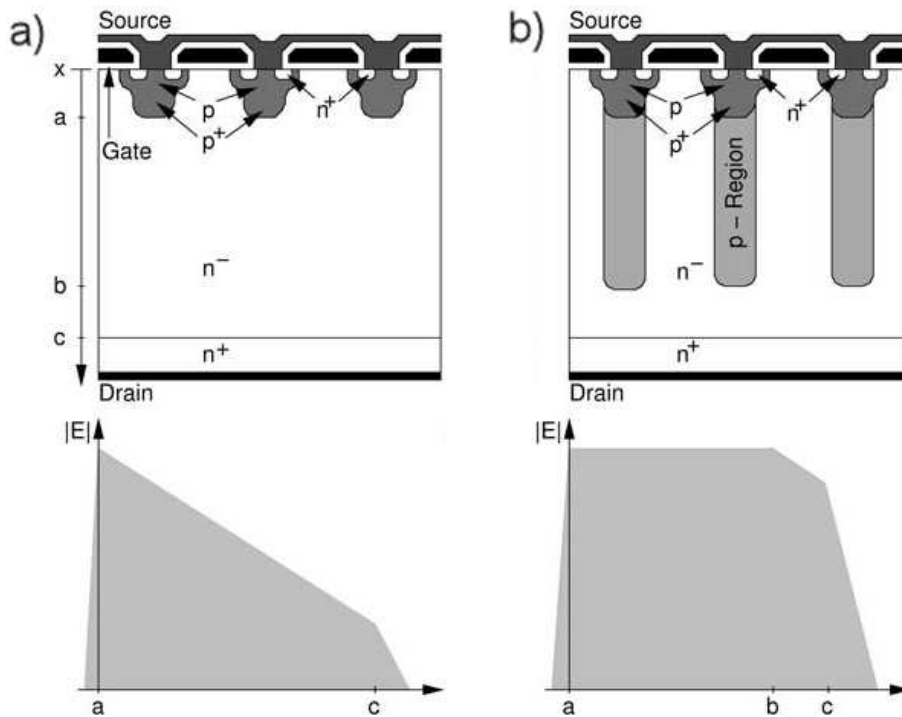
Figure 7.1: Structure of the cross section of a CoolMOS$^{\text{TM}}$-device (**b**) compared to a lateral MOSFET (**a**). The profile of the electric field in the blocking regime of the devices is sketched. The image has been taken from reference [1].

The great advantage of the CoolMOS^{TM} device is the low on-resistance compared to other power transistors. This is achieved by a relatively high doping of the substrate of the device. The ability to still block high voltages origins from the formation of a thick depletion layer, called super junction, when a negative bias voltage is applied. The width of this layer correlates to the length of the p-columns. In figure 7.1 the profile of the electric field is drawn. Comparing the profiles of the electric field of the CoolMOS^{TM} (7.1b) to the one of the lateral MOSFET (7.1a) one can identify a larger area under the profile of the electric field of the CoolMOS^{TM} and hence a higher blocking voltage for the same maximum electric field.

The CoolMOS^{TM} device was of interest for this project because it can also be realized using proton implantation [60, 61].

As described in reference [61], CoolMOS^{TM} devices are usually investigated either after a selective etching step in the scanning electron microscope or using scanning capacitance microscopy. Figure 7.2 shows visualizations of the p-columns of a CoolMOS^{TM} device using different methods, including a simulation and an EBIC 2D-scan.
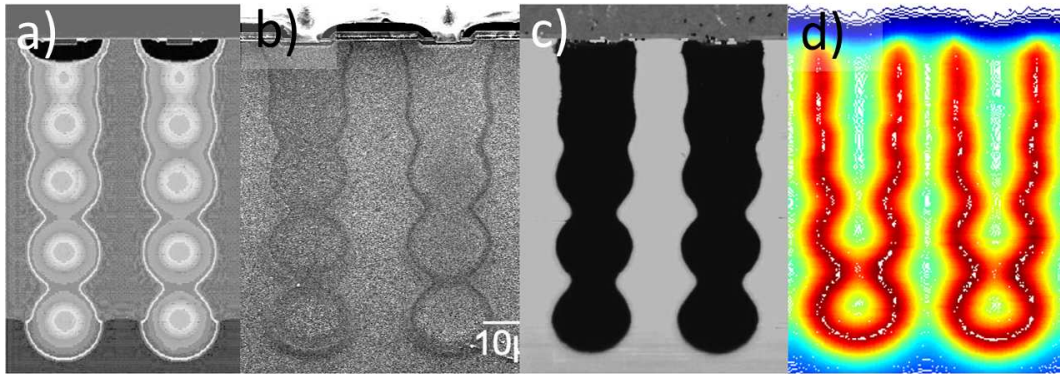
Figure 7.2: Visualization of p-columns on the cross section of a CoolMOS^{TM} device. **a**: Simulation of the structure of the p-columns. **b**: SEM image after selective etching. **c**: SCM image. **d**: EBIC 2D-image. **a**, **b** and **c** have been published in [61].

7.2 Visualization of p-Columns Using Electron Beam Induced Current

For the EBIC measurements, a CoolMOS^{TM} wafer was broken into pieces. As a first measurement, a 1×1 cm piece was glued with the front side (source side) on a thick piece of silicon using a conducting glue. The specimen was then ground from the backside (drain side) in a small angle, to form a beveled cross section through the whole device. After inserting the sample on a planar view specimen holder (see figure 4.6) the source and the drain where each contacted using micromanipulators.

All EBIC measurements in this section were performed using an acceleration voltage of $20\,$kV. Figure 7.3 shows SEM and EBIC images on the surface of this sample. While in the SEM images only a weak contrast can be observed, the EBIC images show defined red circles, representing the pn-junctions between the p-columns and the n-matrix. The diameter of the p-columns depends on the depth. As the sample is beveled at a small angle the circles at the top of figure 7.3c differ from the columns at the bottom of the figure.
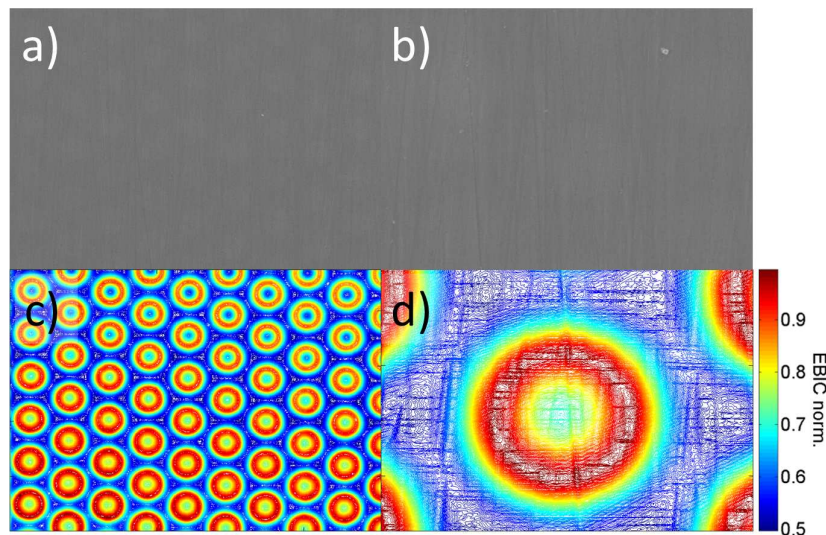
Figure 7.3: Plan view SEM (**a** and **b**) and EBIC (**c** and **d**) images of a CoolMOS^{TM} device. **a** and **c** show an overview of p-doped columns in an n-doped matrix. **b** and **d** show one p-column in more detail. The maximum of the normalized EBIC signal and hence the pn-junctions are coloured red; regions far from pn-junctions and hence yielding small EBIC signals, are blue.

There are two possible directions in which a cross sectional sample can be prepared. Figure 7.4 shows a plan view image of the columns which are arranged in a sixfold symmetry. The sample can than be prepared either along a row of columns (direction **B**) or perpendicular to such a row (direction **A**).

For the analysis of the cross section the samples where simply broken along either direction **A** or **B** and mounted in the scanning electron microscope using the cross section specimen holder (see figure 4.6). The two copper cylinders of the sample holder make contact to source and drain. Figure 7.5 shows SEM and EBIC images of the cross sections of samples either

prepared along direction **A** or **B**. d_A and d_B are the distances between the centres of the columns prepared along direction **A** an **B**. d_A is related to d_B as $d_A = d_B\sqrt{3}$.
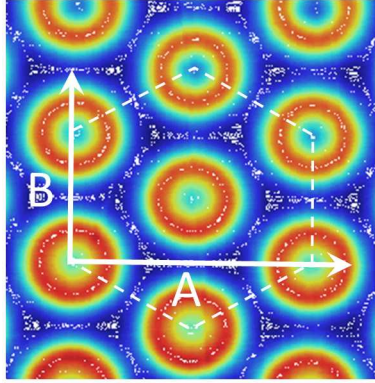
Figure 7.4: Sixfold symmetry of the *p*-column pattern in a CoolMOS^{TM}. Samples have been prepared by breaking along directions **A** and **B**.
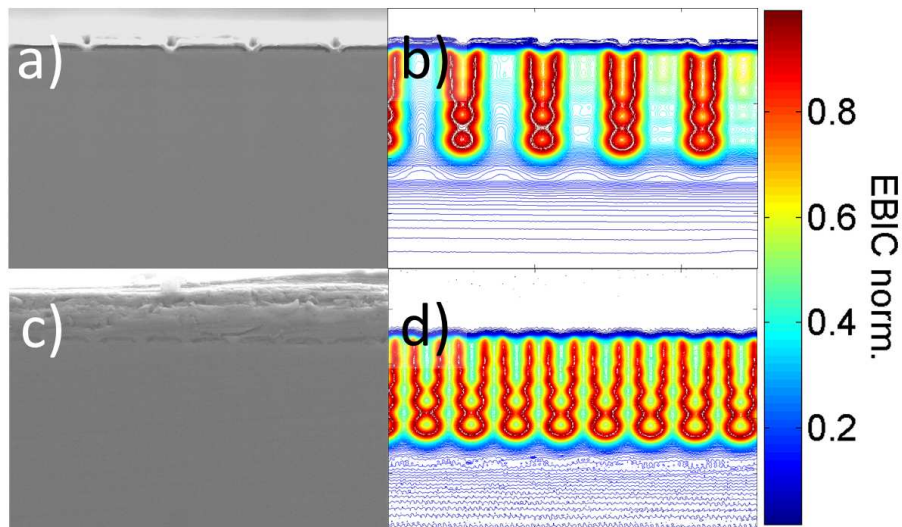
Figure 7.5: a and **b**: SEM and EBIC image of the cross section of a CoolMOS^{TM} device prepared perpendicular to a row of columns (direction **A**). **c** and **d**: SEM and EBIC image of the cross section of a CoolMOS^{TM} device prepared along a row of columns (see figure 7.4 direction **B**).

7.3 Visualization of the Formation of the Super Junction

If a negative voltage is applied from source to drain, the *pn*-junction between the *p*-columns and the *n*-matrix is reverse biased. This leads to a change of the work function of electron in the conduction band of the *p*-columns and hence to a voltage contrast in the SEM image (see section 4.3.4). Figure 7.6 shows voltage contrast images of the same position on the cross section of a CoolMOS^{TM} prepared along direction **A** at different reverse bias voltages.
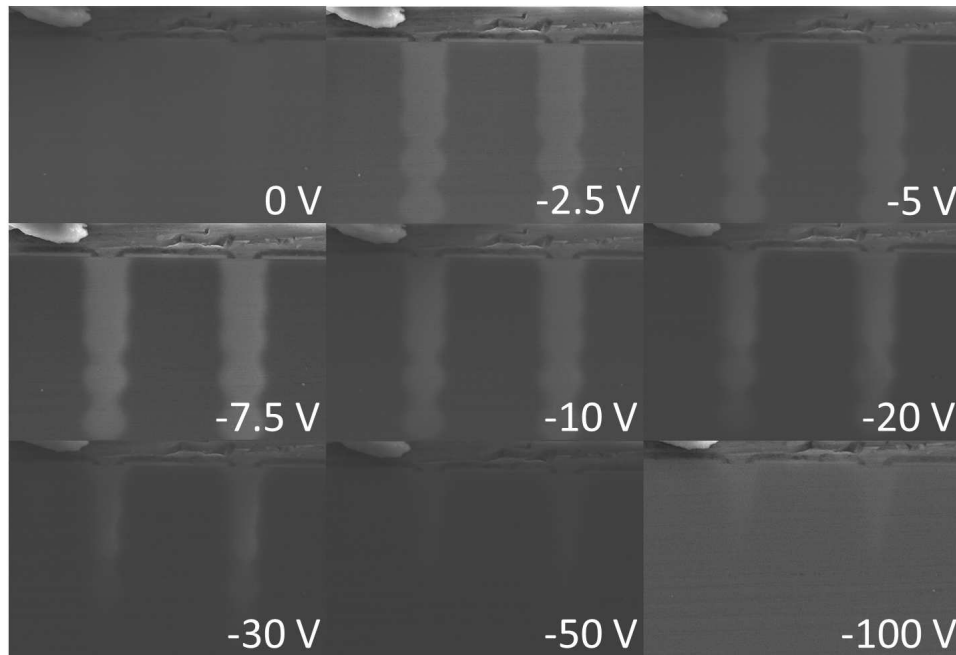
Figure 7.6: Voltage contrast images of the cross section of a CoolMOS^{TM} device at reverse bias voltages from 0 to -100 V.

At 0 V no voltage contrast is visible. As soon as a bias voltage is applied the *p*-columns appear. If the bias voltage is increased the width of the columns seems to decrease. The higher the reverse bias voltage, the more the space charge region at this *pn*-junction extends and, hence, the area of brighter contrast decreases. As soon as the whole area is depleted the voltage contrast disappears completely.

Figure 7.7 shows a waterfall chart of AC-EBIC line-scans recorded at the same position as the voltage contrast images in figure 7.6 applying different reverse bias voltages. As the reverse leakage current at higher reverse bias voltages exceeded the electron beam induced current by a factor of thousand and more, not the standard EBIC method but rather the EBIC chop-scan (see section 4.4.3) method was used. The two *p*-columns are located at 1.5 to 2.5 units and 4.5 to 5.5 units. At zero bias the line scan shows four maxima at the four *pn*-junctions between the two *p*-columns and the *n*-matrix. If the reverse bias voltage is increased, the peaks of the EBIC signal flatten, until the maximum of the EBIC signal reaches through the whole *p*-column at -30 V. In the same time the difference between the maximum and the minimum of the EBIC signal decreases.
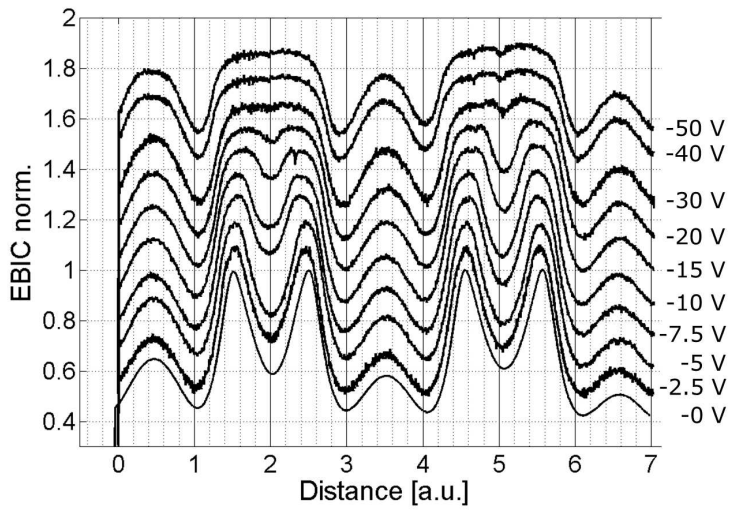
Figure 7.7: Waterfall chart of EBIC line scans across two *p*-columns in a CoolMOS^{TM}-device at different bias voltages.

7.4 Conclusions

The structure of a CoolMOS^{TM} transistor, consisting of *p*-doped columns in an *n*-type matrix has been studied using electron beam induced current measurement techniques. The device was investigated in plan view and in a cross sectional orientation. The cross sectional samples were prepared along two different orientations of the rows of columns. Furthermore the expansion of the space charge region at the *pn*-junction between the columns and the matrix has been examined using different reverse bias voltages. This expansion has been visualized using the voltage contrast method (see section 4.3.4) and EBIC chop-scan method (see section 4.4.3). While the voltage contrast images only show the appearance and the reduction of the columns, the EBIC images show the partial formation of the super junction in the device. For better visualizing this mechanism, AC-EBIC line-scans have been recorded at different reverse bias voltages. The waterfall chart, containing these scans shows the expansion of the space charge region until it reaches through a whole *p*-column.

8 Discussion of the Measurements

8.1 Schottky-Junction-EBIC Measurements

The Schottky-junction-EBIC (see section 4.4.3) method has proven to be a powerful method to determine the doping type of silicon samples (see sections 5 and 6). The limits, concerning the resistivity or the doping concentration of the investigated sample for this method have not been explored yet. The highest resistivity of an investigated sample, which was already known, was more than $1000\,\Omega$cm for p-doped and $650\,\Omega$cm for n-doped material. It is assumed that the method still works for the determination of the doping type of samples with a higher resistivity.

However, not all measurements yielded clear signals. Figure 8.1 shows a Schottky-junction-EBIC measurement on the p-doped substrate region of a sample from the annealing series (see section 6), annealed for $1\,$h at $530\,°$C. In this measurement the signal was collected with the upper tip, reaching to the sample from the lower left corner. The EBIC signal at the Schottky junction formed between this tip and the sample is negative, hence the doping is p-type. If the EBIC signal generated at the Schottky junction between the other, lower tip and the sample is investigated, one sees a broad positive signal with a sharp negative peak in the centre (see sub-plot in figure 8.1).
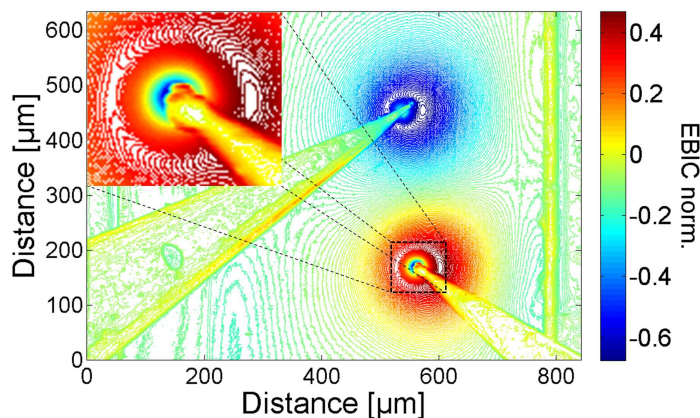
Figure 8.1: Schottky-junction-EBIC measurement on p-type material, yielding no clear signal. The signal was measured with the upper tip. The signal generated at the second tip is magnified.

It has not yet been identified, where this negative peak comes from. If the position of the tip or the contact pressure were slightly changed, the minimum disappeared again.

8.2 Four Point Resistivity Measurement

The four point resistivity measurement method (see section 4.6) used in this project has shown to yield accurate resistivity values for low resistivity, *n*-type samples (see section 5). It has also been shown, that the variation for the results for measurements on high resistivity *p*-type samples is high.

The sub-plots a-c in figure 8.2 where obtained from a "good" measurement while d-f originate from a "bad" one. In the "good" measurement a straight line is obtained if the voltage between the measuring tips V_{34} is plotted against the sourced current I_{12} (see sub-plot 8.2c). This is not true for the "bad" measurement (sub-plot 8.2f). Here the curve rather looks like the VI-plot between the outer tips (sub-plot 8.2d) and hence like a double diode. The explanation for this effect is a bad contact between the measuring tips. As soon as a small current flows between these tips, the measured voltage increases drastically.

Generally it can be said, that measurements on high resistivity samples are hard to interpret, as the sum of the contact and the sample resistances in the measurement approaches to the maximal resistance that can be measured with the instruments used.
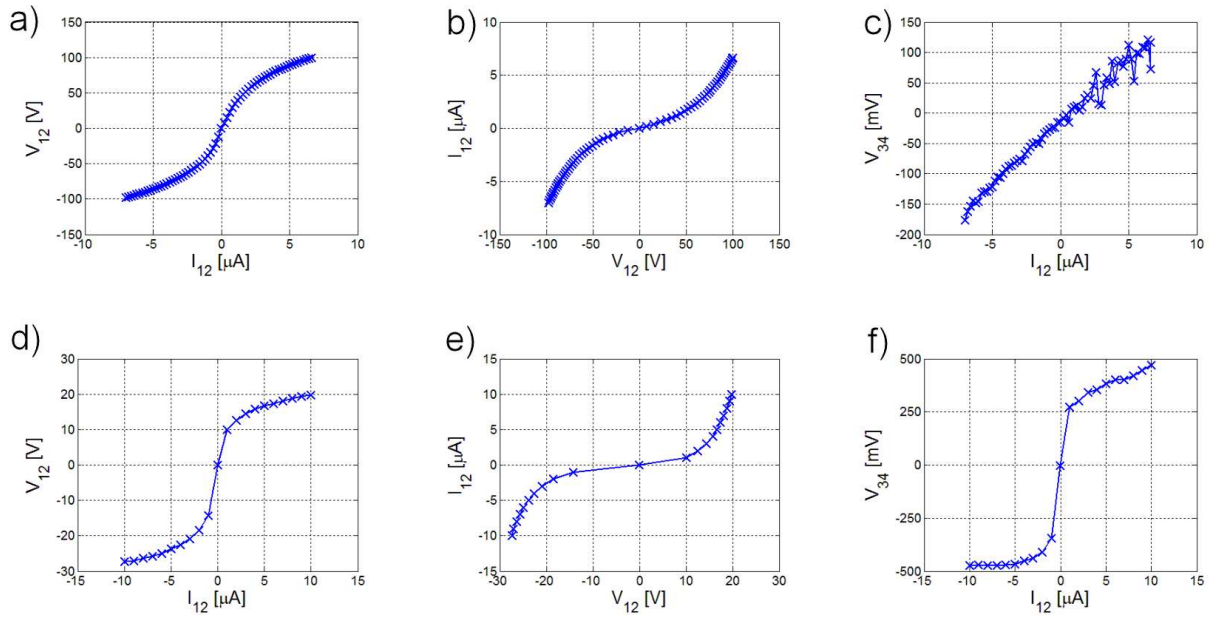
Figure 8.2: a-c): Four-point-resistivity measurement on sample S2 with constant contacts. **d-f)**: Measurement on the same sample at a different position with changing contacts. The indices of current and voltage axes are derived from the tip numbering in figure 4.23. **a)** and **e)**: Voltage V_{12} between the current source and sink versus the sourced current I_{12}; **b)** and **e)**: IV-characteristic between the current source and sink; **c)** and **f)**: potential difference V_{34} between the measurement tips versus the sourced current I_{12}.

8.3 Extraction of Diffusion Lengths

Due to a lack of comparable data, the results of the extraction of diffusion lengths (see section 4.4.3) could not be verified. Nevertheless, the data itself showed high measurement uncertainties up to more than 50% (see figure 6.17).

In figure 8.3 the two methods for the extraction of the diffusion length are compared. Both methods, the EBIC line-scan and the Schottky-junction-EBIC measurement should yield a minimal minority carrier diffusion length as both assume a negligible surface recombination. The two plots in figure 8.3 show that the Schottky-junction-EBIC measurements generally yield a smaller minimal minority carrier diffusion length.
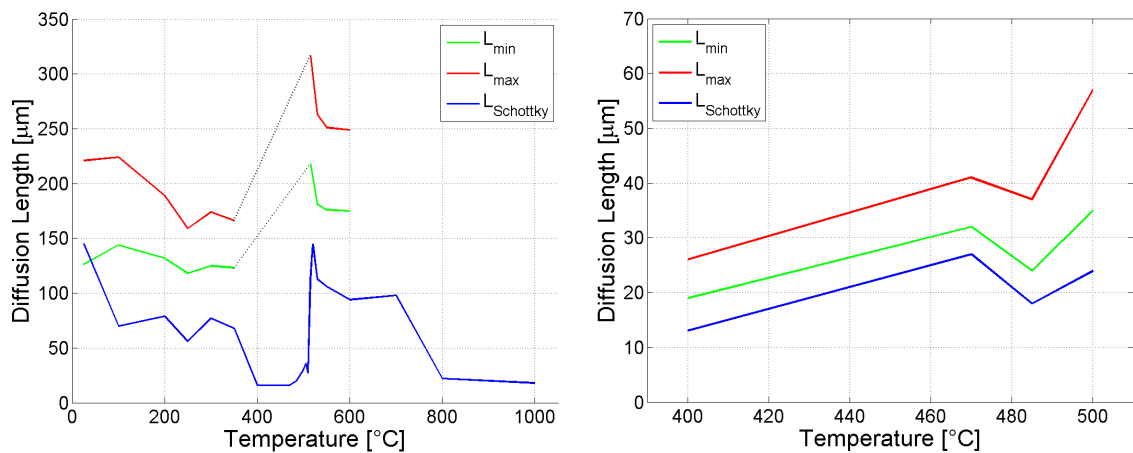
Figure 8.3: Comparison of the EBIC line-scan and the Schottky-junction-EBIC method for the extraction of the minority carrier diffusion length on the substrate material (**left image**) and the proton implanted region (**right image**) of the original sample as a function of the annealing temperature. **Red line**: Maximal diffusion length derived from EBIC line scans. **Green line**: Minimal diffusion length derived from EBIC line-scans. **Blue line**: Minimal diffusion length derived from Schottky-junction-EBIC measurements.

The comparison of the two methods also shows that the relative changes of the diffusion length as a function of the annealing temperature are quite the same for both measurement methods.

8.4 Spreading Resistance Profiling

Up to a certain point the SRP measurement (see section 4.5) has proven to be a reliable and trustworthy analysis method. Nevertheless, this is only true for comparative measurements. The effort that has to be made to conserve a good reproducibility is very high compared to other analysis methods. Small changes in the quality of the measurement tips or the polished surface lead to drastic changes in the results. The measuring error is small for measurements on samples with a medium resistivity but increases when samples with a rather high or a very low resistivity are measured. One way to diminish the error in these measurements would be to add calibration samples at the extrema of the calibration curve, but such material is not easy found. Hence, the measurements at the high resistivity samples in this thesis cannot be taken as absolute. However, the analysis method is good enough for measuring qualitative changes also in high resistivity regions on a sample.

8.5 EBIC-2D-Scan

The influence of the acceleration voltage on the resolution of the EBIC images was investigated using a CoolMOS$^{\text{TM}}$ (section 7) sample.

Figure 8.4 shows two *p*-columns, prepared along direction **A** (see figure 7.4) at different acceleration voltages. If low acceleration voltages are used only at the very *pn*-junction an EBIC signal is collected. In this case most of the charge carriers generated far from the *pn*-junction recombine before they reach the junction and can be separated. If low acceleration voltages are used, the interaction volume is small and located close to the surface (see figure 4.3). Hence it is very likely that most of the carriers recombine at the surface. If the acceleration voltage is increased, both, the number of generated charge carriers and the generation volume are increased, leading to a higher and more spread EBIC signal. At higher acceleration voltages, also the buried column between the two investigated ones emerges. This indicates that charge carriers are generated in a greater depth if the acceleration voltage is increased and hence also buried junctions can be investigated using electron beam induced current measurement techniques.
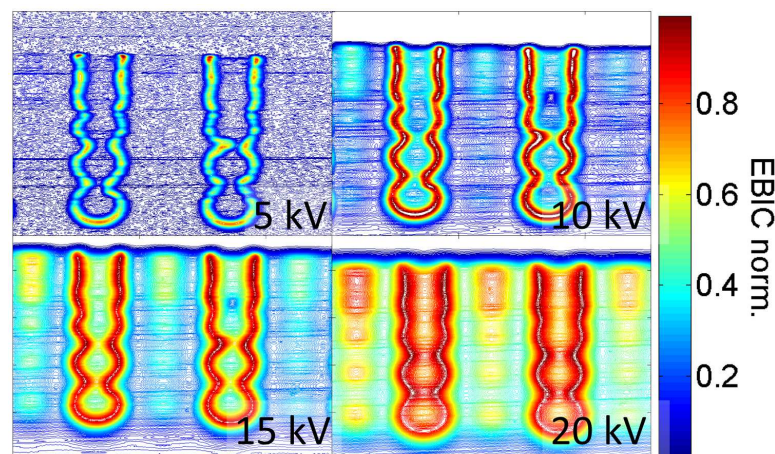
Figure 8.4: EBIC measurement at the *pn*-junction between *p*-doped columns and *n*-doped matrix on the cross section of a CoolMOS$^{\text{TM}}$ device, along direction **A** at an acceleration voltage of 5, 10, 15 and 20 kV. The EBIC signals are normalized; a red color signalizes a high EBIC signal and blue colour a small one.

9 Conclusions

This thesis presents various measurement methods for collecting spatially resolved information about the electrical properties of semiconductor samples.

The investigation of high ohmic, hence low doped semiconductor samples is difficult. Most analysis methods are limited to charge carrier concentrations higher than $10^{13}\,\mathrm{cm}^{-3}$ or resistivities lower than $1000\,\Omega\mathrm{cm}$. A combination of electron beam induced current detection and four point resistivity measurement provides the possibility of determining both, the doping type and the resistivity of unknown samples in a scanning electron microscopy. Both measurement methods have been applied in a scanning electron microscopy. p- and n-doped, high and low ohmic material has been investigated. Using the Schottky-junction-EBIC technique, the doping type of samples with a resistivity up to more than $5000\,\Omega\mathrm{cm}$ could be determined.

Another challenge is the investigation of proton implanted silicon. Here the doping is achieved by defect complexes which form after the proton implantation in a subsequent annealing step. The investigation of such samples is difficult because the charge carrier concentrations are low and the doping is not obtained by an element dopant but by defect complexes and thus, cannot be measured using ToF-SIMS. For this thesis a sequence of proton doped samples has been prepared. A p-doped (boron) raw silicon wafer with a resistivity of $6000 \pm 3000\,\Omega\mathrm{cm}$ (measured using the four point method) had been implanted with a dose of $2 \times 10^{14}\,\mathrm{H^+/cm}^2$ of $4\,\mathrm{MeV}$ protons. The wafer was cut and the pieces were annealed at different temperatures for one hour each. After the annealing step the samples were investigated using electron beam induced current techniques in a scanning electron microscope and spreading resistance microscopy. Using EBIC-methods, the doping type of the proton implanted samples has been determined in spatial resolution. Furthermore the minority carrier diffusion length has been measured in both, the implanted and not implanted region. The spatial distribution of the sample resistivity was obtained from SRP-measurements. Various changes in the material depending on the annealing temperature could be observed, including changes of the doping type due to the formation and deactivation of defect complexes.

The data about the changes in resistivity, doping type and the minority carrier diffusion length collected in this thesis could be amended by investigating more samples, using different annealing times and even different raw materials. In the end it should be possible to predict the effects of the proton implantation under various conditions. A greater goal would be the identification of the exact composition of these defects, including their microscopical shape and energy levels. This way it would even be possible to simulate the effects of proton implantation and annealing.

Additionally to the investigations on proton doped silicon, a CoolMOS$^{\mathrm{TM}}$ device has been investigated. There are only a few analysis methods being capable of visualizing the p-doped columns in the n-doped matrix of a CoolMOS$^{\mathrm{TM}}$ device. In this thesis EBIC techniques have been used, yielding a very good visualization of these columns. Furthermore, applying dif-

ferent bias voltages, the formation of the super junction in such a device could also be visualized.

This thesis proofs EBIC to be a very promising analysis method in semiconductor failure analysis, capable of yielding not only informations about *pn-* or Schottky junctions in the sample. Additionally it is possible to obtain spatially resolved information of the doping type and the minority carrier diffusion length.

10 References

[1] J. Lutz. *Halbleiter-Leistungsbauelemente.* Springer-Verlag Berlin Heidelberg, 2006.

[2] R. Siemieniec, F. J. Niedernosterheide, H. J. Schulze, W. Südkamp, U. Kellner-Erdehausen, and J. Lutz. "Irridation-induced deep levels in silicon for power device tailoring". In: *Journal of the Electrochemical Society* 153 (2006), G108–G118.

[3] D. C. Swako and J. Bartko. "Production of fast switching power thyristors by proton irradiation". In: *IEEE Transactions on Nuclear Science* 30 (1983), pp. 1756–1758.

[4] J. Hartung and J. Weber. "Shallow hydrogen-related-donors in silicon". In: *Physical Rreview B* 48 (1993), pp. 14161–14166.

[5] M. Bruel. "Silicon on insulator material technology". In: *Electronics Letters* 31 (1995), pp. 1201–1202.

[6] J. G. Laven. "Untersuchung und Modellierung von Dotierungsprofilen in Silicium erzeugt durch Protonenimplantationen im MeV-Bereich". PhD thesis. Friedrich-Alexander-Universität Erlangen-Nürnberg, 2012.

[7] E. Simoen, Y. L. Huang, Y. Ma, J. Lauwaert, J. M. Clauws P.and Rafi, A. Ulyashin, and C. Claeys. "What do we know about hydrogen-induced thermal donors in silicon". In: *Journal of the Electrochemical Society* 156 (2009), H434–H442.

[8] Y. V. Gorelkinskii, V. O. Sigle, and Z. S. Takibaev. "EPR of conduction electrons produced in silicon by hydrogen ion implantation". In: *Physica Status Solidi (a)* 22.1 (1974), K55–K57.

[9] B. N. Mukashev, M. F. Tamendarov, S. Zh. Tokmolodin, and Frolov V. V. "Hydrogen implantation into silicon. Infra-red absorption spectra and electrical properties". In: *Physica Status Solidi (a)* 91 (1985), pp. 509–522.

[10] Y. Tokuda, A. Ito, and H. Ohshima. "Study of shallow donor formation in hydrogen implanted n-type silicon". In: *Semiconductors* 13 (1998), pp. 194–199.

[11] P. J. Potts. *A handbook of silicate rock analysis.* Chapman and Hall, 1987, pp. 336, 337.

[12] E. T. Everhart and P. H. Hoff. "Determination of kilovolt electron energy dissipation vs penetration distance in solid materials". In: *Journal of Applied Physics* 42 (1971), pp. 5837–5846.

[13] R F. Egerton. *Physical Principles of Electron Microscopy.* Springer Science, 2005.

[14] D. R. Younkin. "Phase dependent SEM IC chip testing with voltage contrast". Pat. 4387304. 1983.

[15] H. J. Leamy. "Charge collection scanning electron microscopy". In: *Journal of Applied Physics* 53.6 (1982), R51–R80.

[16] S. Kirnstötter, M. Faccinelli, P. Hadley, R. Job, W. Schustereder, J. G. Laven, and H. J. Schulze. "Investigation of doping type convertion and diffusion length extraction of proton implanted silicon by EBIC". 2012.

[17] F. Berz and H. K. Kuiken. "Theory of life time measurements with the scanning electron microscope: steady state". In: *Solid-State Electronics* 19 (1976), pp. 437–445.

[18] V. K. S. Ong, J. C. H. Phang, and D. S. H. Chan. "A direct and accurate method for the extraction of diffusion length and surface recombination velocity from an EBIC line scan". In: *Solid-State Electronics* 37.1 (1994), pp. 1–7.

[19] A. Boudjani, G. Bassou, T. Benbakhti, M. Beghdad, and Belmekki B. "Direct measurement of minority carrier diffusion length in planar devices". In: *Solid-State Electronics* 38 (1995), pp. 471–475.

[20] D. S. H. Chan, V. K. S. Ong, and J. C. H. Phang. "A direct method for the extraction of diffusion length and surface recombination velocity from an EBIC line scan: planar junction configuration". In: *IEEE Transactions on Electron Devices* 42 (1995), pp. 963–968.

[21] D. E. Ioannou and S. M. Davidson. "Diffusion length evaluation of boron-implanted silicon using the SEM-EBIC/Schottky diode technique". In: *Journal of Physics D: Applied Physics* 12.8 (1979), pp. 1339–1344.

[22] D. E. Ioannou and C. A. Dimitriadis. "A SEM-EBIC minority-carrier diffusion-length measurement technique". In: *IEEE Transactions on Electron Devices* 29 (1982), pp. 445–450.

[23] L. Chernyak, A. Osinsky, H. Temkin, J. W. Yang, Q. Chen, and M. Asif Khan. "Electron beam induced current measurements of minority carrier diffusion length in gallium nitride". In: *Applied Physics Letters* 69.17 (1996), pp. 2531–2533.

[24] V. K. S. Ong. "A direct method of extracting surface recombination velocity from an electron beam induced current line scan". In: *Review of Scientific Instruments* 69.4 (1998), pp. 1814–1816.

[25] O. Kurniawan and V. S. Ong. "An analysis of the factors affecting the alpha parameter used for extracting surface recombination velocity in EBIC measurements". In: *Solid-State Electronics* 50 (2006), pp. 345–354.

[26] R. G. Mazur, R. C. Stephenson, M. J. Andy, C. L. Hartford, and J. R. Rogers. "Spreading Resistance Profiling System". English. Pat. 6052653. 2000.

[27] J. C. Maxwell and J. J. Thompson. *A treatise on electricity and magnetism.* Oxford, Calendron, 1904.

[28] Y. V. Sharvin. "A possible method for studying Fermi surfaces". In: *Soviet Physics JETP* 21 (1965), pp. 655–656.

[29] G. Wexler. "The size effect and the non-local Boltzmann transport equation in orifice and disk geometry". In: *Proceedings of the Physical Society* 89.4 (1966), pp. 927–941.

[30] M. Pawlik. "Spreading resistance: A quantitative tool for process control and development". In: *Journal of Vacuum Science and Technology B* 10.1 (1992), pp. 388–396.

[31] *Standard Practice for Conversion Between Resistivity and Dopant Density for Boron-Doped, Phosphorus-Doped, and Arsenic-Doped Silicon.* American Society for Testing and Materials, 2003. DOI: 10.1520/F0723-99.

[32] S. M. Hu. "Between carrier distributions and dopant atomic distribution in beveled silicon substrates". In: *Journal of Applied Physics* 53 (1982), pp. 1499–1510.

[33] A. Casel and H. Jorke. "Comparison of carrier profiles from spreading resistance analysis and from model calculations for abrupt doping structures". In: *Applied Physics Letters* 50 (1987), pp. 989–991.

[34] P. A. Schumann Jr. and E. E. Gardner. "Spreading resistance correction factors". In: *Solid-State Electronics* 12 (1969), pp. 371–375.

[35] S. C. Choo, M. S. Leong, and J. H. Sim. "An efficient numerical scheme for spreading resistance calculations based on the variational method". In: *Solid-State Electronics* 26.8 (1983), pp. 723–730.

[36] A. F. Yaremchuk. "Analysis of the correction factor in the spreading resistance technique for monitoring epitaxial silicon". In: *Applied Physics (a)* 76.3 (2003), pp. 405–411.

[37] J. van Linschoten, J. Snijder, and M. W. Hillen. "Preprocessing of data from spreading resistance maeasurements". In: *Solid State and Electron Devices* 127.2 (1980), pp. 100–104.

[38] T. Clarysse and Vandervorst W. "An efficient smoothing algorithm for spreading resistance calculations". In: *Solid-State Electronics* 31.1 (1988), pp. 53–63.

[39] L. B. Valdes. "Resistivity measurements on germanium for transistors". In: *Proceedings of the IRE* 42 (1954), pp. 420–427.

[40] P. De Wolf. "Two dimensional carrier profiling of semiconductor structures with nanometer resolution". PhD thesis. Katholieke Universiteit Leuven, 1998.

[41] P. De Wolf, T. Clarysse, W. Vandervorst, J. Snauwaert, and L. Hellemans. "One- and two-dimensional carrier profiling in semiconductors by nanospreading resistance profiling". In: *Journal of Vacuum Science and Technology B: Microelectronics and Nanometer Structures* 14.1 (1996), pp. 380–385.

[42] P. De Wolf, T. Clarysse, W. Vandervorst, L. Hellemans, P. Niedermann, and W. Hänni. "Cross-sectional nano-spreading resistance profiling". In: *Journal of Vacuum Science and Technology B* 16.1 (1998), pp. 355–361.

[43] L. Zhang, K. Ohuchi, K. Adachi, K. Ishimaru, M. Takayanagi, and A. Nishiyama. "High-resolution characterization of ultrashallow junctions by measuring in vacuum with scanning spreading resistance microscopy". In: *Applied Physics Letters* 90 (2007), pp. 192103 1–3.

[44] L. Zhang, H. Tanimoto, K. Adachi, and A. Nishiyama. "1-nm spatial resolution in carrier profiling of ultrashallow junctions by scanning spreading resistance microscopy". In: *IEEE Electron Device Letters* 29.7 (2008), pp. 799–801.

[45] D. Alvarez, J. Hartwich, M. Fouchier, P. Eyben, and W. Vandervorst. "Sub-5-nm-spatial resolution in scanning spreading resistance microscopy using full-diamond tips". In: *Applied Physics Letters* 82.11 (2003), pp. 1724–1726.

[46] H. Jacobs, F. A. Brand, J. D. Meindl, M. Benanti, and R. Benjamin. "Electrodeless measurement of semiconductor resistivity at microwave frequencies". In: *Proceedings of the IRE* 49 (1961), pp. 928–932.

[47] S. Bothra and J. M. Borrego. "Spatially resolved resistivity measurements in semiconductor wafers using microwave techniques". In: *20th European Microwave Conference* 2 (1990), pp. 990–995.

[48] J. Krupka and J. Mazierska. "Contactless measurement of resistivity of semiconductor wafers employing single-post and split-post dielectric-resonator techniques". In: *IEEE Transactions on Instrumentation and Measurement* 56 (2007), pp. 1839–1844.

[49] J. R. Matey and J. Blanc. "Scanning capacitance microscopy". In: *Journal of Applied Physics* 57 (1985), pp. 1437–1444.

[50] Y. Huang, C. C. Williams, and J. Slinkman. "Quantitative two-dimensional dopant profile measurement and inverse modeling by scanning capacitance microscopy". In: *Applied Physics Letters* 66 (1995), pp. 344–346.

[51] Y. Li, J. N. Nxumalo, and D. J. Thomson. "Two-dimensional imaging of charge carrier profiles using local meatal-semiconductor capacitance-voltage measurement". In: *Journal of Vacuum Science and Technology B* 16 (1998), pp. 457–462.

[52] F. Giannazzo, F. Priolo, V. Raineri, and V. Privitera. "High-resolution scanning capacitance microscopy of silicon devices by surface beveling". In: *Applied Physics Letters* 76.18 (2000), pp. 2565–2567.

[53] R. Stephenson, A. Verhulst, P. DeWolf, M. Caymax, and W. Vandervorst. "Contrast reversal in scanning capacitance microscopy imaging". In: *Applied Physics Letters* 73.18 (1998), pp. 2597–2599.

[54] W. Shockley, G. L. Pearson, and J. R. Haynes. "Hole injection in germanium - quantitative studies and filamentary transistors". In: *Bell Sys. Tech. Journal* 28 (1949), pp. 344–366.

[55] T. J. van der Pauw. "A method of meausuring specific resistivity and hall effect of discs of arbitrary shape". In: *Philips Research Reports* 13.1 (1958), pp. 1–9.

[56] A. Ourmazd and W. Schröter. "Oxygenrelated thermal donors in silicon: A new structural and kinetic model". In: *Journal of Applied Physics* 56 (1984), pp. 1670–1681.

[57] G. Deboy, M. März, J. P. Stengl, H. Strack, J. Tihanyi, and H. Weber. "A new generation of high voltage MOSFETs breaks the limit line of silicon". In: *International Electron Devices Meeting 1998 Technical Digest* 1 (1998), pp. 683–685.

[58] L. Lorenz, G. Deboy, M. März, J. P. Stengl, and A. Bachofner. "Drastic reduction of on-resistance with CoolMOS^{TM}". In: *PCIM Europe* 5 (1998), pp. 250–258.

[59] S. Kirnstötter, M. Faccinelli, P. Hadley, R. Job, W. Schustereder, J. G. Laven, and H. J. Schulze. "Imaging superjunctions in CoolMOS^{TM} devices using electron beam induced current". 2012.

[60] M. Rüb, M. Bär, F. J. Niedernosterheide, M. Schmitt, H. J. Schulze, and A. Willmeroth. "First study on superjunction high-voltage transistors with n-columns formed by proton implantation and annealing". In: *Proceedings of the 16th International Symposium on Power Semiconductor Devices and ICs* 1 (2004), pp. 181–184.

[61] M. Buzzo, M. Ciappa, M. Rüb, and W. Fichtner. "Characterization of 2D dopant profiles for the design of proton implanted high-voltage superjunction". In: *Proceedings of the 12th IPFA* 1 (2005), pp. 285–289.

11 List of Figures

12 List of Tables

13 Appendix

Table 13.1: Annealing conditions for annealing series of proton doped sample.

Annealing Temperature [°C]	Annealing Time [h]	EBIC	SRP Bevel Aangel
25 (no annealing)	0	✓	2 °52 ', 5 °44 ', 11 °32 ', 20 °
100	1	✓	2 °52 ', 5 °44 ', 11 °32 '
200	1	✓	2 °52 ', 5 °44 ', 11 °32 '
250	1	✓	no SRP
300	1	✓	2 °52 ', 5 °44 ', 11 °32 '
400	1	✓	2 °52 ', 5 °44 ', 11 °32 '
470	1	✓	2 °52 ', 5 °44 ', 11 °32 '
485	0.25	✓	no SRP
485	0.5	✓	2 °52 ', 5 °44 ', 11 °32 '
485	0.75	✓	no SRP
485	1	✓	2 °52 ', 5 °44 ', 11 °32 '
485	1.5	✓	no SRP
485	2	✓	no SRP
485	2.5	✓	no SRP
485	5	✓	no SRP
500	1	✓	2 °52 ', 5 °44 ', 11 °32 '
500	2.5	✓	no SRP
505	1	✓	no SRP
510	1	✓	2 °52 ', 5 °44 ', 11 °32 '
510 (He-atmosphere)	1	✓	no SRP
515	1	✓	2 °52 ', 5 °44 ', 11 °32 '
515	2.5	✓	no SRP
515	5	✓	no SRP
520	1	✓	11 °32 '
530	1	✓	11 °32 '
530	2.5	✓	no SRP
530	5	✓	no SRP
550	1	✓	11 °32 '
600	1	✓	11 °32 '
700	1	✓	11 °32 '
800	1	✓	no SRP
1000	1	✓	11 °32 '
1000 (He-atmosphere)	1	✓	11 °32 '

Table 13.2: Changes of material properties at different ranges of the annealing temperature.

Temp [°C]	Change of material	Explanation
25-300	Shift of the resistivity minimum from 164 μm to 148 μm leaving a low resistivity region behind	Diffusion of hydrogen related donors enabled by radiation damage
300-700	Immobilization of resistivity minimum at $145 \pm 3\,\mu m$	Diffusion of hydrogen related donors stopped due to healing of radiation damage
350-400	Conversion of substrate doping from p- to n-type, decrease of the diffusion length	Formation of a thermal donor complex
350-400	Formation of a shallow p-type region	Healing of the radiation damage. The formation of thermal donor which is present in the substrate is inhibited
350-470	Decrease of the resistivity in the implanted region close to the implantation depth	Beginning of the diffusion of the implanted hydrogen forming hydrogen related thermal donor complex
350-700	Increase of the minimal resistivity	Diffusion of hydrogen away from the implantation depth, deactivation of hydrogen related thermal donor complex which was formed during the implantation
400-485	Expansion of shallow p-type region	Healing of the radiation damage in greater depths of the sample, or, formation of a thermal acceptor complex
470-510	Increase of the resistivity of the substrate material	Slow inactivation of the thermal donor complex or formation of a thermal acceptor which slowly compensates the thermal donor
470-600	Increase of the resistivity at the implantation depth $(164 \pm 2\,\mu m)$	Deactivation of thermal donor or compensation due to a thermal acceptor
485-500	Contraction of shallow p-type region	Expansion of hydrogen rich region, forming hydrogen related thermal donor complexes
510-515	Conversion of substrate doping from n- to p-type, increase of the diffusion length	Deactivation of the thermal donor complex formed between 350 and 400 °C
600-700	Conversion of all residual n-type regions to p-type, leaving an all p-type sample with a homogeneous minority carrier diffusion length and resistivity, except for the implantation depth	Deactivation of residual thermal donor complexes
700-800	Conversion of the doping of the whole sample from p-to n-type, strong decrease of the minority carrier diffusion length	Formation of another thermal donor complex.